Batteries and Battery Management: Development of Low Cost, Rapid Impedance Measurement Equipment Suitable for Fast Analysis of Li-ion Cells

Huw Price

MPhil Thesis

October 2014

110109181

Supervisor: Prof. D.A. Stone

Second Supervisor: Dr M.P. Foster

ABSTRACT - Batteries are a vital and integral part of modern life, installed in devices of every scale from personal portable electronic equipment to electricity grid energy storage. As people become increasingly dependent on battery energy sources, they also become increasingly reliant on accurate methods of quantifying the amount of useful energy available to them in order to function in their daily lives. Electrochemical Impedance Spectroscopy (EIS) is a branch of System Identification that can be used to identify battery metrics by which the remaining short-term (i.e. remaining charge) and long-term (battery lifetime remaining) life of a battery may be assessed. In this thesis the author gives an overview of battery chemistries and battery state estimation techniques before describing the development of a system capable of performing rapid impedance measurements. The development process spans two system designs, and results are given of impedance tests on lithium iron phosphate cells (LiFePO$_4$) and lithium titanate (Li$_4$Ti$_5$O$_{12}$) cells. A key feature of the method is to use Pseudo-Random Binary Sequences (PRBS) to approximate white noise, thereby providing equal stimulation of a wide band of frequencies simultaneously and reducing the required test-time. This document will be of use to those wishing to develop EIS test equipment at low-cost, and those who require a method of rapidly obtaining an impedance spectrum.

Contents

List of Figures

List of Tables

List of Acronyms

- ADC   Analogue-to-Digital Converter
- ANN   Artificial Neural Network
- BESS   Battery Energy Storage System
- BMS   Battery Management System
- C/LCO   Graphite/Lithium Cobalt Oxide ($LiCoO_2$)
- C/LFP   Graphite/Lithium Iron Phosphate ($C/LiFePO_4$)
- C/LMO   Graphite/Lithium Manganese Oxide ($C/LiMn_2O_4$)
- C/NCA   Graphite/Lithium   Nickel   Cobalt   Aluminium   Oxide ($LiNiMnCoO_2$)
- C/NCM   Graphite/Lithium   Nickel   Manganese   Cobalt   Oxide ($LiNi_xMn_yCo_zO_2$) (also C/NMC)
- CAN   Controller Area Network
- DOD   Depth of Discharge
- DUT   Device Under Test
- EKF   Extended Kalman Filter
- EMF   Electromotive Force
- EOL   End-Of-Life
- FL   Fuzzy Logic
- FRF   Frequency Response Function
- HEV   Hybrid Electric Vehicle
- IC(E)   Internal Combustion (Engine)
- KF   Kalman Filter
- LTO   Lithium Titanate anode material ($Li_4Ti_5O_{12}$)
- OBD   On Board Diagnostics
- OCV   Open Circuit Voltage
- PDC   Pulsed Discharge
- PRBS   Pseudo-Random Binary Sequence

- SEI   Solid Electrolyte Interface
- SLPB   Super Lithium Polymer Battery
- SOA   Safe Operating Area
- SoC   State of Charge
- SoF   State of Function
- SoH   State of Health
- VAS   Voltage Amplification Stage
- VRLA   Valve-Regulated Lead-Acid, a type of Pb-acid Battery

Chapter 1: Introduction

The purpose of this chapter is to provide context for the author's work. There is a brief description of the most popular battery chemistries of the last two centuries, followed by a more detailed look at Lithium-ion batteries and an outline of key current research in Battery Management System (BMS) technology. This gives a platform from which the author's research into battery impedance testing using Pseudo-Random Binary Sequences (PRBS) can be discussed.

1.1 A Background to Battery Technologies

1.1.1 Lead Acid (Pb-acid) Batteries

Lead-acid (Pb-acid) batteries are the most mature rechargeable battery technology, with over 150 years of development behind them. The batteries comprise of a series of cells containing positive electrodes of lead dioxide and negative electrodes of sponge lead, which are immersed in an aqueous sulphuric acid electrolyte and separated by a micro-porous material. Broadly speaking, the batteries fall into two categories; the flooded (or 'vented') type, in which the electrolyte is an aqueous sulphuric acid solution, or a valve-regulated (VRLA) type in which the acid electrolyte is immobilized in a porous separator material, and a pressure regulating valve seals the battery. The valve in VRLA batteries is a safety device and not an operational mechanism.

Pb-acid batteries are low-cost, rugged and relatively tolerant to abuse [1]. They require careful maintenance procedures to prevent large sulphate crystals from forming, which reduce the overall battery capacity and can be difficult to break up during recharge. Crystal formation is likely when the battery is over-discharged or kept in a discharged state [2].

Pb-acid battery technology is mature and widespread, the flooded cells being most commonly used in Internal Combustion (IC) vehicles as starter batteries, and employed in fork lift trucks and traditional 'milk float' vehicles. They are used in the leisure industry as off-grid power for motor homes and marine craft, often coupled with diesel generators or charged from an auxiliary drive. The largest configuration lead-acid batteries have been designed for bulk energy storage, with disappointing results; in 1986 the Southern California Edison Chino facility was commissioned to produce a 10 MW/40 MWh BESS (Battery Energy Storage

System) plant which was the largest of its kind, but few people have promoted the technology since as life-cycle costs are not competitive [3]. For applications with lower capacity requirements, conventional batteries become more competitive as they are no longer competing for the same market as the more typical bulk storage technologies such as pumped-storage hydro-electric. Figure 1.1 shows a 1 MW/1.4 MWh installation at Metlakatla Power & Light, Alaska, which is estimated to have saved over $6.5 Million over 12 years of operation and exceeded initial life projection by almost 50 % [4]. A key factor to the success of an installation such as this lies in the implementation of the Battery Management System (BMS), which in this case maintained 378 VRLA batteries over a 12 year lifetime.

Figure 1.1 – A 1 MW/1.4 MWh BESS at Metlakatla Power & Light, Alaska. The installation consists of 378 Exide VRLA modules.

Source: DOE Global Energy Storage Database, www.energystorageexchange.org

In 1994 a 21 MW / 14 MWh facility was installed at Sabana Llana by the Puerto Rico Electric Power Authority (PREPA) to mitigate under-frequency load shedding, and whilst it was operationally beneficial, it eventually failed prematurely and led to a governmental 'lessons-learned' study in 1999 [5]. A major recommendation of this report is to invest considerable resource in the accurate measurement and control of battery state-of-charge in any future projects [5], as measurement of state of charge, and state of health is critical to obtaining the best performance from any battery system, based on any chemistry.

Other applications include rapid spinning reserve, frequency control, and voltage regulation, along with UPS (Uninterrupted Power Supply) services on a local level.

Pb-acid batteries are one of the most benign battery technologies, however without proper regulation and battery management, Pb-acid batteries can give rise to hydrogen generation on recharge which may present a risk of explosion without proper ventilation. Lead is a restricted substance under EU law and its use is subject to legislation, along with the relevant obligations for safe disposal [6], however Pb-acid batteries can be recycled, and an existing infrastructure for battery recycling can achieve a 97% recycling of the lead in a battery [7], which is far higher than any other material commonly recycled.

1.1.2   *Nickel Cadmium (Ni-Cd) and Nickel-Metal Hydride (Ni-MH) Batteries*

First made at the turn of the 20th century, Ni-Cd (Nickel Cadmium) batteries have been in development for almost as long as lead-acid batteries. The 1990's saw the commercialisation of the Ni-MH (Nickel-metal hydride) battery, bringing higher capacity and the use of safer materials. However Ni-MH batteries do suffer from a higher self-discharge rate than equivalent Ni-Cd units, while Ni-Cd batteries are capable of higher maximum discharge rates than the equivalently sized Ni-MH battery. Ni-MH batteries can generally improve on the capacity of Ni-Cd by 25% to 40% for a given battery volume [8], however to date both technologies remain in widespread use.

Ni-Cd cells are able to tolerate a state of deep discharge for long periods, making them more robust than many other battery chemistries. Their terminal voltage is comparatively stable over deep charge cycles, and their average lifetimes are typically longer than those of Pb-acid. The capacity of Ni-Cd batteries is largely impervious to rate of discharge, but if a constituent cell in a string of cells is discharged excessively, a cell can become reverse polarized, which leads to capacity degradation [2]. Ni-Cd batteries can cost up to ten times more than lead-acid batteries, but provide a higher energy density, longer cycle life and exhibit less frequent maintenance intervals [8].

EU legislation effectively means that Ni-MH has superseded Ni-Cd technology, due to the high toxicity of cadmium and restrictions on its use [9]. Cadmium is a heavy metal, highly toxic to all life forms, and poses considerable environmental waste issues for Ni-Cd batteries.

Ni-MH batteries are more environmentally friendly, with most nickel recovered at end of life and used in corrosion resistant alloys such as stainless steel [10]. During charging, water in the cell is split into hydrogen and oxygen, which at low charge rates can recombine to form into water again, thus making the batteries maintenance free; however if a Ni-MH is charged at too high a rate, the excess energy splits water in the cell electrolyte into hydrogen and oxygen at a faster rate than it can recombine which can cause internal pressure build up at high charge rates leading to cell rupture [2].

Currently the moves within the automotive market are towards Lithium based batteries, where most of the development in cell technology is now focussed, despite the Honda Insight, Honda Civic and Toyota Prius hybrid electric vehicles (HEV's) employing Ni-MH based cell chemistries.

1.1.3   Lithium-Ion Batteries

Lithium has the lowest density of any metal, and the highest electrochemical potential. With the proliferation of consumer portable electronics in the 1980's lithium batteries were developed for their excellent power to weight ratio, and pioneering work was commercialised by Sony in the early 1990's [11]. Lithium batteries are available with a large number of different electrode chemistries, but the main focus for secondary (rechargeable) batteries has been on Li-ion and Li-ion polymer batteries, until the 1990's mostly for the consumer electronics industry, but now also for large scale electric vehicle and grid Battery Energy Storage Systems (BESS).

Lithium based battery technology is currently widely researched, and is also overlapping into development of both flow-battery [12] and metal-air battery [13] technology. Compared to older battery chemistries, Li-ion batteries have high specific energy (energy-to-weight ratio), are efficient, have long lifetimes, minimal memory effect and low self-discharge. While solutions for the consumer electronics market could be considered quite mature, there remain difficulties in scaling up the technology until safety, cost, and materials availability can be resolved [14].

While Li-ion cells have high current capacity, this must be limited in practice to prevent internal heating and early failure. Safety has been a significant issue in bringing the consumer battery technology to market and Li-ion cells can only be safely operated in conjunction with

a battery management system (BMS) providing minimum over-voltage, under-voltage, over-current and over-temperature protection [2]. Larger utility scale systems will also require cell voltage balancing, as when cells are in series, the performance of the overall system can be limited by the performance of the weakest cell. Other drawbacks are high cost and the reduction in lifetime caused by deep discharging [15], along with a limited and strict safe operating temperature range.

In a major review of Li-ion batteries for the Journal of Power Sources, Scrosati et al [14], insist that a radical change in the internal lithium battery structure is required, and that a complete change in chemical process is required away from the current - and restrictive - insertion electrodes mechanism, which is limited to one electron per formula unit, to conversion processes which instead allow two to six electrons per formula unit. The authors point out that this step has already been made in lithium-air and lithium-sulphur technology, and that rapid success will be dependent upon the efficient exchange of information between interdisciplinary studies. Smaller improvements are constantly being reported and research into cathode, electrolyte and anode materials continues to bring advancement [16].

Research until the early 2000's was concentrated on macroscopic changes to cell structure, when increasing electrode surfaces brought increased risk of secondary reactions involving electrolyte decomposition. When this problem was solved with new electrode coatings, it cleared the path for the current trend in nano-scale research and vastly increased electrode surface areas, with nanotechnology providing improvements in power, capacity, cost, materials and sustainability, and promising more still [17]. Polymer electrolyte batteries are being developed that alleviate such issues as internal shorting, electrolyte leakage, and having combustible reaction products at the electrode surfaces – all of which are problems in liquid electrolyte designs [18]. However, these recent developments will take time to filter through into commercial products, and the added safety requirements for such energy dense and potentially volatile units can only extend the testing and time to commercialisation of any academic advance.

Active safeguards have been designed to prevent some failure modes in multi-cell Li-ion batteries, but the batteries are still prone to thermal runaway under short circuit conditions with highly explosive results. Thermal stability at high temperatures remains a major challenge to the advancement of the technology [19]. Safety is therefore a significant

concern, and while there is a great effort underway to address it, the solutions are all expected to result in a reduction of specific energy [14].

Lithium batteries are generally not considered an environmental hazard except where they contain other toxic (heavy) metals and are disposed of in large quantities; the lithium mining already observed in countries like Chile, Argentina and China is proving to be less hazardous than alternative mineral extractions – Bolivia's Environmental Defence League believe that Lithium may be one of the least contaminating mining processes [20]. According to a recent literature review for Ecotoxicology and Environmental Safety, lithium is not expected to bio-accumulate and its human and environmental toxicity are low [21]. However, there is currently a large research effort underway investigating the use of both hazardous and non-hazardous materials in novel electrode and electrolyte types, therefore each battery chemistry must be evaluated individually. According to the U.S. geographical survey [www.usgs.gov] the largest reserves of Lithium in the world lie in South America, in Chile and Bolivia. While Chile is already a major exporter, Bolivia has yet to exploit their resource, and therefore may affect price as their production capability comes online.

Currently there is no commercially viable recycling process for used Li-ion batteries, although research is being carried out in this area, mainly prompted by the presence of Cobalt in some of the Li-ion battery chemistries.

1.2 **Battery Management Systems (BMS)**

Recent high-profile cases of battery pack failure include the Tesla roadster Electric Vehicle (EV) Li-ion battery fires, the Boeing 787 Dreamliner Li-ion battery fires and a 2 MW Sodium-Sulphur Battery Uninterruptible Power Supply (UPS) fire at a Mitsubishi Factory in Japan. In the case of the Tesla EV batteries, the fire was caused by road debris puncturing the underbody shielding of the battery compartment, and the physical protection measures functioned as they were designed to by containing the fire within the battery compartment, preventing it from spreading to the passenger zone and directing the flames and hot gasses away from further flammable sources, including other battery sub-modules [22]. As of October 2014 the cause of the Boeing fire is officially unknown as the National Transportation Safety Board (NTSB) continues to investigate [23], although an interim letter of recommendations was released in May 2014 [24].

Figure 1.2- NTSB photos of the burned auxiliary power unit battery from a JAL Boeing 787 that caught fire on Jan. 7 at Boston's Logan International Airport.

Source: http://www.ntsb.gov/investigations/2013/boeing_787/boeing_787.html

The 2 MW Sodium Sulphur Battery UPS fire at Mitsubishi took eight and a half hours to bring under control and a further two weeks to extinguish. The fire was caused by the failure of a single cell module which itself was a part of a 384 cell battery pack. As the faulty cell failed it leaked molten material, which caused a short between adjacent battery cells. The resulting heat caused the whole battery to be compromised [25].

These cases highlight the importance and safety-critical function of the battery BMS and physical protection measures. When a battery pack fails, even when it does so in a pre-calculated and 'safe' manner such as in the case of the Tesla EV the result can be dangerous, and highly damaging to the brand in terms of public perception. Thus we can observe three distinct and significant damaging factors that may arise as a result of poor BMS and/or physical protection measures:

- Loss of/injury to life, and destruction of equipment
- Underperformance of equipment and subsequent damage to public perception
- Premature end of life (EOL) of battery

1.2.1 Function of the BMS

A BMS must perform three broad functions. These functions will be described in the context of a large array of Li-ion cells assembled into a pack, such as is found in a typical Electric Vehicle (EV) application.

Protect cells and battery packs from damage by keeping the battery within its Safe Operating Area (SOA)

Arguably the most important task for the BMS is to maintain a battery pack in a safe state. Battery packs consisting of parallel and series arrays of multiple cells can have very high energy density and have the potential to deliver large fault currents, which could lead to catastrophic temperature rises and cascading failure of the cells. Manufacturers minimise this risk by creating sub-modules within larger battery packs, with features such as physical firewalls and fuses between modules, vents to control the direction of hot gasses and flames in the event of fire, and armour plating to protect against puncturing [22].

In tandem to these physical safety measures, the BMS monitors pack electrical and thermal conditions to ensure that individual cells are kept within specification. Upper and lower

voltage limits, maximum continuous charge/discharge currents and pulse currents are chemistry-specific and given in cell manufacturers datasheets alongside operational temperature ranges.

Maintain the battery to meet the requirements of its application

The operating conditions just described are those which must be adhered to in order to maintain safe functioning of the battery pack. Ensuring that these limits are enforced is a coarse function of the BMS, but its value extends beyond safety and the BMS may perform secondary and tertiary functions depending on the application. For instance the BMS in a laptop will alert the user when the State of Charge (SoC) reaches a critically low level. Once the SoC drops to a predefined level then the BMS might switch to energy saving mode, disabling inessential services before eventually taking control from the user and executing a safe shutdown sequence in order that the system be put into a safe state while there is still battery power to do so. Then the BMS isolates the battery from any new demands until it has been recharged to a predefined minimum SoC.

Maintain the cells and battery packs to maximise the lifetime of the battery

A third function of the BMS is to prolong the useable life of the battery. Observing safety limits and application-specific functional limits may be considered the primary and secondary tasks for the BMS, while a useful tertiary task is to extend the life of the battery pack. There may be some overlap between the secondary and tertiary function of the BMS, and the mechanisms it uses to achieve these include battery equalisation, heating, cooling and controlling the distribution of load demand amongst the cells.

1.2.2   Key Estimation Metrics

An important branch of battery research is that of estimating the state, or condition of the battery at any given time. End users in many applications require accurate and reliable means of assessing the State of Charge (SoC) of their battery; from mobile phone users and laptop users through to Electric Vehicle (EV) drivers, Unmanned Aerial Vehicle (UAV) operators and large plant (>1 MW Uninterruptible Power Supplies (UPS)).

Compare the task of estimating the remaining range of an Internal Combustion engine car, based on the fuel available in the tank, with the same task of estimating the range of an

Electric Vehicle based on the charge remaining in the battery. Clearly the biggest influence on the range in each case will be the volume of fuel in the tank, and the amount of available charge in the battery respectively. Measuring the quantity of fuel in a tank is a relatively simple task and one that can be achieved with a high degree of accuracy. Furthermore, the rate at which fuel is consumed has no effect on the remaining capacity. Measuring the charge remaining in a battery is a more complex task; State of Charge of a battery is not a fixed quantity but is dependent on variables such as temperature, rate of discharge/charge, cycle history of the battery, and battery form factor among other things.

When measuring and/or estimating battery states, the measurable quantities are cell voltage, current and temperature. These inputs are then often used to feed look-up-tables or estimator algorithms, frequently based on knowledge of prior load-cycle history. Returning to the examples given at the beginning of this section, mobile phone users will be aware of the frustration arising from a bad estimator algorithm – when the phone charge indicator suddenly jumps from 50 % to empty it does not necessarily follow that 50 % of the available capacity has been used in a disproportionally short amount of time, but it may instead mean that the estimation calculation is inadequate to cover all operating conditions. In the case of an EV operator an insufficient SoC estimation algorithm may leave them stranded - a UAV operator may lose their vehicle.

1.2.2.1 *Battery Metrics*

Battery *State-of-Charge, SoC* is a measure of the remaining useful charge in a battery pack, usually given as a percentage of maximum possible charge. The charge capacity of a battery declines throughout its life-cycle therefore an accurate estimation of SoC requires that the present maximum charge capacity of the battery be known, as well as the amount of useable charge remaining. Therefore another metric is required to track these changes in charge capacity – and feed the calculation of SoC estimates - as it decreases from the nominal capacity of a new battery; Battery *State-of-Health, SoH* is a parameter that reflects the present condition of an ageing battery in comparison with a new battery. As well as declining capacity, other parameters change over the lifetime of a battery. Internal resistance increases, maximum available power declines and the capability to support a given load is diminished. A third useful metric is *State-of-Function, SoF*, which is a measure of the battery's capability to perform a specific duty in support of the functionality of a system which is powered by the battery. SoF is a function of SoC, SoH and battery temperature.

1.2.3   Battery State Estimation Tools

As battery technology develops and progresses, so too the techniques of estimating the remaining charge have to be adapted. What works well when applied to one chemistry may not be suitable for another, and for this reason there is a large amount of ongoing research directed at estimation methods. Each time a new chemistry is developed - or even simply a new form factor of the same cell chemistry – existing models and estimation techniques must be updated.

The following is an overview of popular estimation tools which can be categorised into *direct* methods, a *book-keeping* approach, and *adaptive* techniques which comprise several estimation methods in combination.

1.2.3.1   Direct

Historically, battery state measurements began primitively with simple direct voltage measurements.
The voltage drop across an external power resistor was measured and compared with the unloaded terminal voltage. In a healthy battery the on-load voltage drop would be minimal, while a large drop would indicate the need for the battery to be recharged or - in the case of a primary battery - replaced. Over the years since these first techniques were developed in 1938 [26] a number of different methods of state estimation have been devised and often used in combinations of two or more to improve the accuracy of the estimates. The most widely employed direct measurement techniques are presented here.

1.2.3.1.1 Battery and Cell Voltage Measurements

As a battery becomes depleted the terminal voltage drops. It is reasonable to expect therefore that terminal voltage might provide a good indicator of the SoC of a battery or cell, and indeed it is possible to infer the SoC from this data, however the task is complicated by the fact that the voltage is heavily dependent on cell temperature and rate of charge/discharge. If the cell temperature and discharge rate are both known then the error can be corrected, albeit at the expense of increased cost and processing complexity without any significant advantages over other available approaches such as coulomb counting.

1.2.3.1.2   Electromotive Force (EMF)

The EMF of a Li-ion battery (the open circuit voltage, OCV, under steady-state, no-load conditions) can be used as a SoC metric, since the relationship between SoC and EMF is nearly constant over the lifetime of a battery and there is only a small temperature dependence near the extremes of full charge and empty [26]. Figure 1.3 gives an example of the EMF characteristic for five different chemistries.
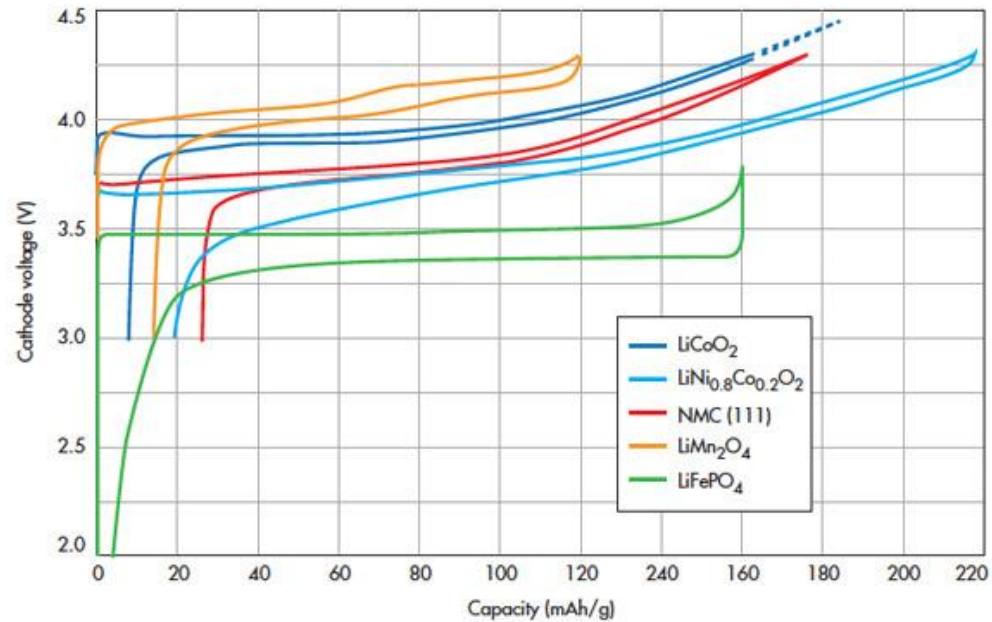
Figure 1.3 - Charge and Discharge Curves for Various Lithium-ion Cell Chemistries.

Source:www.electronicdesign.com/power/understanding-factors-lithium-battery-

From Figure 1.3 we can observe that while a number of EMF curves have a steady or significant slope, the EMF curve of a C/LFP battery is quite flat. From an application's perspective this is a desirable feature, as it means that the supply voltage is more constant over a wider SoC range, i.e. it performs better at its intended role of being a voltage source. However from a SoC estimation point of view this causes a reduction in the accuracy of the estimation, as the EMF varies less over a wider SoC range. Furthermore, obtaining an accurate EMF measurement can be problematic.

The current demand on the battery must be reduced to zero in order to make an accurate, off-line EMF measurement. This *voltage relaxation* method of obtaining the internal driving force of the battery requires a time period of off-line battery relaxation – typically 3 hours for C/LFP - to allow the battery voltage to reach steady-state; the required relaxation time is extended significantly if the battery has been subjected to a high load current, low temperature, or if it is near fully discharged. For many applications this rules out the use of voltage relaxation as a method of obtaining the EMF.

An EMF approximation may also be obtained by *linear extrapolation* of terminal voltages measured under different load current rates, thereby approximating the terminal voltage at zero current, but a further complication in the case of some batteries - such as C/LFP and Ni-MH - is that the measured OCV exhibits a hysteresis effect which is dependent on whether the battery is being charged or discharged [27] (see Figure 1.3 for an example of cell voltage hysteresis). Knowledge of cycle history may also be required in these cases unless an adaptive method is also implemented [28] (see section 2.3.3).

Linear interpolation may be used to determine the mean battery voltage over two consecutive charge/discharge cycles, thereby nulling the effects of hysteresis.

Two practical SoC estimation techniques involving the use of EMF data are the *look-up table* and the *piecewise linear function.* The look-up table is based on laboratory measurements of SoC values stored alongside corresponding EMF data. In the laboratory accurate SoC can easily be determined by running a full discharge or charge test on a battery, but this is of no practical use in an online situation when the battery is in use. Instead, the results of prior full charge/discharge cycles done in the laboratory are used to populate look-up tables. Clearly the look-up table approach will yield the best results when it includes more data points, but again this increases the complexity and expense of the process involved.

The piecewise linear function is a compromise between the accuracy of the look-up table and the expense of including an exhaustive data-set. The EMF curve here is approximated with piecewise linear functions, and the accuracy of the SoC measurements obtained is dependent on the number of intervals chosen.

1.2.3.1.3 Model-based SoC Estimation

The model-based approach to estimation removes the requirement for direct offline EMF measurement by taking into account the internal resistance of the cell or battery pack. Models can be broadly classified into three types: First principle models, Equivalent circuit models, and Black-box models [29].

Equivalent circuit models are often used [30–47] which express the relationship between EMF and dynamic data in terms of the linear differential equations of RC circuits and discrete-time dynamic equations of the cell model [44].

1.2.3.1.4 Impedance Measurements

Impedance measurements over a wide range of frequencies can provide a means of identifying the physiochemical processes in an electrochemical system. Electrochemical Impedance Spectroscopy (EIS) allows equivalent circuit parameters to be extracted which in turn may be correlated with physiochemical processes within cells.

As a battery is discharged, observed changes in the impedance spectrum can be used to identify SoC. Also, changes in impedance can be correlated to ageing effects within the battery and therefore feed SoH and SoF estimations.

Impedance measurements and analysis form the main body of the author's work, and will be discussed in more detail in section 3.

1.2.3.2 *Book-keeping (Coulomb Counting)*

This approach to indicating battery SoC relies on monitoring the charge flowing in or out of the battery. Battery current is continuously measured and integrated, while other battery data may also be used to feed the book-keeping system and compensate for temperature effects, cycle life and self-discharge rate. Equation 1 is an example of a SoC calculation that is based on knowledge of prior SoC at time t_0, SoC_0, the nominal capacity of the battery, C_n, and the battery current I. The coulombic efficiency η varies with temperature, battery current, SoC, and SoH.

$$SoC = SoC_0 - \frac{1}{C_n}\int_{t_0}^{t}\eta I \cdot d\tau$$

Equation 1

Inspection of Equation 1 reveals some weaknesses in this method. Any errors in measuring either coulombic efficiency (η) or battery current (I) will produce a cumulative error in the SoC result, while an error in the initial SoC_0 carries through and affects the precision of the final SoC estimation. The precision of this method is reliant on the precision of the current sensor, the acquisition frequency, and frequent calibration checks to ensure that SoC_o is accurate and to compensate for any errors in the estimation of η. Nevertheless the book-keeping approach is widely used, with the shortcomings described here compensated for by use of other techniques, such as using an adaptive algorithm to prevent errors becoming cumulative.

1.2.3.3   *Adaptive*

As has been described here, the remaining useful charge in a battery is highly dependent on future demand and operating conditions, which in some cases such as a portable music player may be easy to predict while in others, such as EVs, can be highly unpredictable. For this reason, if the implementation cost (processing and monetary costs) can be justified then an adaptive approach may be taken, often comprising more than one measurement type – for example an OCV approximation method may be combined with coulomb counting, and an adaptive approach would compare the resulting estimated values with observed response and inform the new estimates accordingly.

1.2.3.3.1   *Fuzzy Logic*

The Fuzzy Logic (FL) system uses subjective rules to produce 'crisp' outputs from data sets having uncertain values ('fuzzy' sets). A cell voltage, absolute temperature, or load current would all be considered 'crisp' data, whereas fuzzy sets have less certain categories of data. A fuzzy set might include the subsets 'Poor' or 'Very Poor' to describe SoH (see Figure 1.4), and an element of the set 'SoH' might belong to different subsets by various degrees of 'membership'. Identifying the fit of real-valued data into this fuzzy set is called the 'fuzzification' of the data.
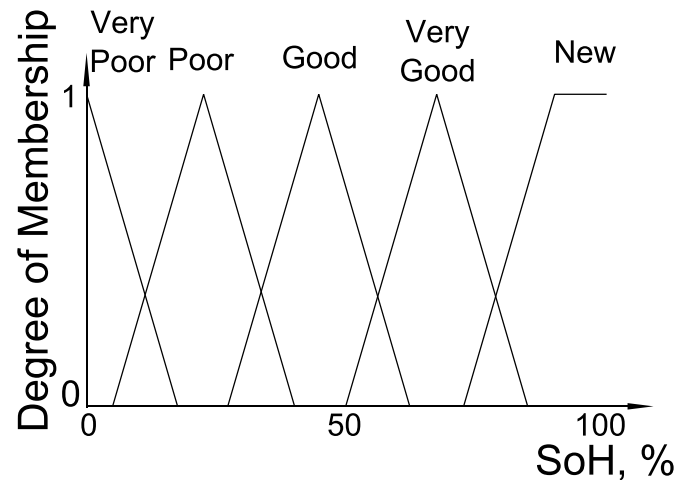
Figure 1.4 - An example of membership function for State of Health

Figure 1.5 shows broadly the steps involved in obtaining a crisp output; the inputs to the FL system may for example be impedance and temperature (and previous FL outputs fed back), and the desired output might be percentage SoH. Fuzzy outputs are generated by inference using subjective 'if…then' rules written in a linguistic format, along with a database that defines membership functions for input and output variables. The defuzzification step produces real-valued crisp data (such as % SoH) from the fuzzy output.

A downside of FL is the relatively large processing power required [26]. Watrin et al provide an overview in their review paper [48], while [49–51] are examples of the use of FL in battery prognostics.
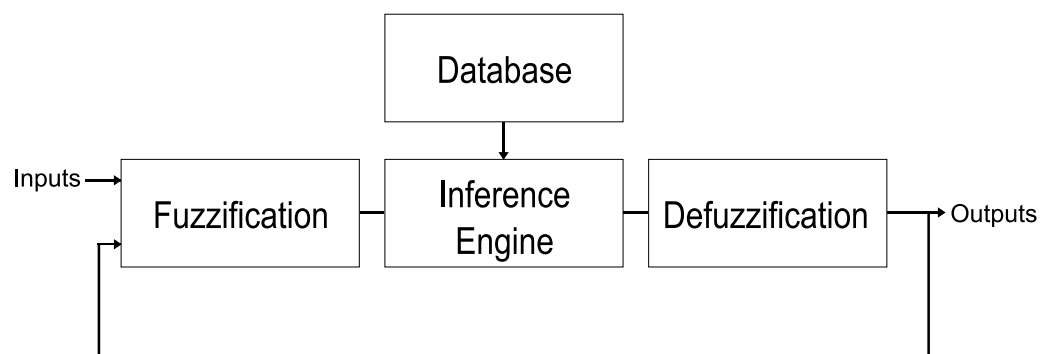
Figure 1.5 – An overview of the Fuzzy Logic Process

1.2.3.3.2 *Artificial Neural Network (ANN)*

A key advantage of the neural network model is that it can be universally applied, irrespective of the battery chemistry. SoC is estimated using the non-linear mapping characteristics of the neural network [52], and the construction of the model does not need to include the prior input of battery-specific information; indeed, because of the large amount of training data that is required the ANN model can also reveal SoH information, but it is the large amount of training information (typically upwards of 1000 cycles [53]) that is a key disadvantage of this method. Processing power may also be a limiting factor to implementation, however some of the advantages of the ANN approach are obtainable without the need for complex processing if the adaptive aspect is not required [53] to estimate individual behaviour.

1.2.3.3.3 *Kalman Filter (KF) and Extended Kalman Filter (EKF)*

This method uses an algorithm which can estimate system states that are not directly measurable, such as SoC or SoH, and can also be useful in minimising measurement noise effects [48]. Kalman Filters are used in the analysis of stochastic and linear signals, but adaptations can be made to allow their use in solving non-linear problems such as those presented by battery SoC estimation, one of which is the Extended Kalman Filter (EKF). Examples of successful application of these filters in the online estimation of SoC and SoH of lead-acid batteries can be found in [54–58].

The algorithm comprises several equations that estimate a measurable value which is then compared to a real measurement of the value and the estimated value is subsequently corrected. Accurate cell models must be developed, and these are often simplified equivalent circuit models with minimal parameters to ensure a fast computing process.

1.3 **Electrochemical Impedance Spectroscopy (EIS)**

As mentioned previously, EIS allows equivalent circuit parameters to be extracted which in turn may be correlated with physiochemical processes within cells. Detailed electrochemical models are often not required, and are themselves problematic in embedded applications due to their complexity – see [59].

Observed changes in the impedance spectrum of a cell can be used to identify SoC and can also be correlated to ageing effects within the battery, thus feeding SoH and SoF estimations. Here we look at this relationship.

1.3.1 The Relationship between Battery Impedance and Battery Dynamics
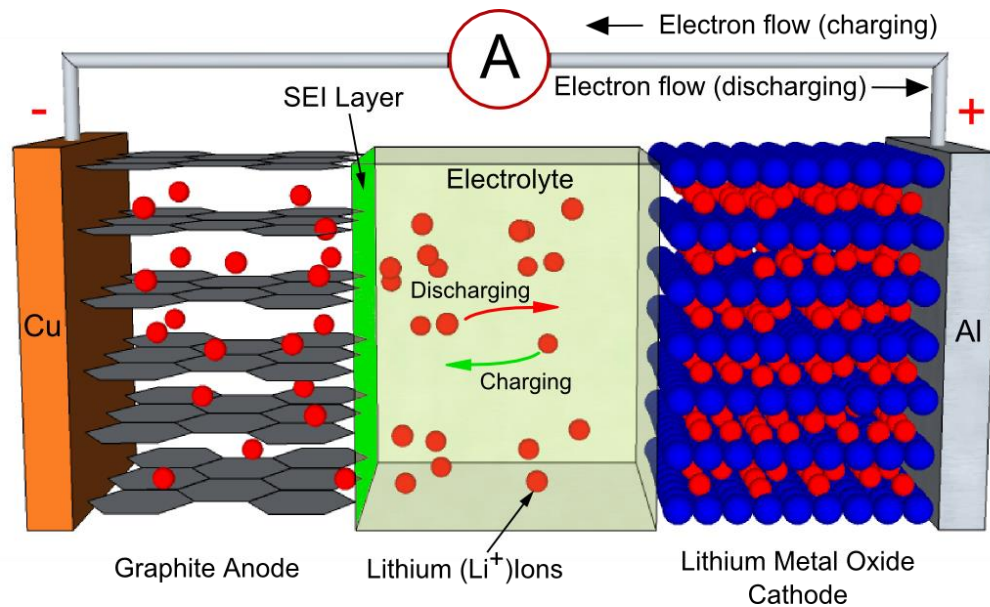
Figure 1.6 – The major components of a Lithium-Ion Cell

Referring to Figure 1.6, a typical lithium cell is comprised of two porous electrodes, metal current collectors, and lithium ions suspended in a non-aqueous electrolyte. On first charge a thin film called the Solid Electrolyte Interface (SEI) forms on the surface of the anode and this has a significant effect on the electric characteristic of the cell, because the lithium ions must diffuse through this layer. This is one of several diffusion mechanisms which are known collectively as mass transport effects. Other locations where diffusion occurs are within the porous electrodes – so that electrode geometry greatly affects cell dynamic behaviour – and

within the free electrolyte. Generally, mass transport effects are observed at sub-1 Hz frequencies, as seen in the impedance plot of Figure 1.7. As the cell ages, this SEI layer changes and the dynamic characteristic changes with it, with the result that the ageing process can be correlated to a change in the slope of this region. Temperature also has a large influence over the diffusion mechanisms and low frequency impedance.
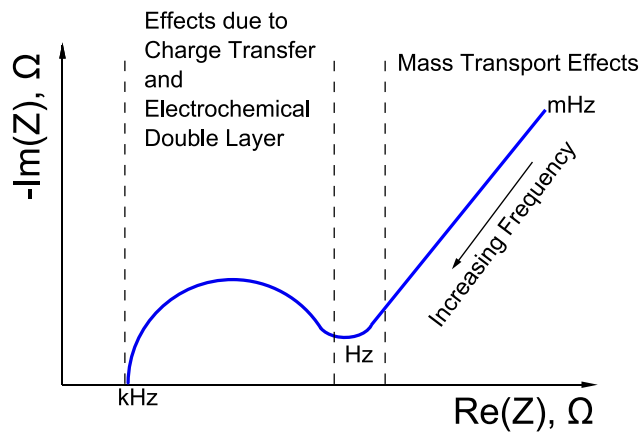
Figure 1.7 – A typical Li-Ion Nyquist impedance plot, showing identifiable characteristics of dynamic mechanisms in a new cell

At the interface between electrode and electrolyte an area of charge forms a layer, causing an effect similar to a capacitor due to the large surface area of the electrodes and because of the short separation. This is known as the electrochemical double-layer [60] and is responsible for the characteristic semicircle response seen in Figure 1.7 which is similar to that produced by a simple RC circuit (an RC impedance is a semicircle on a Nyquist plot).

So we begin to see the importance of impedance spectroscopy in the analysis of the state of charge and health of batteries, and how simple equivalent circuit models can be used to represent some real electrochemical mechanisms and ageing process within the cells. These modelling techniques will be expanded in chapter 4.

1.3.2   Standard Laboratory EIS Techniques

1.3.2.1   Swept Frequency Sine

The most common, standard approach to measuring impedance is to measure the system response to a small voltage or current stimulus of fixed frequency. The phase and amplitude of the response can easily be manipulated using fast Fourier transform (FFT) techniques to give the impedance as a function of frequency. An impedance spectrum of the system can be constructed by repeating the test over a range of frequencies; commercial instruments are available that sweep the frequency in the range of typically 1 mHz to 1 MHz, and directly produce an impedance spectrum in the form of a bode diagram or a Nyquist plot. The signal to noise ratio of this method is excellent - since frequencies of interest can be directly specified – however the measurement time required can be prohibitively long when low frequency data is needed [61]; low frequency response is an important aspect of the frequency response function (FRF) of an electrochemical cell [60].Ω

1.3.2.2   Transient Measurements

Another method involves applying a voltage step-function (this is potentiostatic mode; in galvanostatic mode a current step-function is used instead) *V (t<0, V=0; t>0, V=V$_0$)* to the battery and measuring the resultant time-varying current i*(t)*. The quantity *V$_0$/i(t)* is often called the indicial impedance, or time-varying resistance [62], and usually transformed into the frequency domain to show the frequency dependent impedance. The excitation in this case is non-periodical and therefore a suitable windowing function must be used to correct distortion in the impedance spectra. Another requirement is that *V$_0$* is kept sufficiently small that a linear system response is ensured.

1.3.2.3   White Noise Stimulation and Broadband Excitation

A signal composed of true white (random) noise will stimulate a system equally at all frequencies. Furthermore, this description can be relaxed to say that the requirement for a stimulus to be considered a white noise input to a system is that it has a flat power density spectrum over a frequency range much greater than the system bandwidth [63]. A stimulus of this type (i.e. one possessing a uniform power spectrum) will produce a system response

that can readily be manipulated into providing the system frequency response using Fourier analysis.

There are three important advantages to this method of system identification over the two conventional methods described above [63]:

1. The system (battery) may be allowed to remain in its normal functioning mode, since the noise excitation is spread over a wide bandwidth and is necessarily of a low intensity so that the system is maintained operating within its linear region.
2. Measurements are not affected by other sources of noise, provided they are stochastically independent of the input noise source.
3. Stored energy in the system has no effect on the measurement of the impulse response.

However, there are two important disadvantages to this method. Accurate estimates of the cross-correlation function still require that the stimulus and response are measured for a long (ideally infinite) amount of time. Second, the stimulus energy must be kept small to ensure an approximately linear response is measured from a non-linear system. This increases the accuracy required in the measurement of the stimulus and response signals.

The measurement of the frequency response function (FRF) via broadband excitations has been demonstrated to take significantly less time than when using stepped sinusoidal excitation [64], given good signal-to-noise ratio (SNR) (this time advantage is reduced when the SNR is poor).

1.3.3 *Pseudo-Random Binary Sequences (PRBS) as Pseudo-White Noise Input*

A pseudo-random noise source produces a frequency response that is similar to white noise except that it is produced deterministically and is therefore periodic, and the power spectral response is therefore only flat across a specific bandwidth; it is considered to be a source of band-limited white noise.

A key reason for the early adoption and continued success of PRBS is that the signal can be generated easily with a minimum of digital hardware using simple shift register circuitry and appropriate feedback (see Figure 1.8). While several classes of pseudo-random binary

sequences exist [65], maximum length sequences (MLS) are the class of PRBS signals that are generated in this way and will be referred to as PRBS throughout this document.
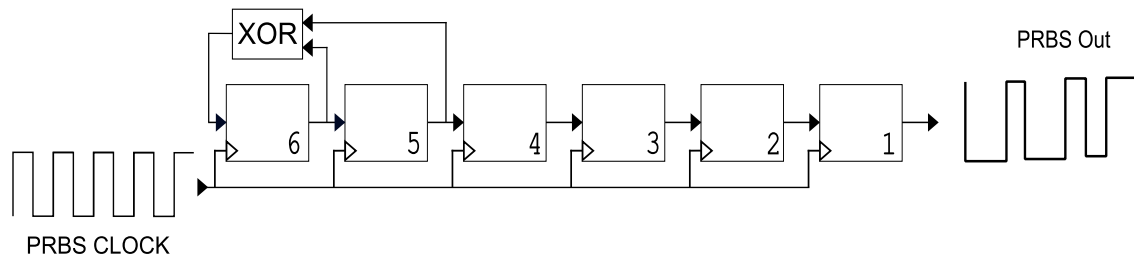
Figure 1.8 – 6-bit shift register showing the feedback tap connections used to produce a maximum-length sequence (MLS)

A shift register containing *n* storage elements will produce sequences of length $N = 2^n - 1$. Thus the shift register shown in Figure 1.8 will produce an $N = 2^6 - 1 = 63\,bit$ PRBS such as that seen in Figure 1.9.
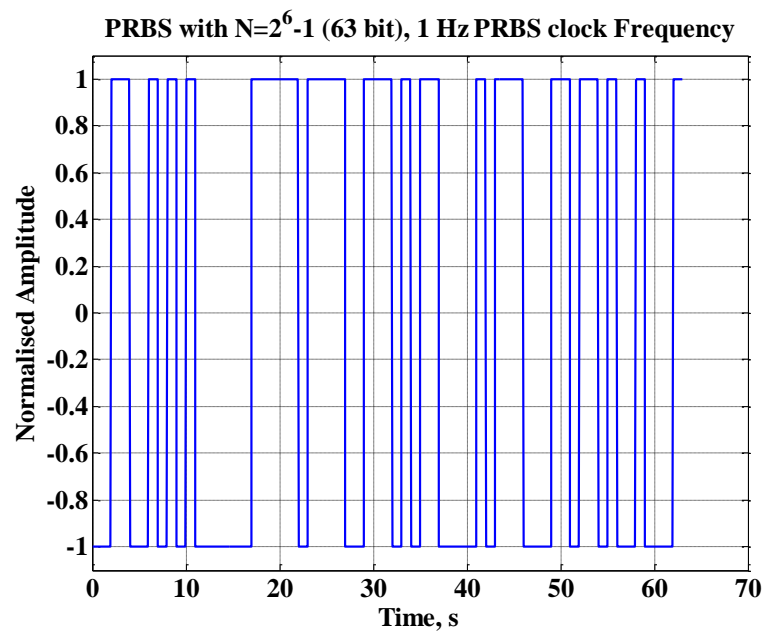
Figure 1.9 – A 1 Hz bipolar PRBS signal produced from a 6-bit shift register

The power spectral density of this signal is shown in Figure 1.10, where it has been normalised to show the power density as a function of generator clock frequency. The fourier transform of a periodic signal is a line spectrum having values at frequencies of $f = k / T \ Hz$ only, T being the period of one complete sequence and k an integer. These discrete values are given by Equation 2, as shown by [63], [65], where V is the amplitude and f_{CLK} is the shift register clock (the bit-rate of the PRBS stream).

$$S_{xx}(f) = \frac{V^2}{f_{CLK}} \frac{N+1}{N} \left(\frac{\sin(f \pi / f_{CLK})}{f \pi / f_{CLK}} \right)^2$$

Equation 2
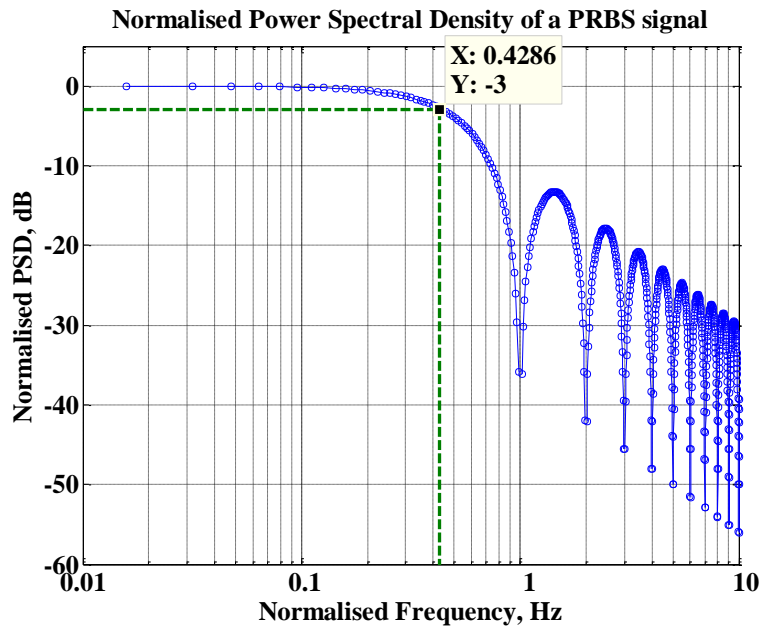
Figure 1.10 – Normalised PSD of the PRBS signal seen in Figure 1.9

Note that at the reciprocal of the clock period or its integer multiples, there is no power in the signal. It has also been shown [65] that as N increases, $S_{xx}(0) \rightarrow 0$ and the power in the first harmonic converges towards $\frac{2V^2}{N}$. The slower decay of the spectrum as k increases gives the desired flat response over the system bandwidth, the half-power point of which is

approximately $0.443 \times f_{CLK}$. In Figure 1.10 above this value is 0.429, as the PSD was produced by an N=63 (6-bit) PRBS shift register.

As stated previously, this method of system identification offers an advantage in the ability to stimulate many frequencies simultaneously with even power, reducing measurement time. A battery or cell can more easily be kept within a linear region of operation throughout the identification process, and the impedance spectrum is easily obtained by dividing the power spectrum of the voltage response with that of the current stimulus (assuming a current controlled excitation). Examples of the technique can be found in [66], [67].

1.4 **Conclusions**

A brief history of popular EV battery chemistries has been presented, along with a description of Battery Management Systems and state estimation techniques. PRBS methods of EI Spectroscopy have been introduced, forming a motive for the work presented in the next chapters. In Chapter 2 there is a description of the equipment that was developed for purposes of charge cycling and impedance measurement of a range of Li-ion cells. The results of tests on two types of cell, LFP 26650E 3 Ah cells and LTO polymer 100 Ah pouch cells, are presented. The author's main findings from the early work precede Chapter 3, which gives details of the new hardware – and corresponding control software - that was developed to address the weaknesses of the first designs. Concluding remarks and suggestions for further work are given in Chapter 4.

.

Chapter 2: Battery Charge Cycler and PRBS Impedance Measurement System

2.1   Objectives

As part of a TSB funded battery project, a test rig capable of cycling Li-ion cells, and measuring their impedance using PRBS as an EIS stimulus was to be built. As there was some pre-existing hardware that could be modified and re-purposed, the task was split into two parts – high current charge cycling, and low current PRBS measurements.

The high current cycling rig was intended to be capable of testing a single Li-ion cell (nominal voltage < 10 V) at pulse currents up to 150 A, and charge cycling the cells at a lower rate of up to 50 A continuously. A PID controlled temperature environment was supplied so that tests could be conducted at temperatures in the range -10$^{\text{o}}$ C to 50$^{\text{o}}$ C. The intention was to test actual cell capacities when cycled at a rate of C/2 (C being nominal cell capacity - e.g. 3 Ah - and the 'C rate' being C/1 hour - e.g. 3 A), and identify the maximum current a cell could accept before reaching maximum/minimum permitted voltages at various SoC (10 % increments). PRBS impedance tests would also be done at each SoC and temperature. Later uses included testing battery packs up to 28.8 V (24 V nominal LFP packs).

The high current rig was used to cycle the cells and bring them to a known SoC. With a cell discharged to a known SoC, the cell could then be taken offline from the high current rig and a PRBS impedance test performed using the smaller rig; the SoC of the cell must not be changed significantly as a result of the impedance test, therefore only low currents could be used to measure the impedance. The system identification aspect of the test relies on being able to make a linear approximation of the non-linear cell.

Therefore, the focus here will be on the procedures that were followed during this phase of the work; there is a critique at the end of the chapter that will hopefully illuminate some of the decisions and changes that were made, prior to later work.

2.2   **High Current Cycling Rig**

Time constraints within the original project meant that the cycling rig was to be made by modifying an existing 4 x parallel power MOSFET half-bridge. This half-bridge was already mounted on a large forced air cooled heatsink, therefore providing a suitable base construction onto which power resistors could be mounted. A control board which had previously been developed for a similar architecture 500 A rig was used to convert a current demand signal into a control signal for the power MOSFETs (Figure 2.1 - Control Board and Single Output (One of Four),Figure 2.1).
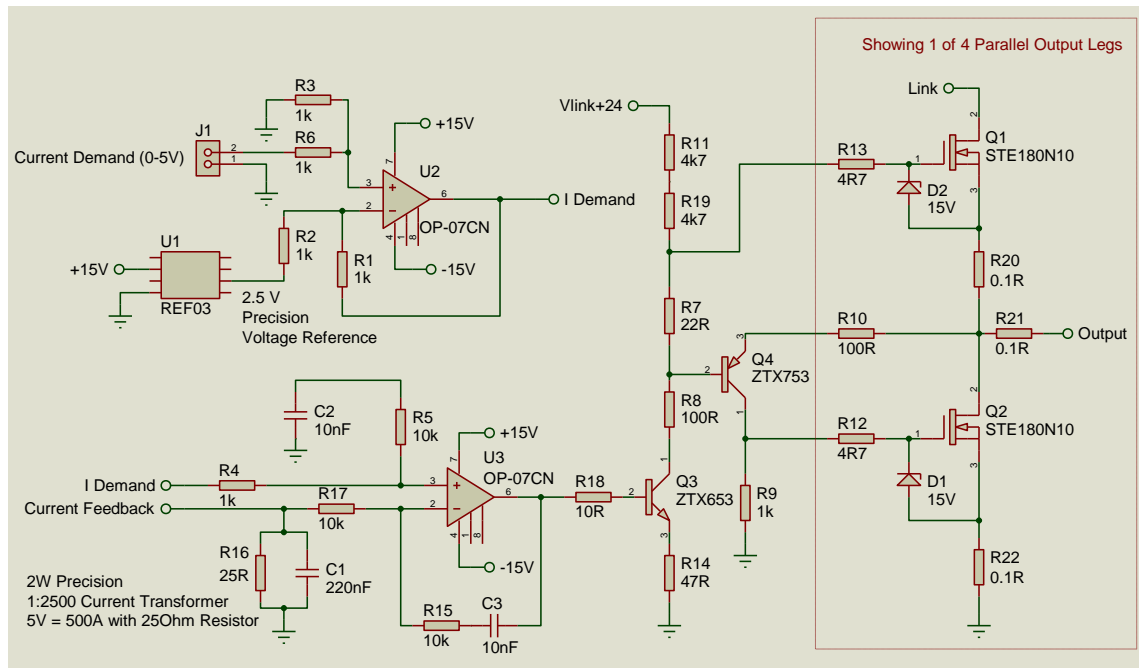
Figure 2.1 - Control Board and Single Output (One of Four),

Modified From an original design by Prof. D. A. Stone

In this circuit, J1, U1 and U2 form the demand input, 2.5 V reference voltage (to allow bi-directional current control from a 0-5 V demand signal) and unity gain buffer respectively. This demand signal is then passed to U3, where it is compared with the current feedback which is generated from a 1:2500 turn current transformer attached to the output current conductor. The generated current then develops a voltage across R16 (a 25 Ω precision resistor) of 1 V per 100 A output current.

The output of U3 feeds the gate drive circuit formed by Q3, Q4, and their associated resistor network. This circuit ensures that both high and low side MOSFETs can turn fully off (the network is fed by a voltage 24 V above the DC link voltage), and eliminates the possibility of shoot-through occurring since only one set of output devices (high or low) may be conducting at any time.

The output MOSFETs are each rated for 120 A continuous drain current at 100° C (540 A pulsed), and 450 W total dissipation at 25° C. As there were four parallel channels mounted on a large forced-air heatsink, this was deemed sufficient for our purposes (150 A pulses) with no further calculations. The system was tested up to a link voltage of 35 V, to allow testing of 24 V nominal LFP batteries (28.8 V max battery under test voltage).

Acquisition of charge cycling signals (cell current and terminal voltage) is done using a NI USB 6009 14-bit DAQ, at a sample rate of 100 Hz.

2.3 PRBS Impedance Test Rig

The impedance tester is a separate circuit to the charge cycler. When an impedance test is required, the battery under test is isolated from the charge cycler using a Kilovac relay and control of the battery current transfers to the PRBS control board, which is capable of drawing up to 2 A from the battery. At this stage of the research the PRBS tests used were unipolar - discharging the battery only – therefore to minimise state changes while performing system identification tests, low stimulus currents were used.
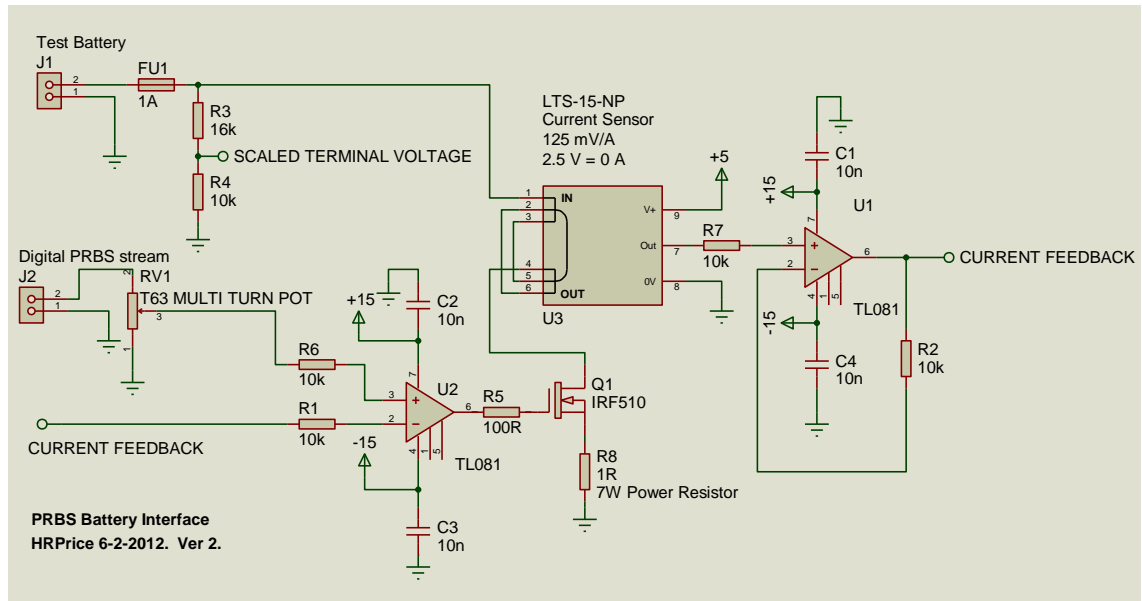
Figure 2.2 – PRBS load control

The circuit in Figure 2.2 shows the initial design of the PRBS test circuit. The digital PRBS stream is generated using an Arduino ATmega 2560 based microcontroller producing 0 V (low) and 5 V (high) on a digital pin as it sequentially reads each bit from a 63-bit PRBS sequence stored in memory. Different PRBS clock frequencies are generated by specifying the delay time of a loop which steps through the sequence in memory.

Stability problems in early testing meant that the current feedback arrangement shown was changed; R8 was used to provide 1 V/A feedback for the control loop, while the output of U1 was reserved purely for current measurement purposes. RV1 is used to scale the input demand signal so that a 5 V (high) input produces 1 A discharge current in the battery.

During impedance testing, control of the current demand and data acquisition is transferred to a MATLAB script which sends a start trigger to the Arduino, and begins streaming acquisition on a LabJack U6. The U6 was configured to acquire differential current and voltage readings (total of four channels) at 5 kS/s, at which rate it is capable of 14-bit resolution.

Figure 2.3 – Cycling Rig and PRBS Impedance Tester

2.4 Test Procedure
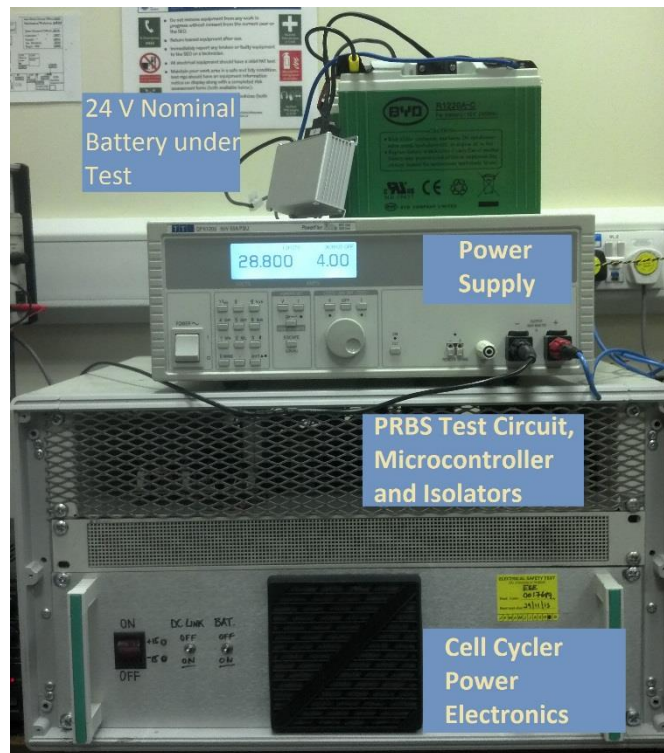
The test method for measuring impedance at different SoC follows the following format. Note that 'C' refers to the amp-hour capacity of the cell, thus a rate of 1C is equivalent to a full charge or discharge in one hour (example values for 3 Ah LFP cells are used in parentheses):

1. The cells are discharged at a C/2 rate until the low voltage cut-off (2.6 V) is reached.
2. Cells are charged at a C/2 rate up to their maximum voltage cut off, and held there until the current reduces to a value of 3 % of C (90 mA for a 3Ah cell).
3. The cells are again discharged at C/2 rate until they reach the low voltage cut-off (2.6 V for LFP cells).
4. Step 2 is repeated, and the cell is now considered to be at 100 % SoC.
5. The cell is taken offline for a set amount of time (at least 30 minutes, preferably of the order of hours). This is the relaxation (rest) time, which allows the terminal voltage to settle to a steady state.
6. An OCV reading is taken, then the cell is brought back online.
7. A PRBS impedance test is begun. This is broken into eight separate sequences of the same 63-bit MLS, at bit rates from 1 kHz to 1 Hz (see full description in section 2.5.1), which lasts 96 seconds. These are then repeated and it is the data from the second set which is then used (as the cell terminal voltage has then settled from its initial 'on load' voltage drop into a steady load state) making the total impedance test time around 200 seconds.
8. The test then enters a repetitive cycle until the low voltage cut-off is reached:
   a. The cell is discharged by 10 % of its nominal capacity (300 mAh for a 3 Ah cell).
   b. Taken offline for a preset rest period (e.g. 30 minutes – same as step 5).
   c. PRBS impedance test.
9. Once the cell has reached 0 % SoC (e.g. LFP cell terminal voltage reaches 2.6 V) step 8a is terminated and steps 8b and 8c are allowed to execute a final time.
10. The cell is re-charged to 30% SoC (ideal storage state for Li-ion cells).

2.5   Impedance Tests

2.5.1   Stimulus Signals

The use of PRBS as a stimulus for EIS impedance measurement has been discussed in section 1.3. Table 2.1 shows the frequencies used and the resulting bandwidth of impedance measurable from each sequence.

Sequence #	PRBS Clock Frequency	Useful Frequency Range After Processing	Test Duration for 63 bit PRBS (single stream)
1 (9)	1 kHz	16 Hz – 330 Hz	63 ms
2 (10)	143 Hz	2.3 Hz – 47 Hz	440 ms
3 (11)	111 Hz	1.8 Hz – 37 Hz	570 ms
4 (12)	55.6 Hz	0.9 Hz – 18 Hz	1.13 s
5 (13)	25 Hz	0.4 Hz – 8.3 Hz	2.52 s
6 (14)	12.8 Hz	0.25 Hz – 4.2 Hz	4.91 s
7 (15)	4 Hz	65 mHz – 1.3 Hz	15.8 s
8 (16)	1 Hz	16 mHz – 330 mHz	63 s

Table 2.1 – Chosen PRBS Clock Frequencies and Resultant Bandwidth of Spectrum

The test consists of two cycles of eight PRBS stimulus streams (16 total), and the post-processing is done on the final eight sequences – this allows the cell to recover from the initially severe voltage drop which results from being subjected to a load after being at rest. Differential measurement of terminal response voltage and stimulus current is done at 5 kS/s.

2.5.2   Post-Processing

Following a typical test such as that outlined in Section 2.4, one data file for each impedance test is generated. These contain the terminal voltage measured prior to the test, the SoC and temperature of the cell, and a data array consisting of [time, stimulus current, and response voltage]. The data array contains a continuous stream of all 16 sequences.

The following is an outline of the process involved in generating an impedance spectrum from a single set of 8 PRBS stimulus and response signals, the results of which follow in the next chapter.

1. In order to identify the complete data sequences exactly, the 16 individual stimulus and response signals are extracted from the data array by cross-correlating the array with a clean reference signal for each PRBS clock frequency. The final set of eight sequences are used.

2. A DFT of the current and voltage, yields a signal power spectrum for each sequence.

3. The impedance spectrum (now in the frequency domain) is obtained by V/I.

4. The obtained spectrum is band limited to the useful frequency ranges listed in Table 2.1.

5. The eight spectrums are combined and averaged to yield the impedance spectrum for the cell.

2.6 **Results**

The primary purpose of the work was to characterise various 3.2 V - 3 Ah 26650E LiFePO$_4$ cells, although the intention was that the equipment be versatile enough to test other cells, such as 24 V - 20 Ah LFP battery packs, 100 Ah – 3.7 V LTO polymer (pouch) SLPB cells, and 6 V – 24 Ah lead-acid batteries.

Presented here is a summary of the early tests done on the 26650E LFP cells, and the high capacity SLPB LTO cells. In both cases impedance vs. SoC tests were run, along with basic SoH tests done by comparing the impedance spectrums of a new cell and an aged cell.

Following the presentation of the results of this early work is a discussion of the problems encountered and the weaknesses found in the test methods and resulting data.

2.6.1   26650E LiFePO₄ (LFP) Cells

These 3 Ah cells have a nominal voltage of 3.2 V. Table 2.2 lists the condition of the cells and the test configuration used (single or parallel), along with the reference numbers used in this section. Note that cell 1 was damaged during testing and was therefore only tested at 10°C, 20°C and 30°C. All other cells and configurations were tested to 50°C.

Cell Reference #	Description
1	New cell, damaged during testing – incomplete dataset (< 30 cycles)
2	New cell – lightly cycled (< 30 cycles)
3	New cell – lightly cycled (< 30 cycles)
4	New cell (0 cycles)
5	End of Life (EOL) cell (2300 cycles)
23	Cells 2 and 3 in Parallel
234	Cells 2,3 and 4 in Parallel

Table 2.2 - Cell Reference Table

2.6.1.1   *Discharge data*

A typical pulsed current discharge (PDC) curve is shown in Figure 2.4. Offline time between pulses was not recorded, which is why the current appears to be continuous and there are visible peaks in the voltage curve, when in reality there is a 30 minute (1800 seconds) offline period prior to each voltage peak. The test procedure was changed to log data continuously in later work; this and other changes are discussed in more detail in section 2.7 - clearly it is valuable to be able to analyse the recovery of the terminal voltage after a discharge pulse.

Figure 2.5 shows typical recharge curves for the LFP cells. Note that the scales are different to the previous figure.
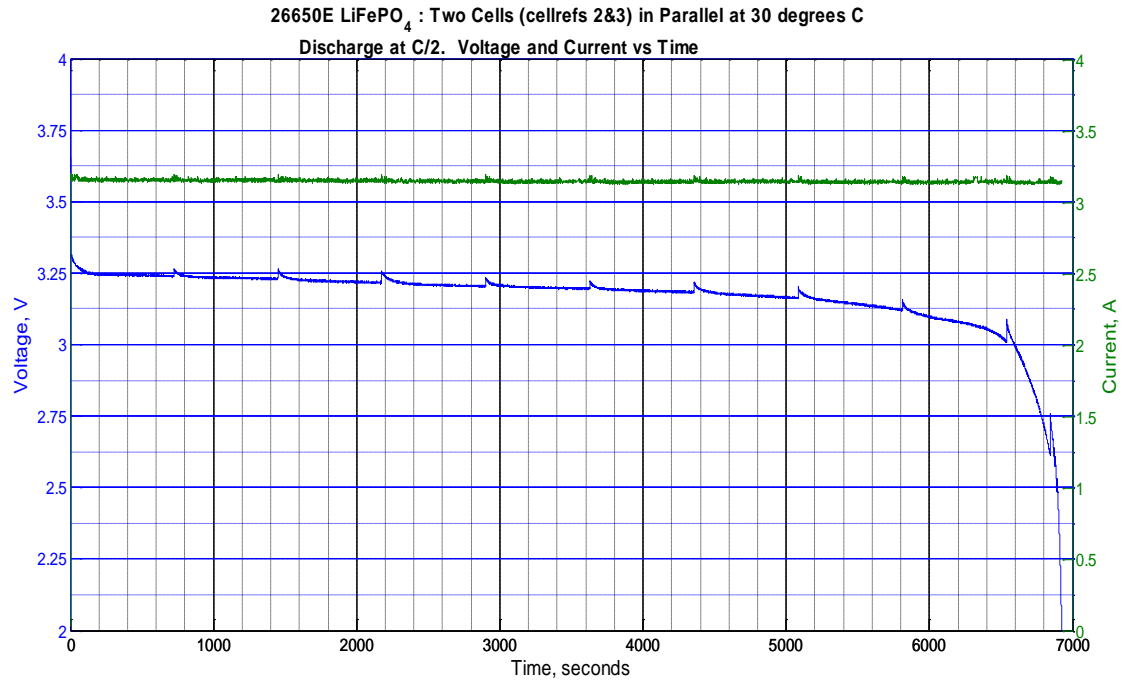
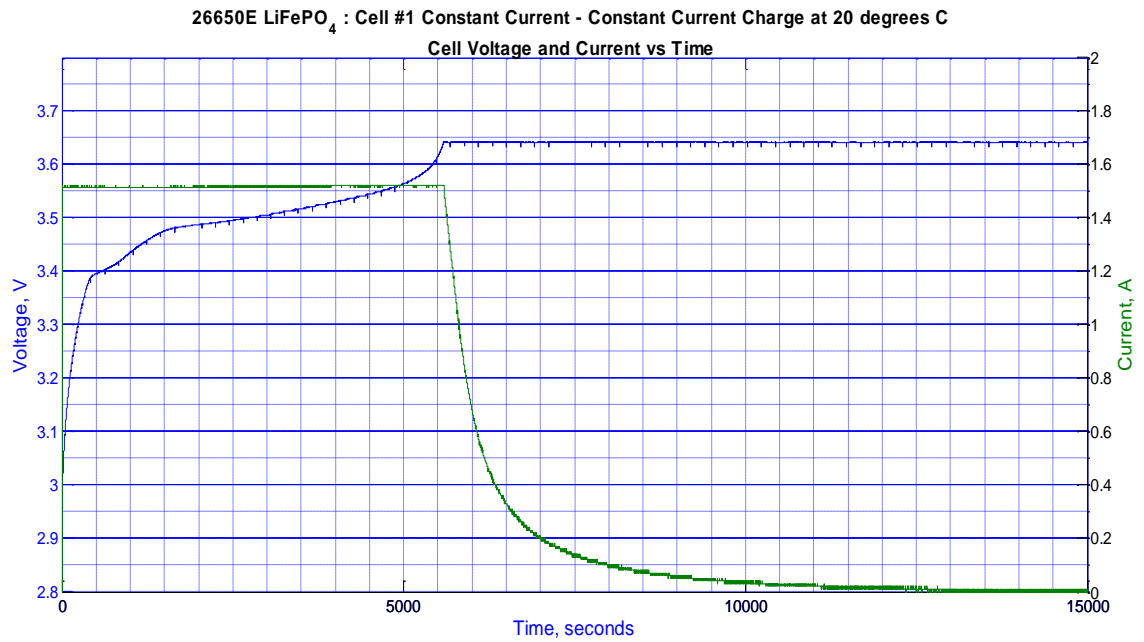**Figure 2.4 – Standard Discharge Voltage Characteristic**

Figure 2.5 - Standard Recharge Characteristic

Figure 2.6 shows the variation of measured capacity (Ah) with temperature. Cells 1, 2 and 3 show similar capacities, while cell #5 – which has been heavily cycled - has capacity reduced by approximately 15 % after 2300 cycles. Cell 4 was a new cell with zero cycles and shows the highest capacity. At low temperatures, a parallel configuration of cells allows more charge to be removed per cell (normalised capacities shown). The overall trend for all the cells, and parallel combinations, is for an increase in useable capacity as the temperature is increased (manufacturer's maximum recommended temperature during discharge is 60°C, and during charge is 45°C).
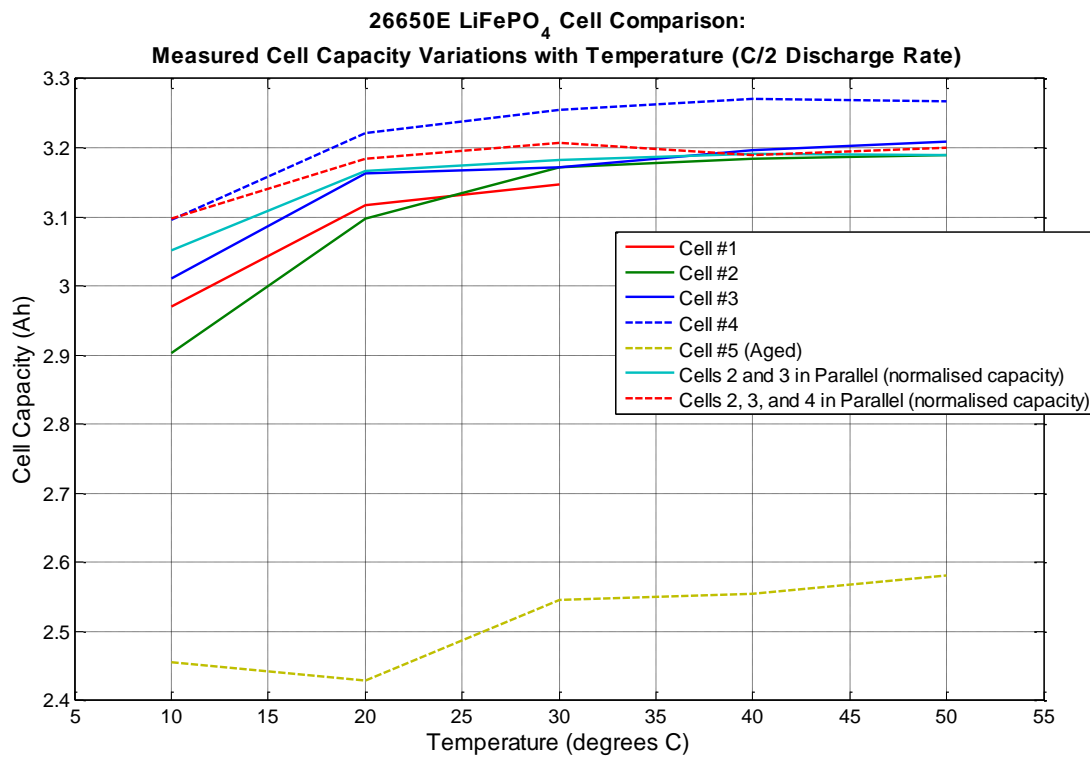
Figure 2.6 – Measured Cell Capacities

2.6.1.2   OCV, SoC and Temperature Results
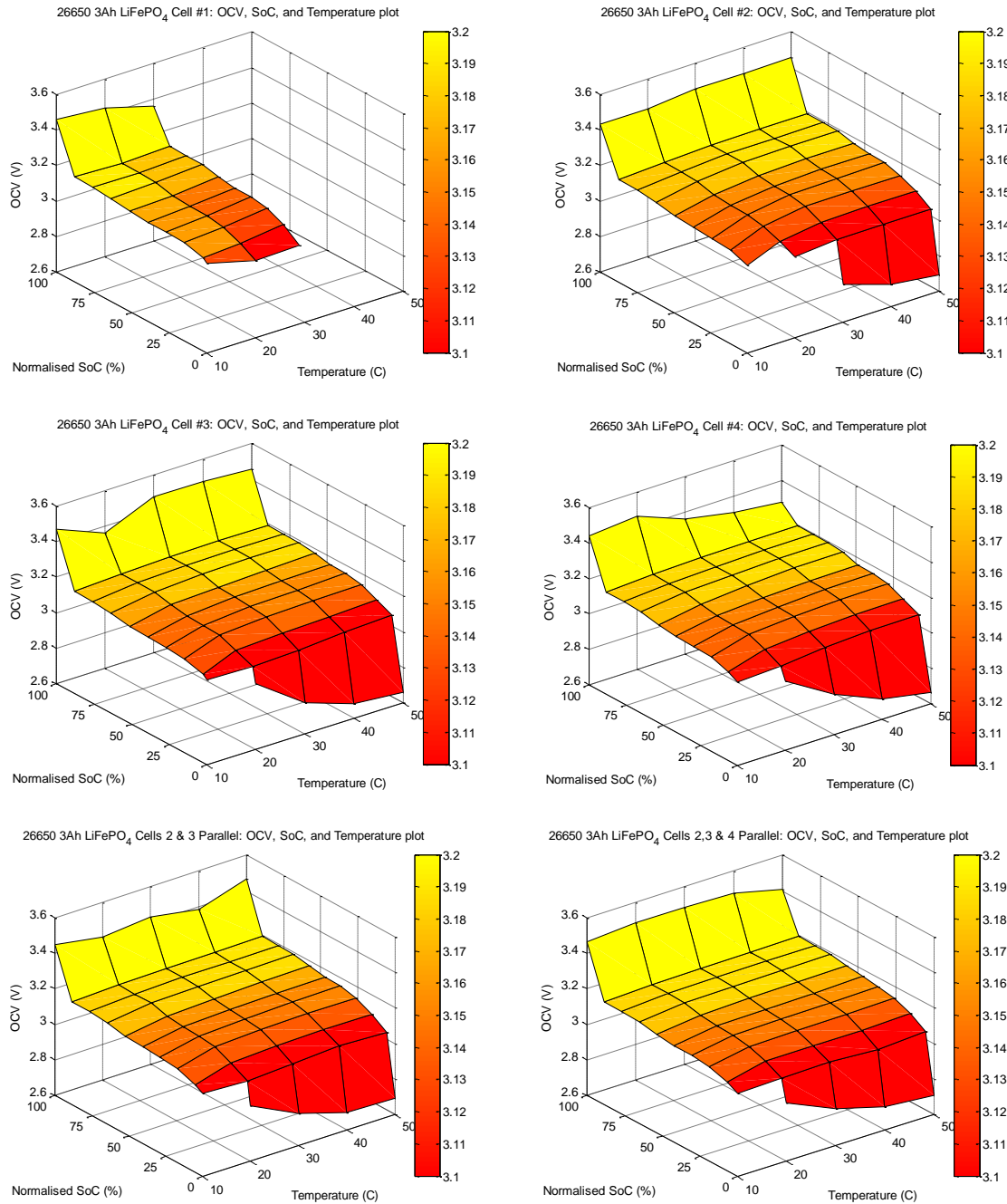

Figure 2.7 - Cell OCV, SoC and Temperature

In the plots shown in Figure 2.7 the variation of cell OCV with both temperature and SoC can be observed. While this 3D representation is helpful for observing simultaneous multi-variable trends it can be difficult to identify specific values, therefore dual-axis plots are included in the appendix in Figure A. 1 and Figure A. 2.

With reference to all plots in Figure 2.7, we see that between 90 % and 20 % SoC there is little variation in OCV, as is characteristic of LFP cells. At temperatures above 30º C there is a noticeable decrease in OCV as the cells reach a state of deep discharge, at about 5 % of normalised capacity. In the previous section (2.6.1.1) we observed that at low temperatures the cells had a reduced capacity, and here we observe that at low temperatures the OCV remains relatively higher during deep discharge. Although it was not investigated further, it may be of interest to conduct a test where a cell is discharged to 0 % at a low temperature and subsequently heated to a higher temperature before testing to see if the remaining useful charge can be recovered; this would give a clearer view of the effect temperature has on cell capacity.

2.6.1.3 *Impedance, SoC and Temperature Results*

Inspection of a typical impedance spectrum obtained from the 26650E cells revealed that the largest variation in impedance occurs at frequencies below 0.5 Hz (see Figure 2.12 on page 51). Therefore, to facilitate making a useful comparison between cells at various SoC and temperatures (see Figure 2.8, below), we use the mean impedance of the frequencies below 0.5 Hz down to the limit of resolution. Again this data can be found in dual-axis format in the appendix in Figure A. 3 and Figure A. 4.

At temperatures below 30ºC the impedance is higher, but there is also a smooth increase in impedance as the cell is discharged, indicating that it could be a good metric for estimating SoC at low temperatures. At higher temperatures the response is reasonably flat between around 90% and 5% SoC, and therefore less useful. The impedance range is also wider compared with the range of impedances observed at lower temperatures. The conclusion is that impedance-based SoC measurements will have a higher resolution at low temperatures, except at the extremes of full charge or deep discharge.

When cells are placed in a parallel configuration the range of impedances observed during a full discharge do not vary as much with temperature.
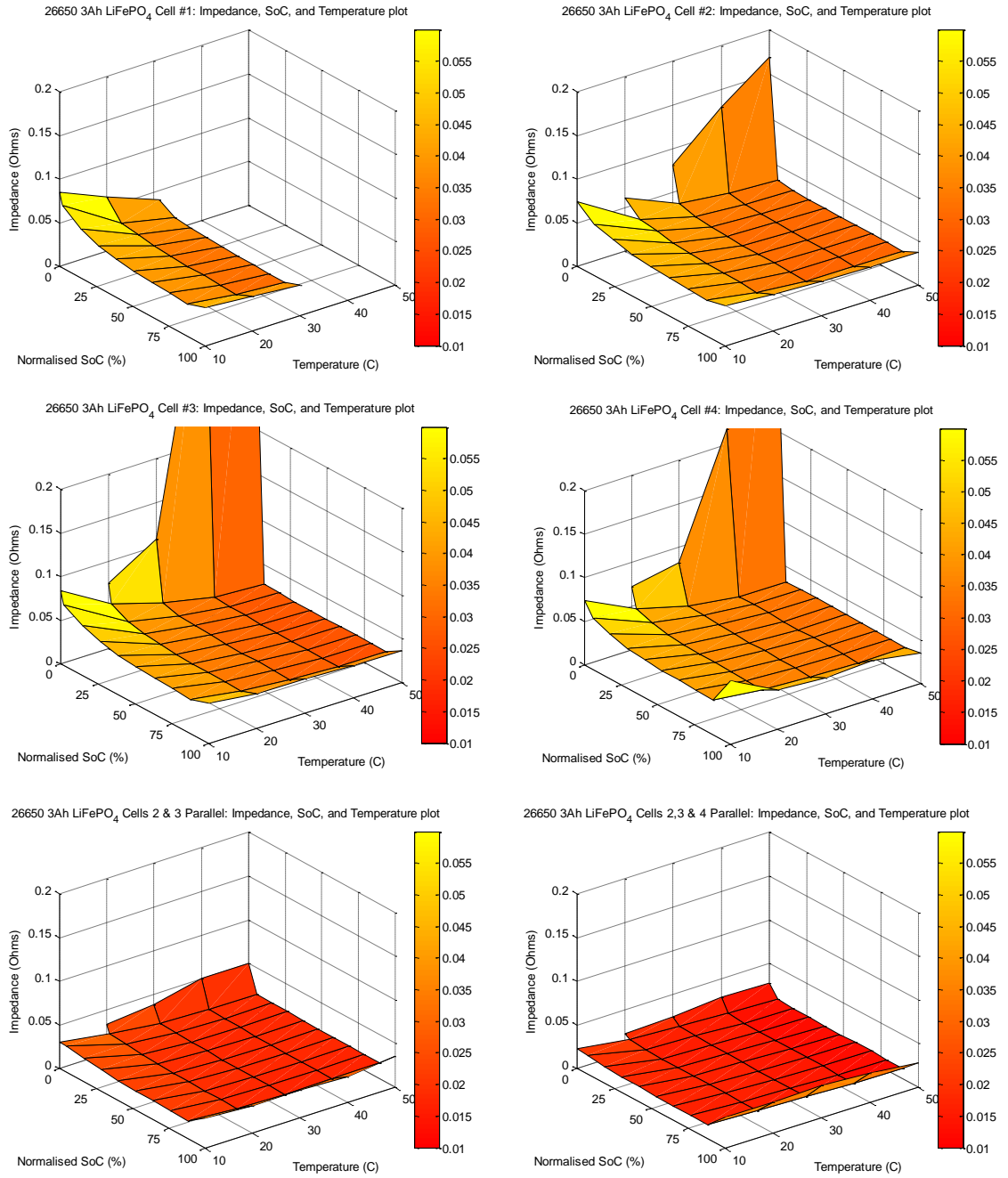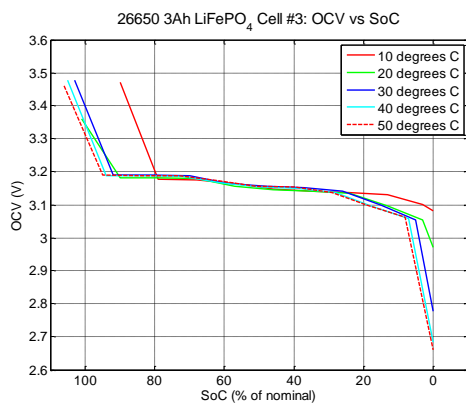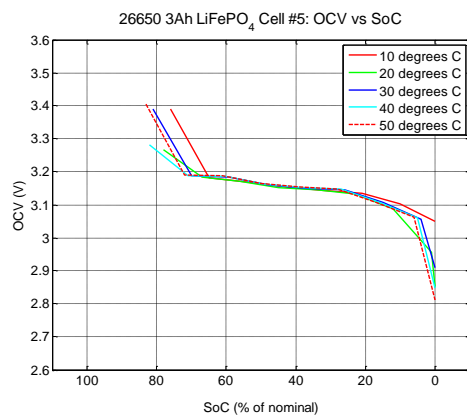
Figure 2.8 – Impedance, SoC, and Temperature

2.6.1.5 *Effects of Ageing*

Here a comparison is made between an aged cell (2,300 cycles) and a new cell, with the aim of identifying characteristic changes by which SoH can be derived. One established indicator of SoH is the capacity of a cell, since this is known to reduce over the lifetime of cycles. A comparison of Figure 2.9 and Figure 2.10 reveals that OCV does not change significantly over the life of the cell; an OCV of 3.1 V at 20°C indicates approximately 20 % charge remaining in both new and aged cells. In order to calculate normalised SoC the capacity must first be known, which requires a full discharge test. For this reason we look to the impedance data for a correlation between SoH and impedance, on the next page.

a) New Cell   b) Aged Cell

Figure 2.9 – OCV vs. Nominal SoC for New and Aged Cells
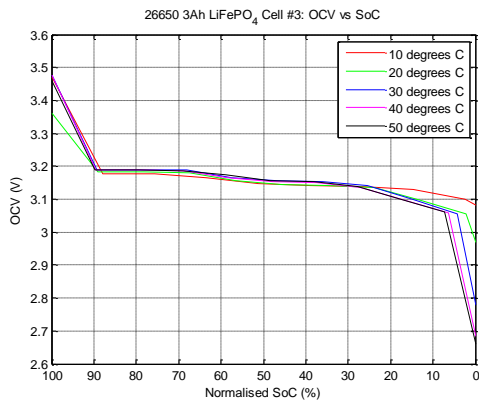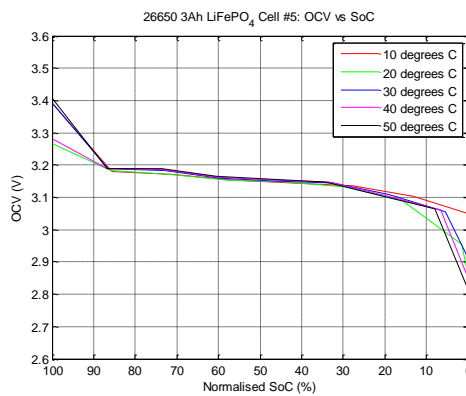
a) New Cell   b) Aged Cell

Figure 2.10 – OCV vs. Normalised SoC for New and Aged Cells
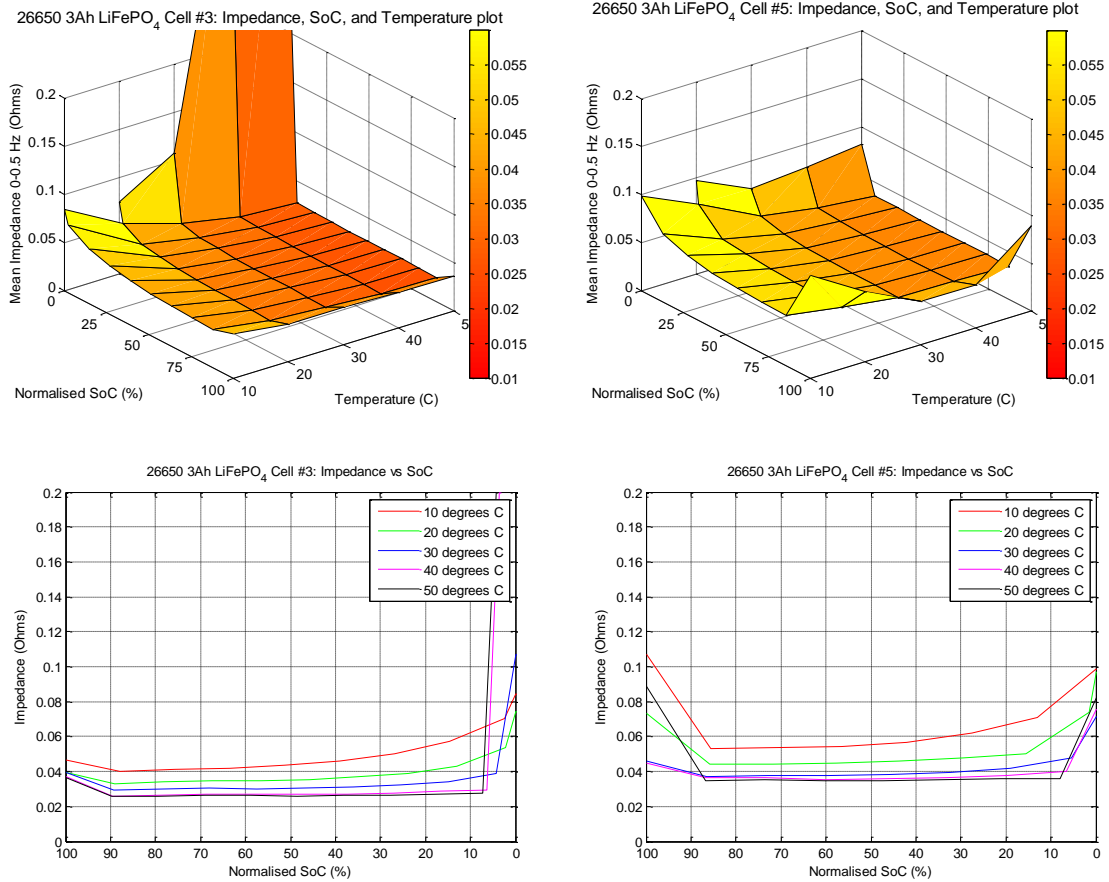
a) New Cell   **b) Aged Cell**

Figure 2.11 – Impedance (0-0.5 Hz), SoC and Temperature for New and Aged Cells

In Figure 2.11 we see that the aged cell (#5) has an overall higher impedance than the new cell, as expected, and the impedance tests on both show a similar variation of impedance with temperature. At low temperatures there may be enough of a slope in the impedance vs. SoC curves to provide a reasonable indicator of SoC, provided the SoH was pre-calculated via another method to compensate for the difference in absolute magnitude. Alternatively, it appears that it may be possible to use the impedance measured at full charge as a measure of SoH.

2.6.1.6 PRBS vs. EIS Test results

The following graphs (Figure 2.12) show the general correlation between results obtained using the swept sine method on a Solartron 1480 Electrochemical Impedance Spectroscopy (EIS) machine, and results obtained by PRBS. Rather than trying to identify individual SoC levels in each graph, the graphs are presented here to show the general correlation between results obtained on the different equipment.
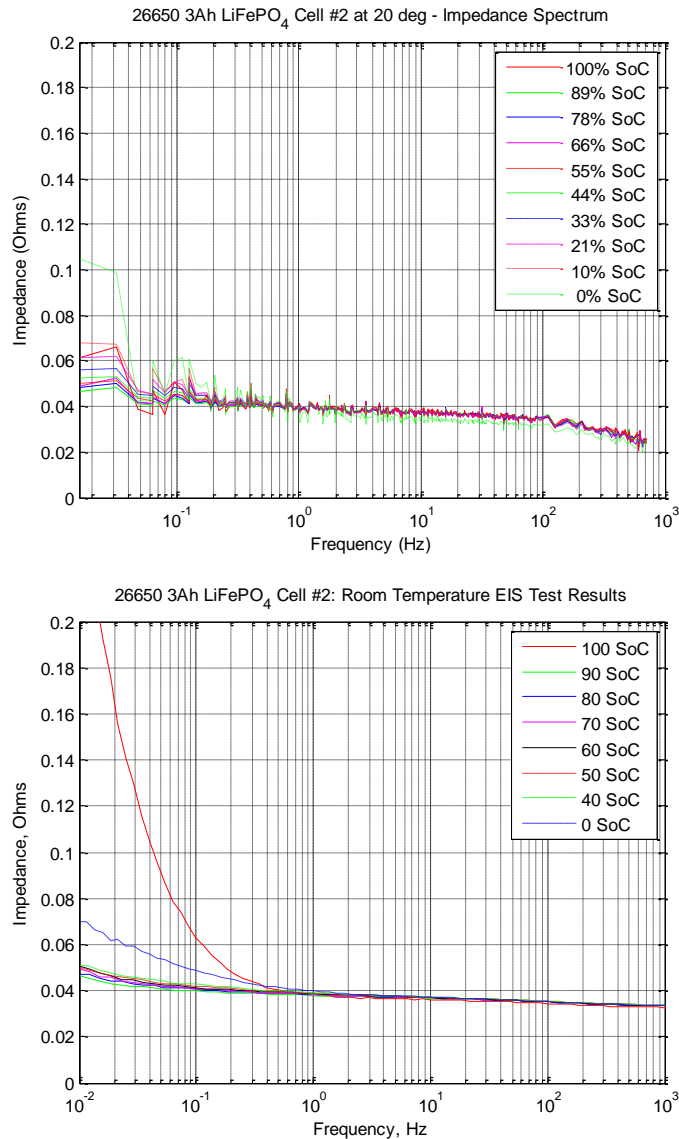
Figure 2.12 – Comparison of PRBS Impedance Results with EIS Swept Sine Results

The PRBS data is obtained almost 40 times faster – in around 200 seconds – and the

51

equipment cost is a fraction of the EIS test equipment cost. A comparison of the results show good correlation apart from the 100 % SoC test, but this can be explained by different relaxation times prior to beginning the tests; the EIS test was started immediately after a full charge, with no voltage relaxation period preceding it.

Apparent in Figure 2.12, as mentioned previously, is that at frequencies above 0.5 Hz both tests reveal little difference in impedance as the SoC changes. The PRBS results diverge from the EIS measurements at frequencies above around 100 Hz, and reasons for this are proposed in section 2.7. Otherwise, the results show good correlation.

2.6.2 *LTO Polymer (Pouch) SLPB Cells*

These high capacity (100 Ah) cells were pulse discharged (10 Ah pulses) at a rate of C/5 (20 A). Due to their size (450mm x 325mm x 7mm) they could not be placed in the temperature controlled environment, therefore they were tested at room temperature. One new cell and one aged cell were tested.

2.6.2.1 *Discharge and OCV Data*

Pulse Discharge Rate = 20 A (C/5). Voltage Recovery Time (not visible in Figure 2.13) = 1800 seconds.

New Cell	Aged (>2300 Cycles) Cell
Measured capacity at 20°C = 101.3624 Ah	Measured capacity at 20°C = 64.2108 Ah

Table 2.3 – Measured Capacity, New and Aged LTO Cells
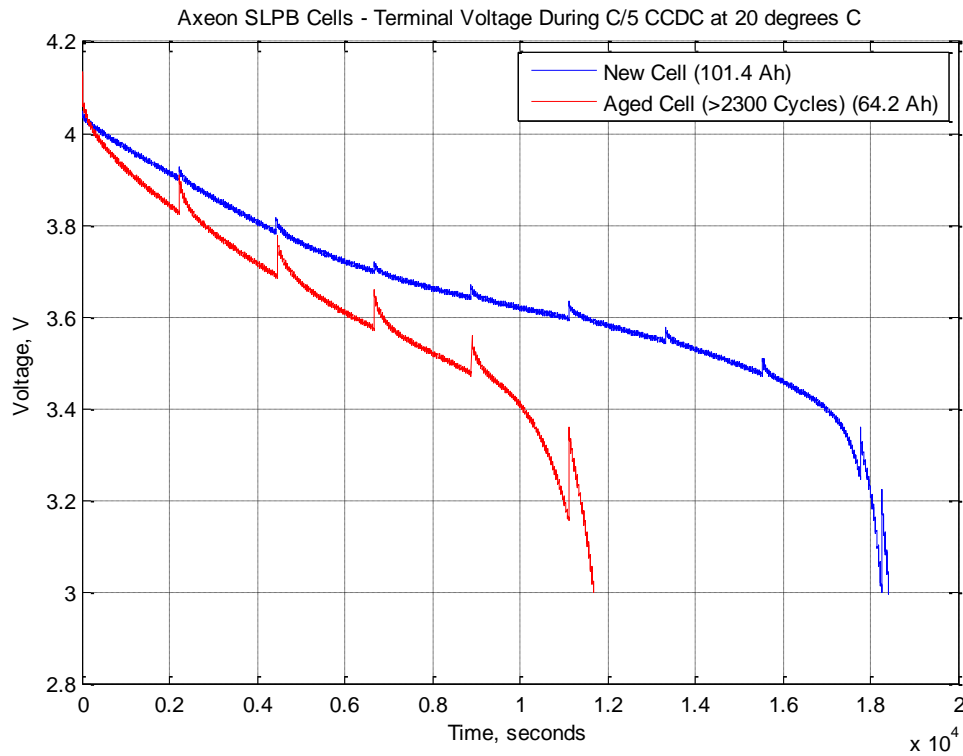
Figure 2.13 – PDC Voltage Curves: New and Aged LTO Cells

The PDC test in Figure 2.13 shows the degradation of the aged cell in terms of useful capacity; the aged cell has 63 % of the capacity of a new cell. In Figure 2.14 we see the OCV against normalised SoC – taking the reduced capacity into consideration – and we can observe two things. First, that LTO cells have a larger and more linear slope of OCV against SoC compared to LFP cells. As discussed in section 1.2.3, this means OCV can be a good metric to feed SoC estimation. Secondly we see that at SoC below 20 % no SoH compensation for ageing effects is required in order to make a good estimate in an LTO cell. Despite there being a reasonably linear relationship between OCV and SoC at higher states of charge, SoH information is required to make an accurate prediction of SoC from 100 % - 20 % SoC due to the observed increase in absolute OCV in an aged cell.
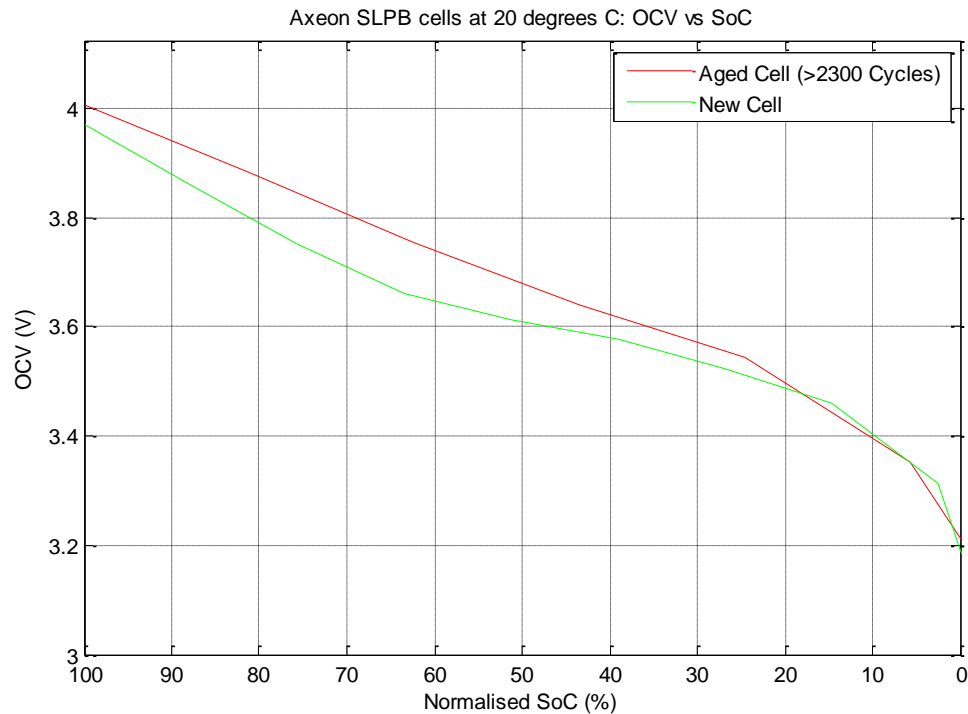
Figure 2.14 – OCV vs. Normalised SoC, New and Aged LTO Cells

2.6.2.2 <u>PRBS Results After 10 Ah Pulse Increments</u>
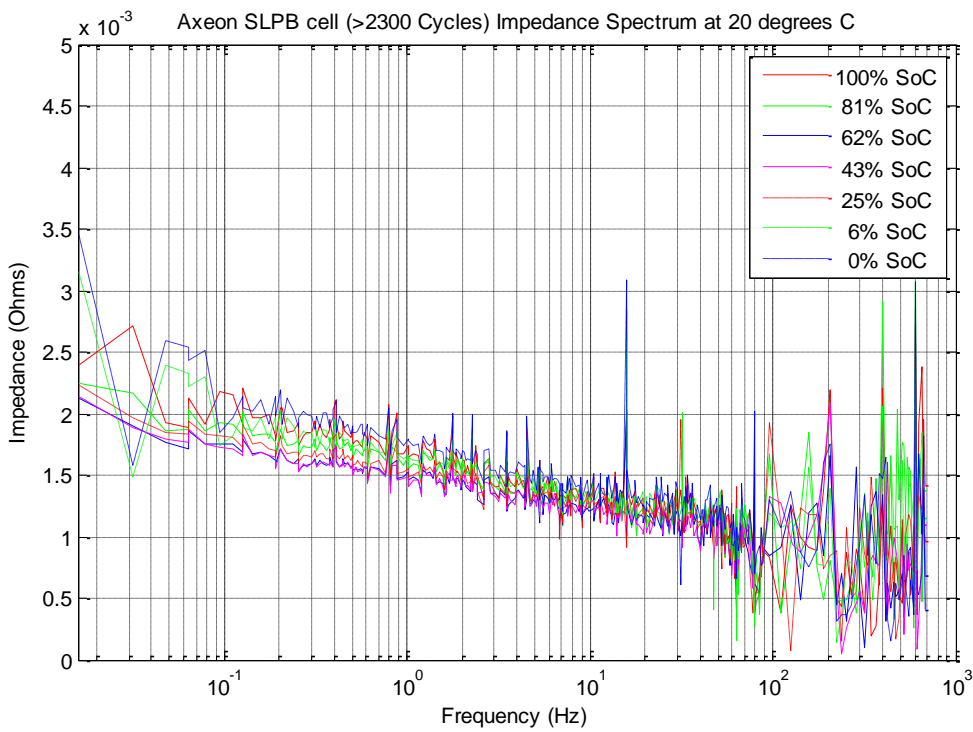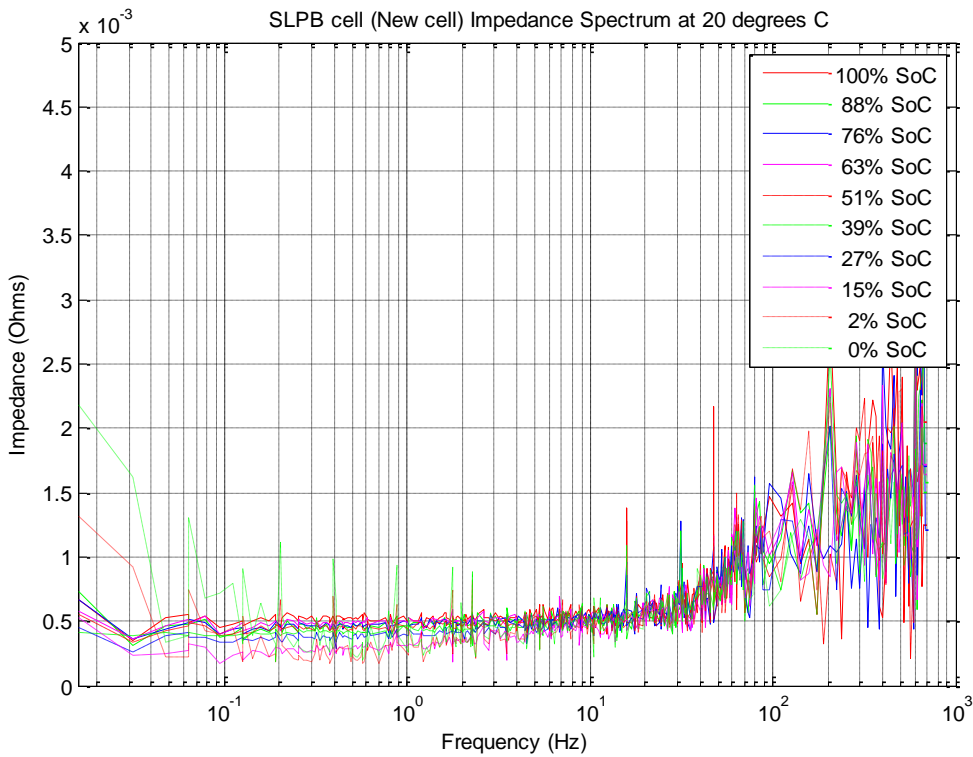
Figure 2.15 – PRBS Impedance Test Results, New and Aged LTO Cells

The PRBS Impedance test results shown in Figure 2.7 on the previous page show a marked difference between the cells in the impedance roll-off as frequency increases. In the new cell the spectrum is fairly flat between 1 mHz and around 50 Hz, whereas in the aged cell there is a marked slope, which suggests that this data could be used as a SoH indicator.

From these plots it is difficult to find a region of the spectrum that could be used to clearly distinguish between SoC levels, and furthermore it is worth bearing in mind that when measuring ≈500 µΩ levels the noise floor and sensor resolution become a significant issue.

2.6.2.3   *Problems with Resolution*

Impedance in the aged cell was measured at levels of approximately 2.2 mΩ to 0.5 mΩ, while in the new cell sub 0.5 mΩ levels were seen (see Figure 2.16).
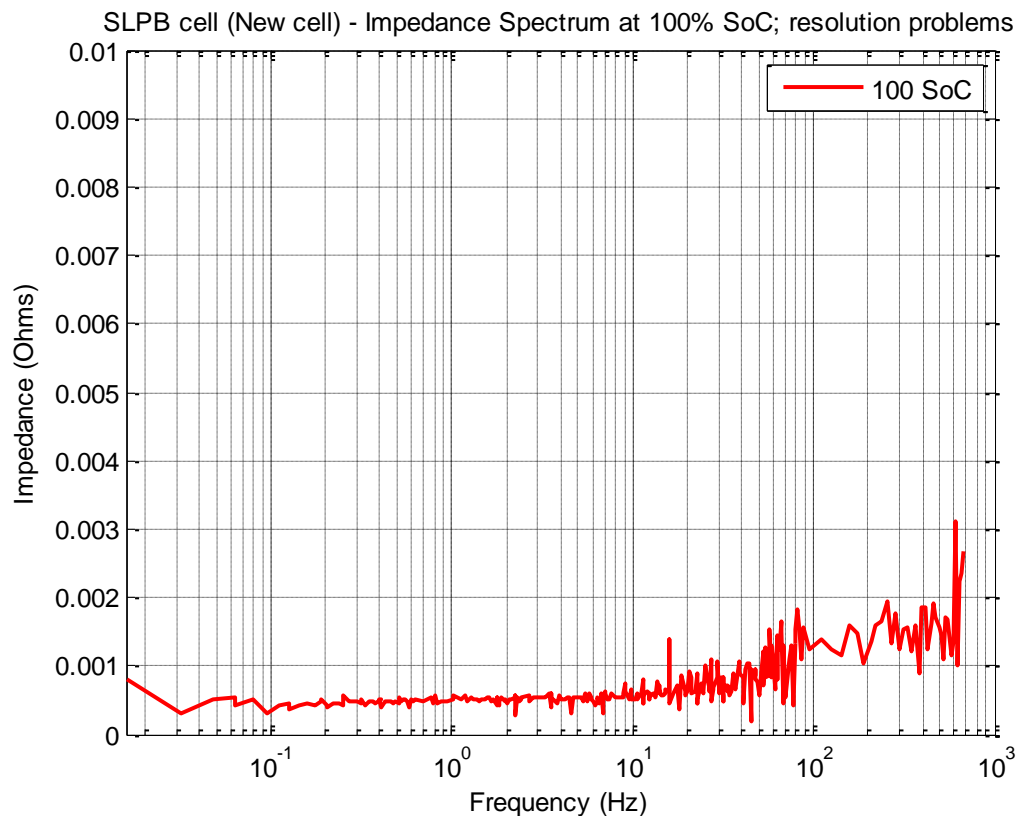
Figure 2.16 – New LTO Cell Impedance Spectrum at 100 % SoC

Inspection of the time-domain PRBS test data reveals that the voltage response of the new cell (Figure 2.17) is not detectable above the noise floor at these low current levels. The noise amplitude is around 5 mV, while the amplitude of voltage deflection we would expect to see from a 1 A amplitude current stimulus on a 0.5 mΩ cell would be a tenth of this.
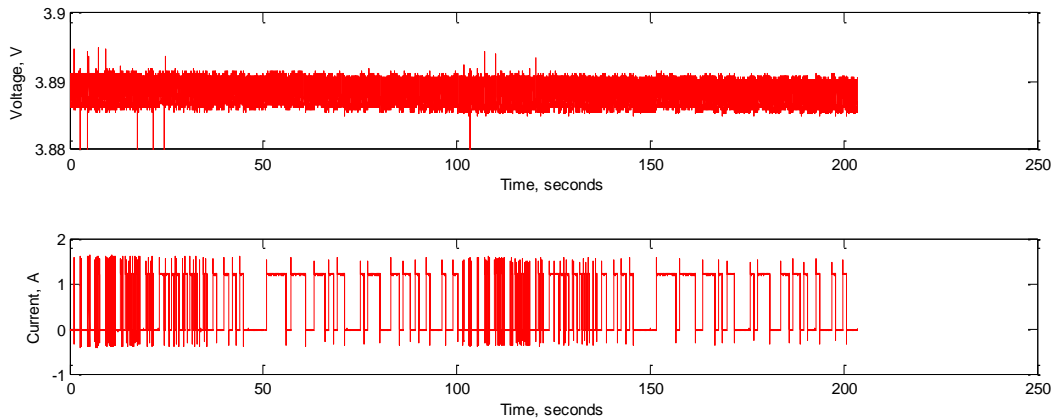
Figure 2.17 – New LTO Cell PRBS Current and Voltage Showing Poor Resolution

The aged cell - with higher impedance - has a more distinguishable voltage response (Figure 2.18) but still the response amplitude is only around 8 mV and well into the noise floor.
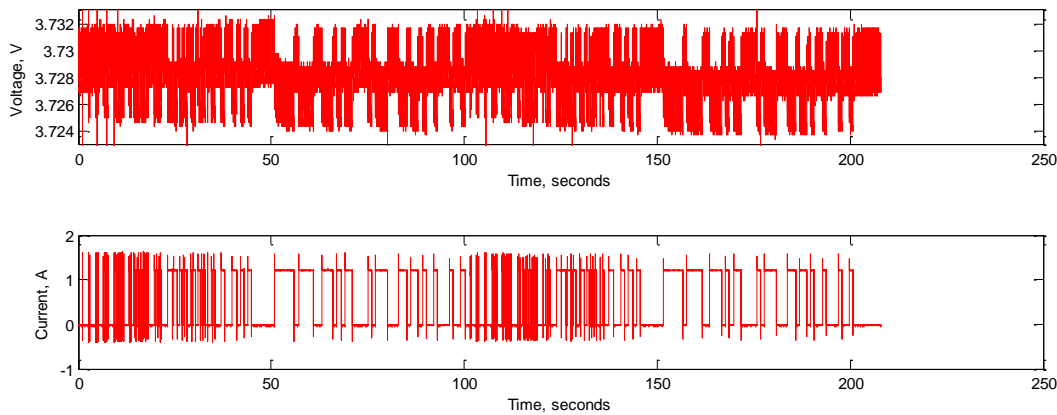
Figure 2.18 – Aged LTO Cell PRBS Current and Voltage

Clearly this test equipment is not suitable for making accurate impedance measurements on higher capacity cells, and a higher PRBS stimulus current is required.

2.7   **Preliminary Findings and Suggested Changes**

Documented here are the weaknesses found in the early system which prompted a redesign and new methods.

2.7.1   *Charge Cycling*

The biggest problem with the existing charge cycling rig was a stability issue when testing higher voltage cells and batteries. When all four output channels were operating in parallel, the system became unstable as the battery current was increased to beyond a few amps. All attempts to stop these output oscillations ultimately failed - increasing the bypass capacitance decoupling the power supply, decoupling of the control op-amps, shortening wires (although more could have been done here – by this time work was underway designing the new system). For this reason maximum cell power characteristics were not mapped, although low voltage (3.7 V) single cells were successfully cycled at rates of 20 A (C/5) using a single output channel.

Problems with stability while charging cells meant that this step was often done directly using a current limited power supply. This was not ideal since it would have been useful to compare charging capacity of the cell against discharging capacity, but a complete set of charging data was not obtained.

Another weakness of the initial setup was the failure to continuously log the cell terminal voltage as it settled during the voltage relaxation step. This data would allow for a good estimation of OCV despite a short rest time, and should be logged in future.

2.7.2   *PRBS Impedance Testing*

The PRBS generation clock and data acquisition clock were not synchronised, and the LabJack inter-channel delay when streaming four channels at 5 kS/s was later discovered to be a maximum of 120 microseconds, which is 12 % of the PRBS clock period at 1 kHz (and 60 % of the acquisition period at 5 kS/s). Failure to identify precise whole-length sequences prior to performing a spectral analysis of PRBS streams results in significant spectral noise, therefore this margin of error is unacceptable.

Further, the PRBS generation clock signal itself was not hardware timed. The binary sequence was read in a software 'for' loop, reading each bit from a variable stored in memory, and an 'if… else' statement decided whether to make the digital output pin high or low. An attempt was made to mitigate the errors introduced as a result of the use of software timing by taking oscilloscope measurements of single PRBS bit periods to confirm the actual clock rate for correction purposes. However, another source of timing error may be introduced when performing 'if… else' statements within a software loop, due to the two outcomes (if/else) having different execution time after the code is compiled. Ultimately these bring uncertainties into the work which could be avoided with the use of hardware timing and synchronised generation and acquisition clocks.

14-bit resolution was found not to be sufficient to accurately measure the response voltage when testing large capacity cells (50 Ah and above) at low (1 A) PRBS currents. One solution is to increase both the stimulation current and the measuring resolution (use 16-bits resolution, and increase current to +/- 5 A). It is also prudent to make bipolar stimulus a requirement, so that the overall state of charge is not affected during the impedance test. System Identification requires that the system state does not change for the duration of the test.

Still considering resolution, we must ask ourselves about the final application. If PRBS impedance measurement is to be embedded in say an EV BMS, then very low impedance levels such as those seen in the LTO cells require sensitive measurement instruments. These are not commonly available in very high cell-count battery packs, where 5 mV resolution is considered to be good [52].

Finally, the PRBS frequencies chosen were based on values inherited from previous work in the group. It was later confirmed that those frequencies were in fact chosen to suit a particular microcontroller's counter divisions. With this information, a more logical choice in a new system would be to choose roughly logarithmic frequency intervals, such as 1, 2, 5, 10 and so on, as these produce an even spread of data points on a logarithmic frequency plot.

These findings form the basis for the development of the system described in the next chapter.

Chapter 3: Charge Cycler/Impedance Analyser Specification and Design

3.1   Objectives

As discussed in the previous section, weaknesses in the early design prompted ideas for improvement which could be met with a new design. Previously built hardware was limited in three ways which were to be addressed:

1. Unipolar current. During a system identification test it is important that the system being measured does not change state over the duration of the test; that is, its final state (e.g. SOC of a battery) must be the same as its initial state. Some low frequency aliasing effects in impedance spectra gathered from the unipolar PRBS rig can be explained by the fact that during the course of the system identification tests the state of the system was in fact changing at a very low rate. This unwanted effect can be avoided by using bipolar stimulus that has no net effect on charge over the duration of the test.
2. Amplitude. The previous hardware was limited to 1.5 A pulses which is not a high enough current stimulus to cause sufficient voltage deflection in larger capacity (> 20 Ah) cells. Upgrading from 14 to 16-bit data acquisition went some way to improving measurements, but the capability to drive larger currents would provide better results (improved SNR).
3. Timing. The previous hardware relied on software timing to clock the PRBS stream, and asynchronous hardware timed data-acquisition. The new design uses hardware timing for both PRBS generation and acquisition and synchronises data acquisition with the stimulus pulse edges.

3.2   Hardware Design and Construction

3.2.1   Target Specification

A transconductance amplifier was required that could perform charge cycling and PRBS stimulus/response measurements on a variety of battery cells and single port networks.

Table 3.1 lists the proposed minimum requirements.

DUT Voltage Range	1.5 V – 6 V
DUT Current Range	± 5 A
Acquisition Sample Rate	10 kHz desirable, 5kHz acceptable
NI USB-DAQ 6211	Synchronised simultaneous V and I measurement ADCs
	Synchronised sample and PRBS clock
System Tests	Prove on an RC network, charge and discharge at rated current, and obtain impedance spectrum. Validate results against those from a spectrum analyser. Then cycle a battery and do a PRBS impedance analysis.

Table 3.1 – Minimum Requirements

3.2.2 Design Steps

3.2.2.1 Overview

In order to provide test equipment of high reliability and robustness, some aspects of the design involved increasing the target specification to allow a comfortable overhead during longer test cycles. Reliability and flexibility of the equipment was an important factor, therefore the design was based on a continuous current rating of 200% (+/- 10 A) with 125% of rated Device Under Test (DUT) Voltage (7.4 V max). Furthermore the DUT voltage range was extended down to 0 V in order that passive networks could be tested, which would aid calibration of the rig.

The overall topology (full schematic in the appendix) is based around a BJT push-pull output stage powered from a bipolar DC link. A link voltage of +/- 12 V was chosen for convenience. There is a Voltage Amplification Stage (VAS) which is loaded by a small current source and a pre-driver bias circuit to maintain class B amplification, thus minimising crossover distortion with minimal quiescent current. Control of the output current is achieved using a reference voltage to drive the VAS via a differential amplifier.

3.2.2.2   *Output Stage Devices*

Transistors available in the local Electronic Stores were chosen for the design so that in case of failure minimum downtime would be suffered. Figure 3.1 shows the Safe Operating Area (SOA) of the TIP3055 and the complementary pnp type TIP2955. The design criteria of discharging a 7.4 V battery at 10 A into a -12 V link places the required operating area on a vertical line denoted by $V_{ce} = 19.4$ V, which corresponds to a maximum current of roughly 4 A, capped by the thermal limit of the low-side devices. A minimum of three devices in parallel are required therefore, to meet the 10 A current requirement, and four were chosen in the design to provide suitable de-rating.
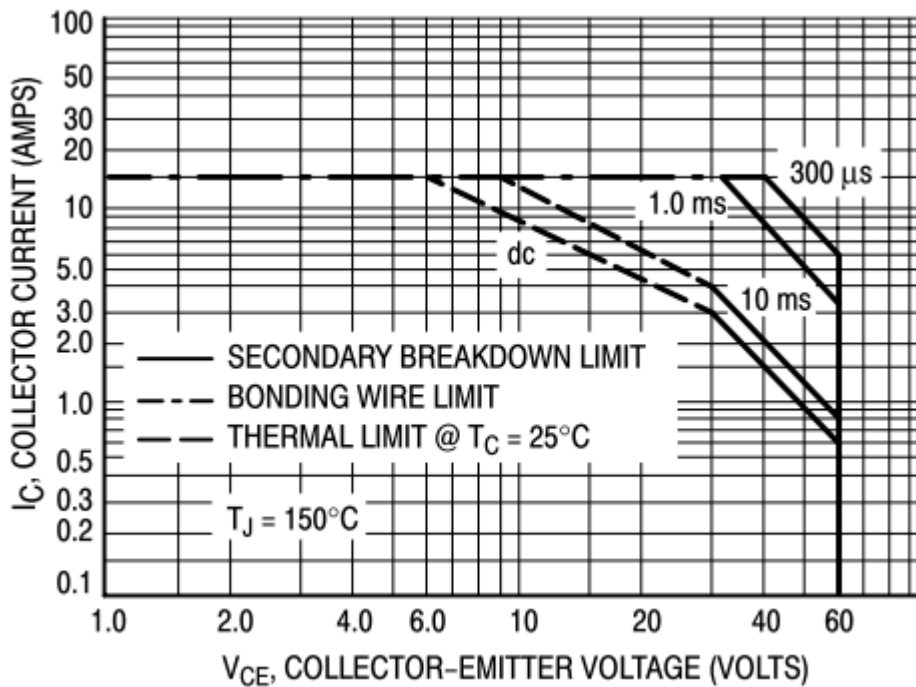
Figure 3.1 – TIP3055/2955 BJT Safe Operating Area, single device

Small emitter degeneration resistors are fitted to each output device so that current is shared equally between devices. Due to the negative temperature coefficient of BJTs, if one device heats more than another this leads to an increase in current through that device; the 0.1 Ω emitter degeneration resistor will compensate for this and prevent thermal runaway by reducing the V_{CE} across the device and thus a dynamic equilibrium is maintained between all parallel devices.

3.2.2.3   *Heatsink Requirements*

The heatsink requirements were calculated using the same worst-case calculations as for the output devices, see Figure 3.2.

Worst Case Low-Side Dissipation (one device of four is shown):

10 A continuous discharge of a 7.4 V DUT (2.5 A per low-side device)

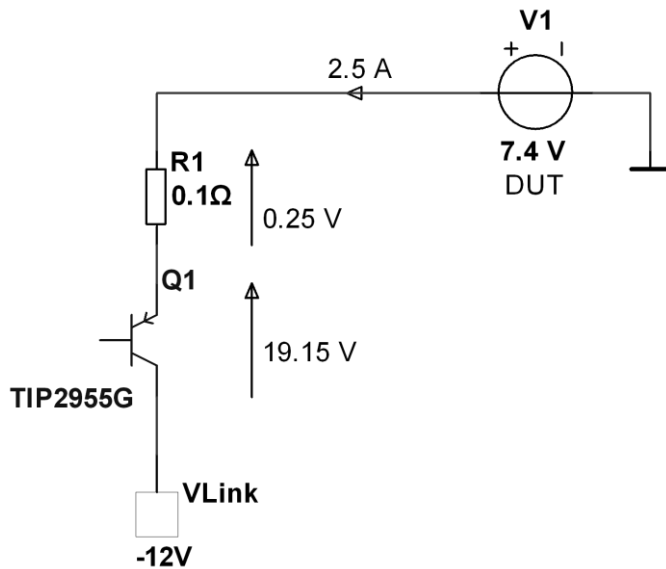Power dissipation = 50 W per device (200 W total).

Figure 3.2 – Output Stage Maximum Load

The design assumption is that each output device will be expected to dissipate a maximum of 50 W continuously. With reference to Figure 3.3 the thermal resistance between junction and case of these devices is 1.4° C/W, while the thermal pads used add a further 0.425° C/W. This means that the junction of each device will rise 92° C above the surface temperature of the heatsink under maximum load conditions.

The absolute maximum allowable junction temperature (T_{junc}) is 150° C. A good de-rating factor might be 0.8, making the maximum allowable T_{junc} = 120° C. However given that T_{junc} will always be 92° C above the heatsink surface temperature (T_{surf}) this would require that T_{surf} not be allowed to exceed 30° C; this would require a heatsink with heatsink-to-ambient thermal resistance of 0.019° C/W. This sort of heatsink requirement would need an exotic

cooling mechanism and the cost would be substantial, but since these calculations were based on an uprated design criteria then the decision was made to relax the thermal de-rating to 5%, with a maximum $T_{junc} = 142.5°$ C when the system is running at 200 W in 25° C ambient temperature. Thus the maximum permissible heatsink surface temperature T_{surf} is 50° C, and the heatsink to ambient thermal resistance requirement to maintain this is $25/200 = 0.125°$ C/W. A forced convection, 0.12° C/W heatsink was sourced from Fischer Elektronik (LA 7/100, 24V Dual Fans).

Heatsink Requirements for Worst Case Scenario

The temperature at the junction of each device will rise 92° C above the heatsink surface temperature.
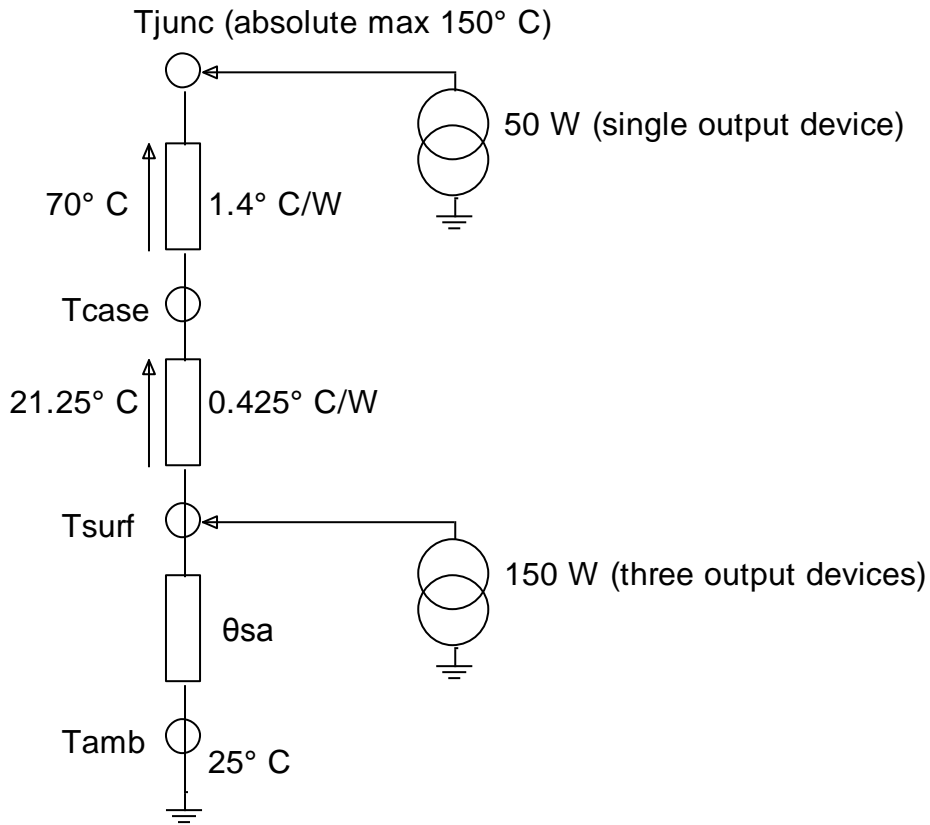

Figure 3.3 – Heatsink Maximum Power Requirements
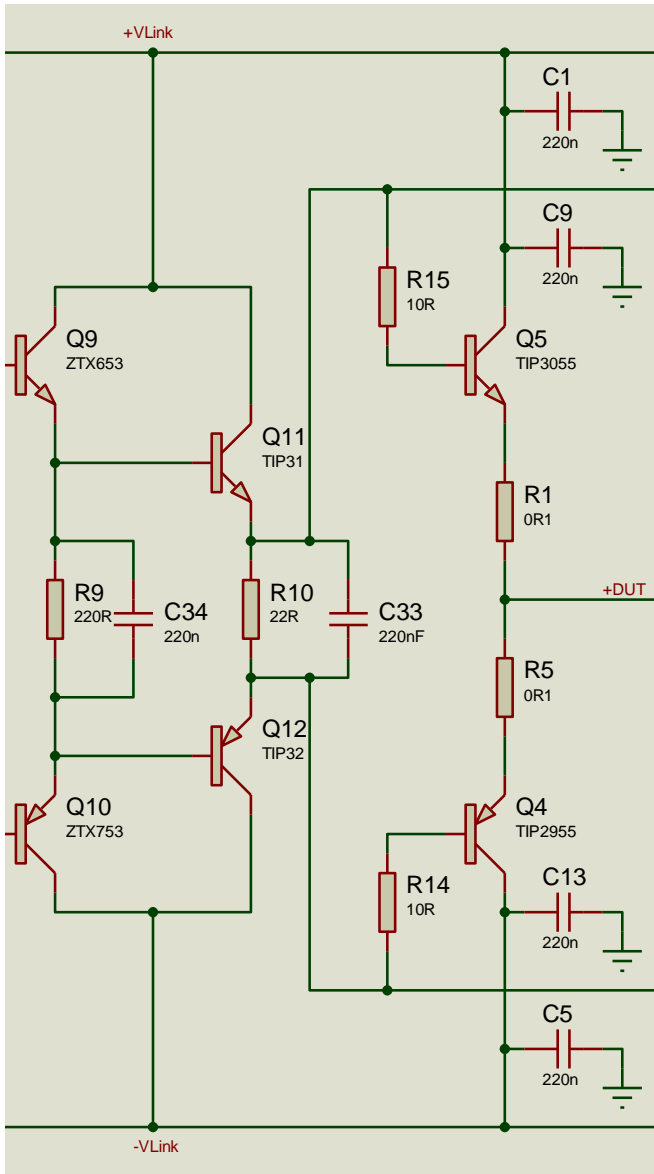
3.2.2.4   *Output Pre-Drivers*

Figure 3.4 – Output Pre-Drivers and One Output Pair

The TIP2955/3055 output devices Q_4 and Q_5 have a minimum h_{FE} of 20 when collector current, $I_C = 4$ A, and $V_{CE} = 4$ V. For the same V_{CE} but with $I_C = 10$ A this reduces to $h_{FE} = 5$. As neither of these conditions exactly match the rig design criteria, the lower value of the two is used here; under maximum load conditions each device will carry 2.5 A, therefore a maximum base current of 500 mA for each output device – total 2 A - should be allowed for. Again sourcing parts from the local stores, TIP31 and TIP32 BJTs have been used in the design and each forms a Darlington pair with a ztx653 and ztx753 respectively (Q_9 and Q_{11}, Q_{10} and Q_{12}), thus providing suitable current gain in the pre-driver stage so as not to overload the VAS under maximum load conditions. Resistors R_9 and R_{10} limit current in case of shoot-through occurring, while C_{33} and C_{33} speed up transitions.

3.2.2.5   *Voltage Amplifier Stage (VAS)*

The VAS comprises a current source (Q_{14}, R_{21}, D_4, D_5 and R_{20}) which is biased into 6mA constant conduction, Figure 3.5. This forms an active load for the VAS transistor Q_{15},

maximising transistor gain while simultaneously providing increased current sourcing for the pre-driver stage.
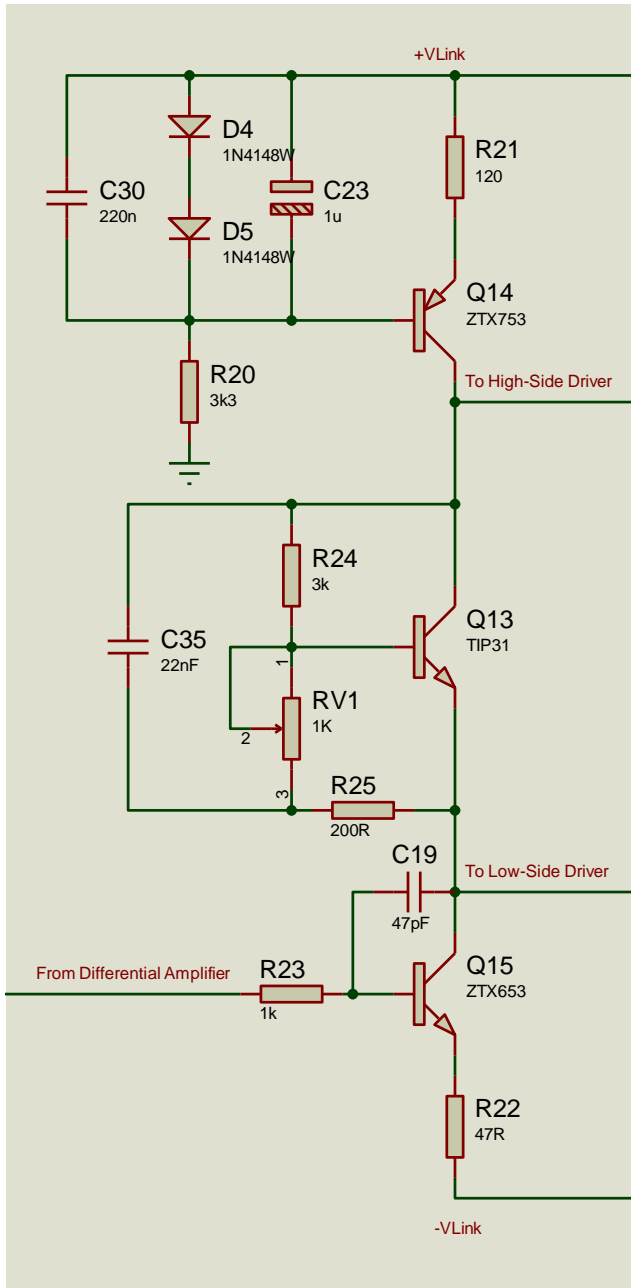

Figure 3.5 – VAS with Current Source Load and Pre-Driver Bias

Q13 and its associated bias resistor network maintains a bias voltage between the pre-drivers in a dynamic equilibrium which in turn maintains a low quiescent current in the output devices. This reduces the effect of crossover distortion when switching from high-side conduction to low-side, or vice versa. RV_1 provides a means of calibrating this quiescent current after construction. The bias voltage required is in the region of 4.2 V, as the output transistors (which require a bias of ≈0.7 V each to be on the verge of conduction) are supplied by Darlington pair pre-drivers each requiring ≈1.4 V of biasing. Component values were chosen based on **Equation 3** while maintaining a minimum base current to Q13. A common failure mode for variable resistors is to fail open-circuit, therefore its position was chosen such that this mode of failure would cause a *decrease* in bias voltage.

$$V_{bias} = V_{CE(Q13)} . \frac{(R_{24} + [R_{25} + RV_1])}{[R_{25} + RV_1]}$$

Equation 3

As discussed previously, BJTs have a negative temperature coefficient, therefore the bias transistor Q_{13} is mounted close to the output BJTs on the heatsink, between the high-side and low-side devices. This ensures good thermal-tracking and therefore temperature compensation for the non-linear change in bias requirements as temperature increases.

Finally the capacitor C_{19} is chosen to create a dominant pole around the base-collector junction of Q_{15}.

3.2.2.6   *Differential Amplifier and Global Feedback*

Figure 3.6 shows the input and feedback topology of the amplifier. Omitted from the figure is the current sense resistor which is located between the DUT and ground. This is actually comprised of two 1% precision 1 Ω resistors in TO-247 packages. These have less than 12 nH inductance and 3 pF capacitance each, and a typical temperature coefficient of 60 ppm/°C. For a worst case operating condition of 10 A continuous DC, this represents a maximum error of 0.25%. The voltage generated across the sense resistance is fed back to the IFB input in Figure 3.6.
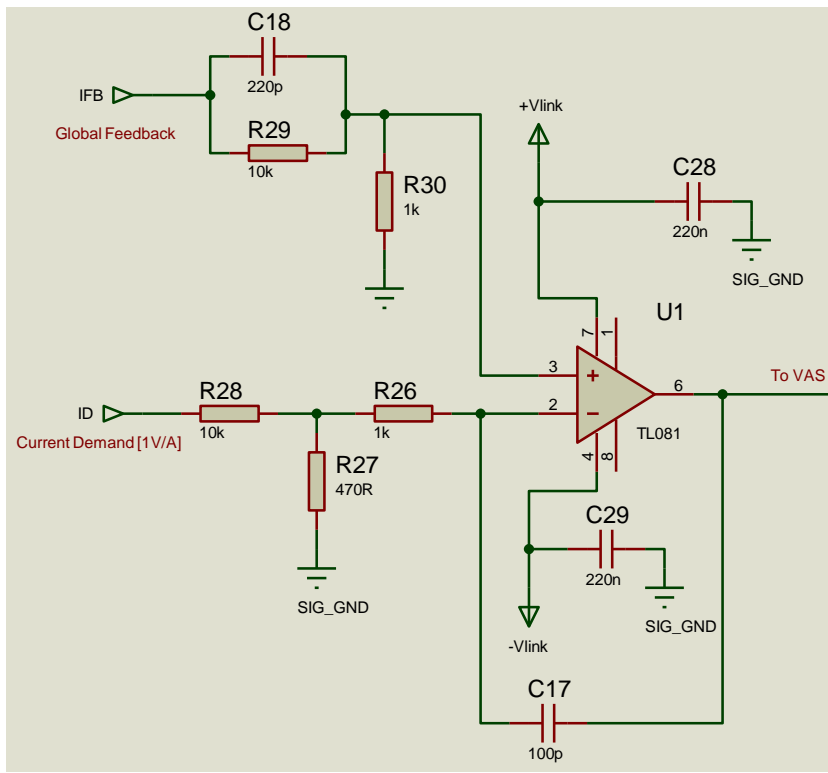
Figure 3.6 - Differential Amplifier and Global Feedback

As the VAS adds an inversion to the architecture, the negative feedback connection is made to the non-inverting input of the op-amp U1. The input resistor network R_{27} and R_{28} along with the feedback divider R_{29} and R_{30} scale the current demand to the current sense voltage developed over the 0.5 Ω sense resistor such that ± 1 V input will produce ± 1 A current in the DUT. Capacitors C_{17} and C_{18} provide a dominant pole and pole-splitting respectively. Their values were chosen empirically using a SPICE simulation, and then tuned again empirically in hardware. The open-loop simulation response is shown in Figure 3.7 and it can be seen that the dominant-pole causes roll-off to begin at 0.5 Hz, with the second coming into effect around 1 kHz. The effect of the pole-splitting is to maintain a minimum phase margin of 25° across the upper bandwidth of the amplifier.
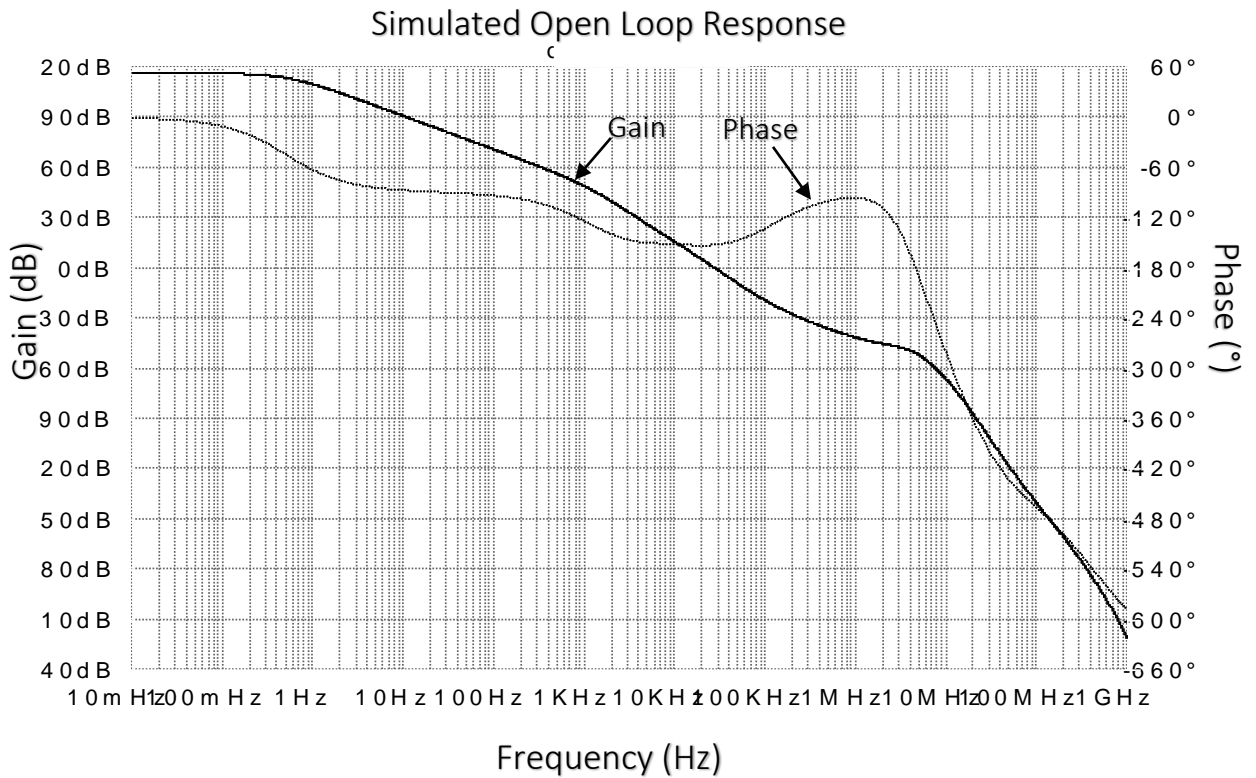

Figure 3.7 – Simulated Open Loop Response

3.3 **Theoretical Limits**

The DC Link supplies all circuitry apart from the input differential amplifier which has a separate +/-18 V supply. This is necessary due to the voltage drop of 2.1 V between the output device emitters and the base of the Darlington-pair pre-drivers; the input op-amp must be able to swing approximately 2.1 V below −Vlink in order to be able to switch off the output devices. This limits −Vlink to −15 V. The rig is designed around +/-12 V as the link voltages, but it should be possible to run with an uneven link supply if required, e.g. +30V/-15V.

The output device SOA is calculated using the data from Figure 3.1, shown in blue dashes in Figure 3.8 after scaling appropriately for four parallel devices. The power limit, shown in smaller green dashes, is calculated from the heatsink capacity. Thus using a +/- 12 V link to discharge a 7.4 V battery will cause almost 20 V to be dropped across the low-side, corresponding to a 10 A maximum continuous current rating. For a lower voltage battery such as a 4.2 V Li-ion, the maximum rating is closer to 15 A.

Impedance Test Rig Safe Operating Area
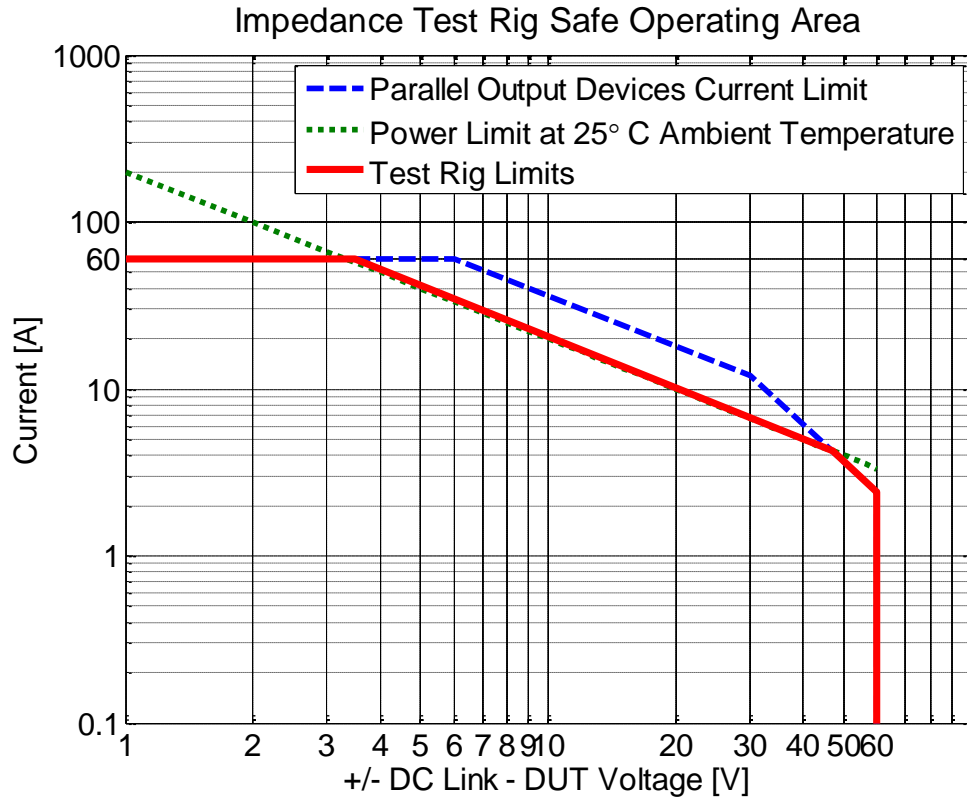
Figure 3.8 – Test Rig Safe Operating Area

The test rig is set-up to run at a maximum of +/-8 A. This was for convenience of having a 1 A/V transfer function, thus it is limited by the +/-10 V output swing of the DAQ control device, of which some of this range is required for offset nulling. Adjusting for higher currents is a matter of adjusting the value of R_{27}, and the scaling value in software.

3.4 **Control Software**

3.4.1 User Interface and Test Options

The hardware is controlled using a bespoke National Instruments LabVIEW Virtual Instrument (VI) running on a desktop PC, which provides readily reconfigurable functionality.
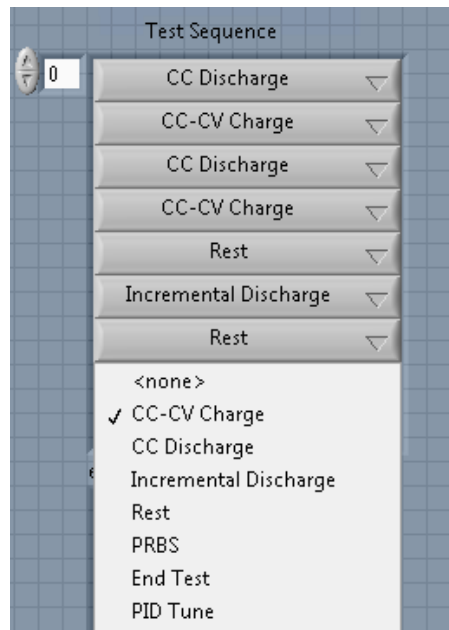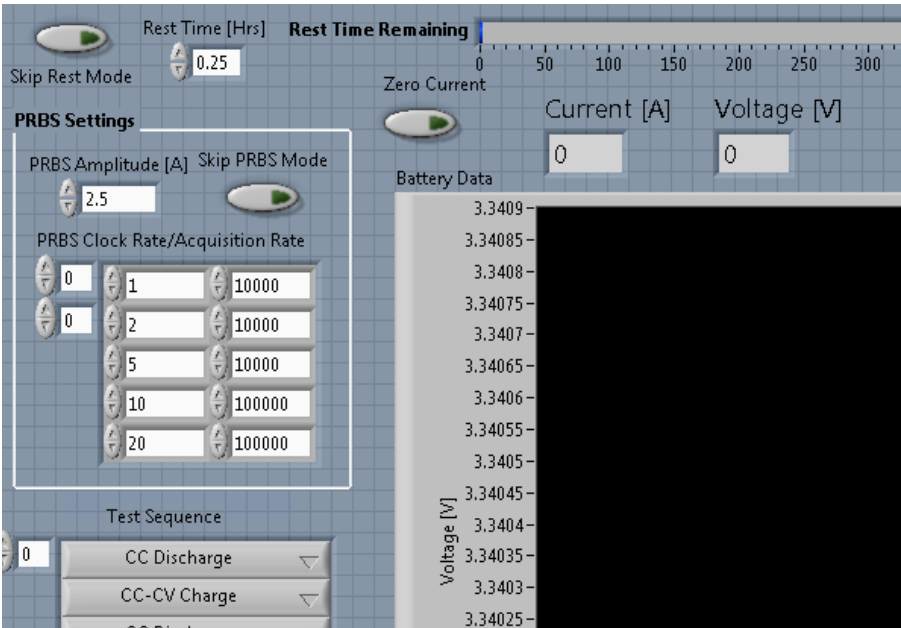
Figure 3.9 – Virtual Instrument Controls Showing a Typical Test Sequence and Available Test Options

Figure 3.9 shows how a typical test sequence is scheduled. In the case illustrated, the DUT (battery) will be cycled twice, followed by a rest, then an incremental (pulsed) discharge. Incremental Discharge actually comprises three stages; Constant Current (CC) Discharge, Rest, and PRBS are executed sequentially in this step, after which a check is made to see if the 'end test' final voltage limit has been reached, which would indicate 0 % SoC. If it has not, this step will be repeated until the low voltage cutoff is reached, after which the next step in the test sequence will be executed.

CC-CV Charge	Four settings control this mode, as seen in Figure 3.10. 1. Set Voltage – the target 'fully charged' voltage 2. Max Current – this sets the current level for the constant current mode of the charge process 3. Cutoff Current – charge current decays as charging enters constant voltage mode. This setting dictates what current level should indicate the end of the charge process 4. PID values – The load current is controlled using a software PID controller to ensure a smooth transition from Constant Current to Constant Voltage mode and to prevent overshoot or instability. (See PID Tune for setup details)
CC Discharge	Two settings are relevant to this mode, also shown in Figure 3.10. 1. Load Current - sets discharge current level. This is negative for discharge, although this step can be used to set a positive constant (charge) current, albeit without upper cutoff control 2. End-Test Voltage – sets the low-voltage cutoff threshold which signals the end of this step **Figure 3.10 – Charge and Discharge Settings**

Incremental Discharge	This mode comprises CC Discharge, Rest, and PRBS. In addition to the settings described individually for each of those modes, there is one additional setting (see Figure 3.10). 1. Charge to Integrate – in incremental discharge mode, CC discharge is stopped when a pre-defined amount of charge has been removed, or when the low voltage cut-off is reached. In the former case the step will repeat after a rest period and PRBS test, while if the low voltage cut-off is reached then this step will terminate and the next will begin (i.e. enter charge mode).
Rest	The battery is taken offline for a definable period by explicity including a rest step, and is implicitly included during incremental discharge mode. **Figure 3.11 – PRBS and Rest Time settings**
PRBS	Configuring the PRBS mode (Figure 3.11) involves specifying: 1. PRBS amplitude 2. PRBS generator clock frequency, and acquisition sample rate

	The number of PRBS sequences to run is set by the number of value pairs in the array (e.g. PRBS Clock = 1 kHz, Acquisition Clock = 20 kHz)
End Test	Shuts down the hardware to a safe state
PID Tune	A special mode used for obtaining the PID tuning values used in the charge mode, required when setting up to test a different type cell.

Table 3.2 – Test Options

In addition to these options, the safety limits and general acquisition settings must be set up, as shown in Figure 3.12. The DUT Safety panel allows limits to be set that - when exceeded – execute a shutdown procedure that zeros the load demand, isolates the DUT by allowing the hardware watchdog to timeout, then saves the buffered data, leaving the system in a safe state.

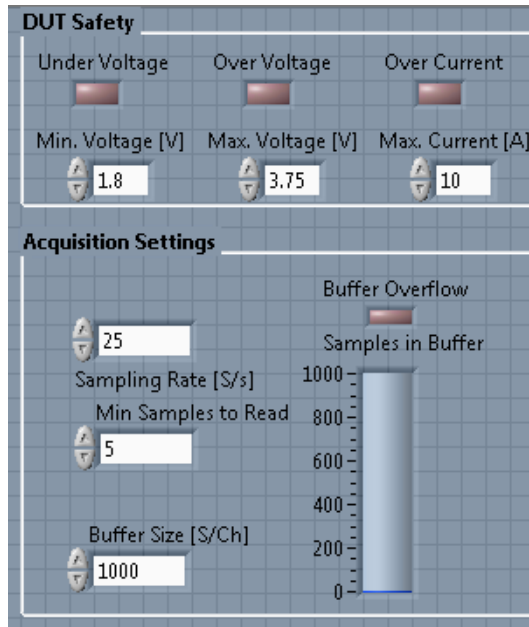
Figure 3.12 – Safety Limits and Acquisition Settings

The acquisition settings (Figure 3.12) apply to all modes except PRBS mode, which is configured separately (see Table 3.2 – Test Options). Visual indicators indicate over-limit conditions.

3.4.2   PRBS Post-Processing

Post processing has been streamlined in the new software, so that impedance results are available immediately at the conclusion of the test. Synchronising the PRBS clock with the data acquisition clock removed the need to use autocorrelation to identify the start and finish points of the PRBS streams, since these points can be directly indexed in the set of acquired samples.

The process for each PRBS clock frequency is to take the FFT of the voltage response and divide point-by-point with the FFT of the current stimulus. This is repeated for each set of time domain PRBS test results, and these impedance spectrums are then sliced to exclude all frequencies above roughly $1/3^{rd}$ of the obtained bandwidth (see Chapter 1; higher frequencies produce impedance data which suffers with poor SNR).

Typically, the PRBS test is set up to repeat at a logarithmic spread of frequencies, e.g. [1, 2, 5, 10, 20, 50, 100, 200, 500, 1k, 2k, 5k, 10k, 20k], producing 14 impedance spectra, each overlapping with its lower frequency neighbours. These band-limited results are then interpolated, averaged and smoothed using a moving average to produce a single continuous impedance spectrum.

3.5 Hardware Performance Characteristics

The equipment has been empirically validated to meet the following conditions (see earlier section for theoretical limits):

	Original Specification	Tested Specification
DUT Voltage Range	1.5 V – 6 V	0 V – 7.4 V
DUT Current Range	± 5 A	+/- 8A
Acquisition Sample Rate	10 kHz desirable, 5kHz acceptable	100 kHz
NI USB-DAQ 6211	Synchronised simultaneous V and I measurement ADCs	Inter-channel Delay = minimum 4µs
	Synchronised sample and PRBS clock	Yes

Table 3.3 – Tested Specifications

3.5.1 Charge Cycling and Pulsed Discharge

Figure 3.13 shows the test log from a charge cycling and pulsed discharge test on a 3 Ah LFP26650E cell. The steps can clearly be identified; a constant-current charge mode is followed by a constant voltage mode, followed by a complete discharge, then a full charge which is followed by a rest period. Here a PRBS impedance test may be performed, followed by a sequence of incremental (pulsed) discharge/rest/PRBS until the low-voltage cut-off is reached. The last section is a charge to approximately 40% SOC, which is the standard SOC level Li-ion cells should be stored at to reduce damage from internal stresses.

The charge curve resets to zero after each step change to minimise cumulative errors and shows the change in absolute charge per step; the observed capacity of this cell when cycled at 1 C is in fact 2.51 Ah. The pulsed discharger was set to remove charge in blocks of 0.6 Ah (20% of nominal capacity), therefore the charge removed per pulse is 20 % of nominal capacity, or $\frac{0.6\ Ah}{2.51\ Ah} = 23.9$ % of actual capacity where present SoH is taken into account.

Full Test Log: 3 Ah, 3.2 V LFP 26650E Cell
Charge/Discharge Current = 3 A (1C)
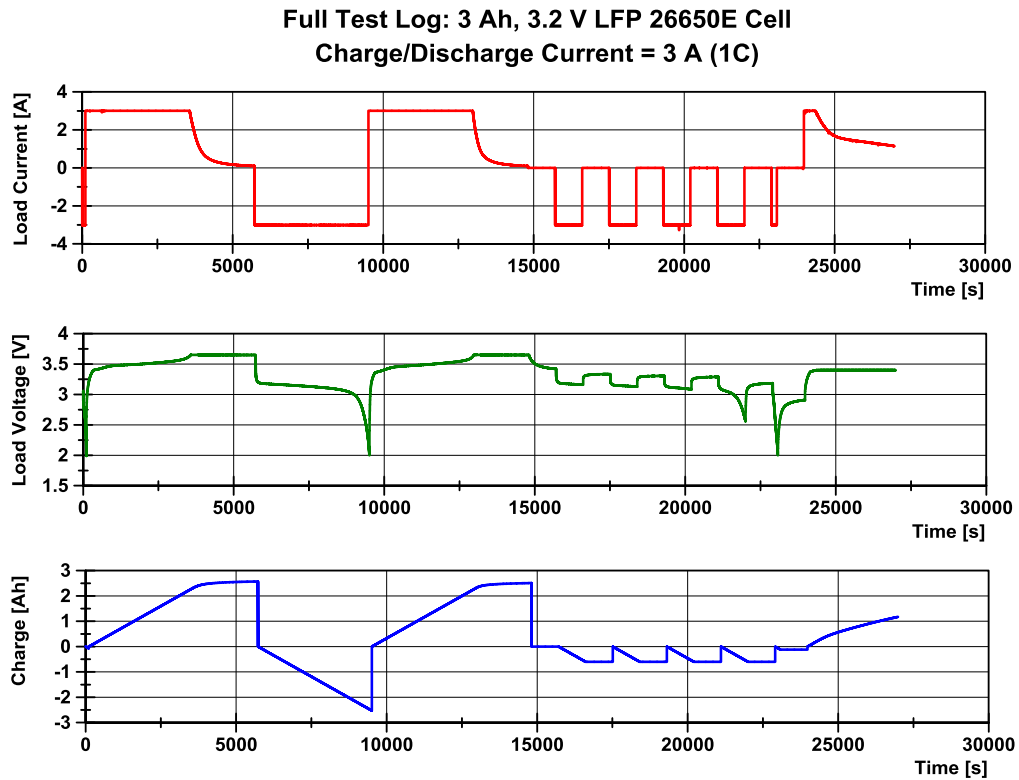
Figure 3.13 – Charge Cycling and Pulsed Discharge, 26650E Cell

Also observable in Figure 3.13 is the smooth transition from constant current charging to constant voltage charging. This is achieved by use of software PID control (described in section 3.4) to monitor the charge voltage and control the charge current to prevent overshoot and maintain a set voltage until the charge current is reduced sufficiently to indicate a full charge.

Calibration of the bulk charge cycling function is checked using an external voltmeter and ammeter, and can be corrected easily using scaling functions within the LabVIEW VI.

3.5.2   PRBS – Time Domain Signals

Figure 3.14 shows the stimulus and response curves for an 8 A peak, 1 Hz PRBS which is 63 bits long. This system test was performed on a 50 Ah Lithium Titanate (LTO) Super Lithium Polymer Battery (SLPB) cell, and this figure, when compared with Figure 2.17, highlights the improved SNR that has been achieved with this design when testing high capacity cells.
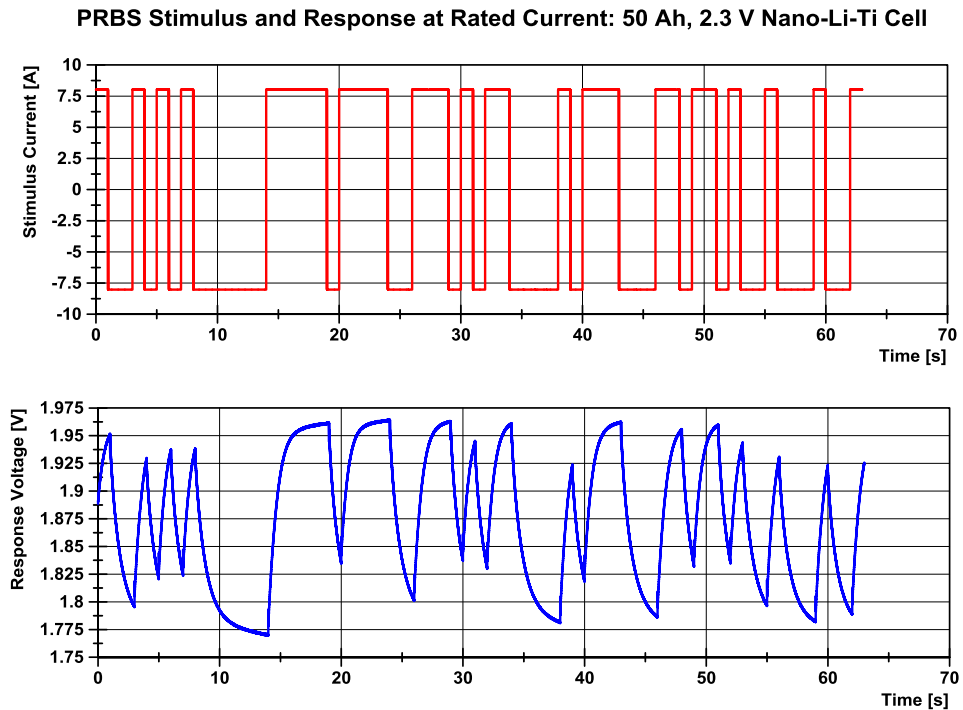
Figure 3.14 – Demonstration of 8 A amplitude PRBS, 1Hz PRBS Clock

The high frequency validation test results shown in Figure 3.15 provide a visual measure of the performance and demonstrate that the system is stable at these higher frequencies. The maximum acquisition rate of the system is 100 kS/s, although as the PRBS clock rate was increased beyond 35 kHz the time domain signal was observed to distort, and frequency analysis showed a sharp increase in noise when plotting the phase of the impedance. The frequency response is discussed in the next section.
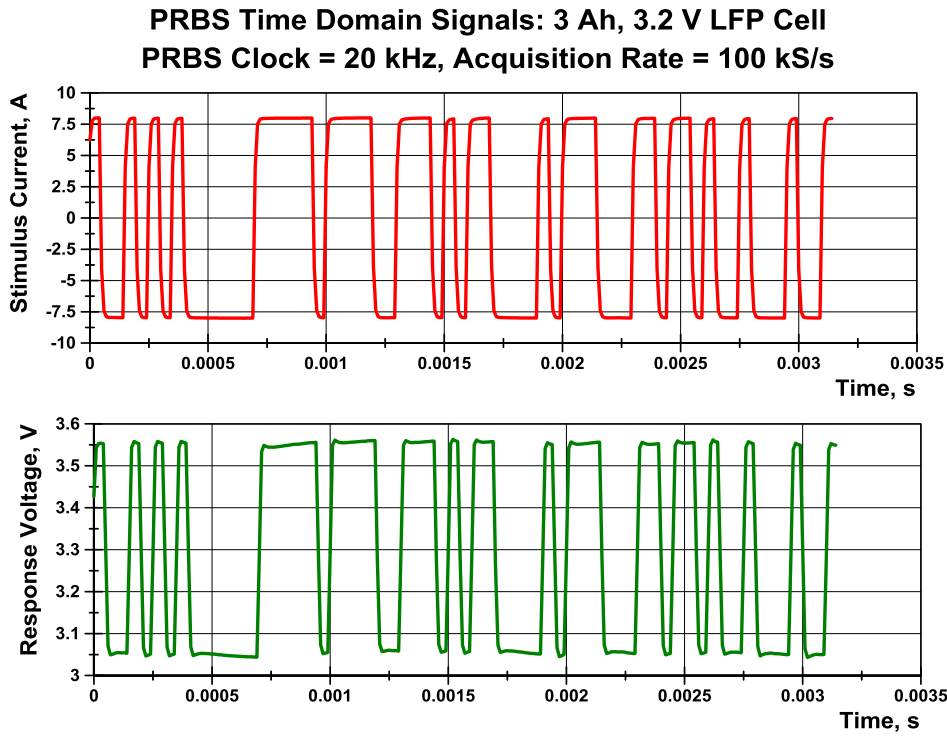
a)
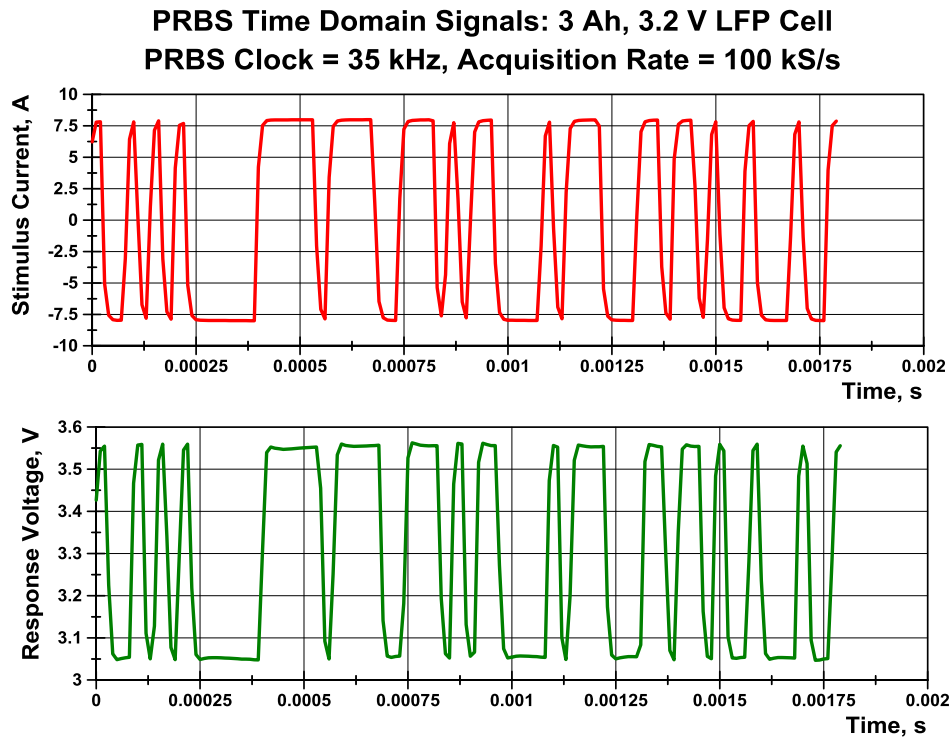
b)

Figure 3.15 – Distortion as PRBS Clock (35 kHz) Approaches the Nyquist Limit (50 kHz)

3.5.3 PRBS – Frequency Response

The frequency response was evaluated by measuring the frequency response of a parallel RC circuit and comparing the response with that of industry standard Solartron 1480 EIS test equipment.
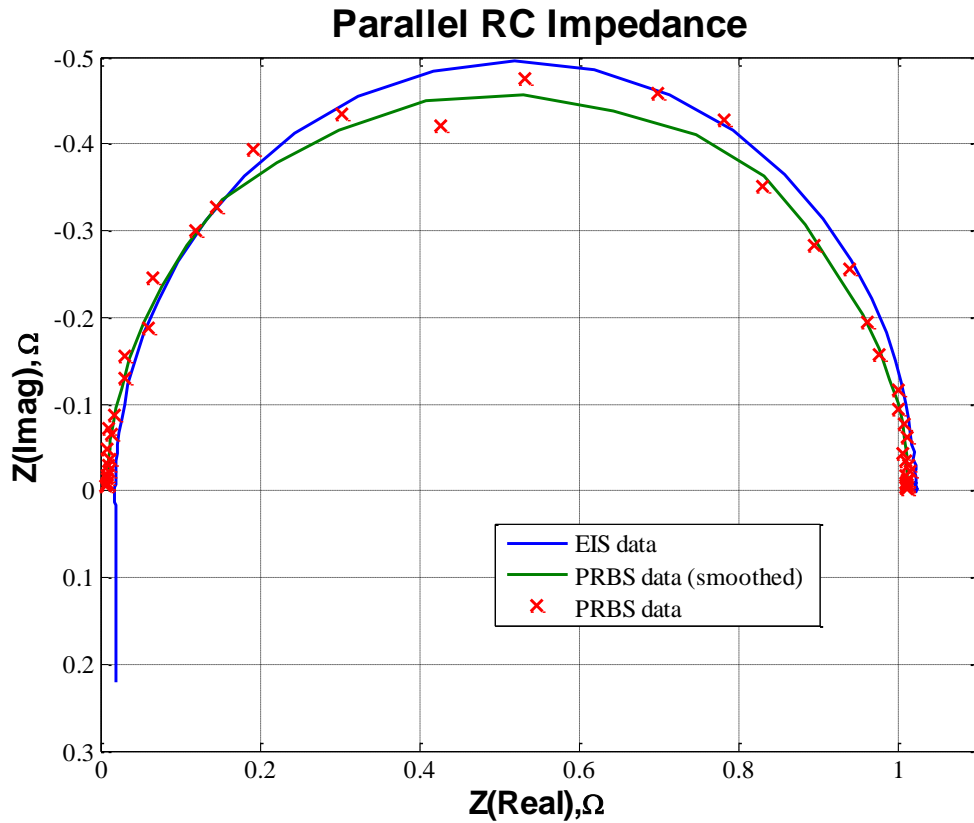
Figure 3.16 – Nyquist Plot of Parallel RC Circuit Validation Test

The results shown in Figure 3.16 show that the PRBS test has captured the characteristic semicircle of a parallel RC circuit. The low frequency points (right hand side) show good correlation with the EIS data (1.07 % error in real component, 0.17 % error in imaginary component), but these errors increase with frequency. Points on the Nyquist plot are not easily correlated to specific frequencies, therefore further analysis of errors is done on the amplitude and phase plots of Figure 3.17.
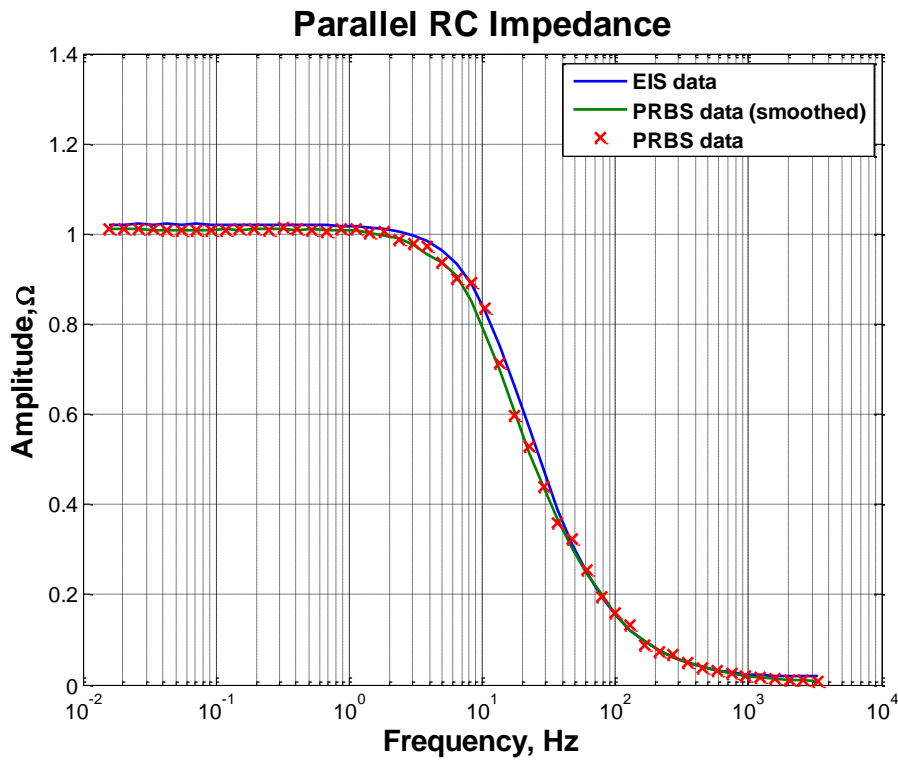
a)
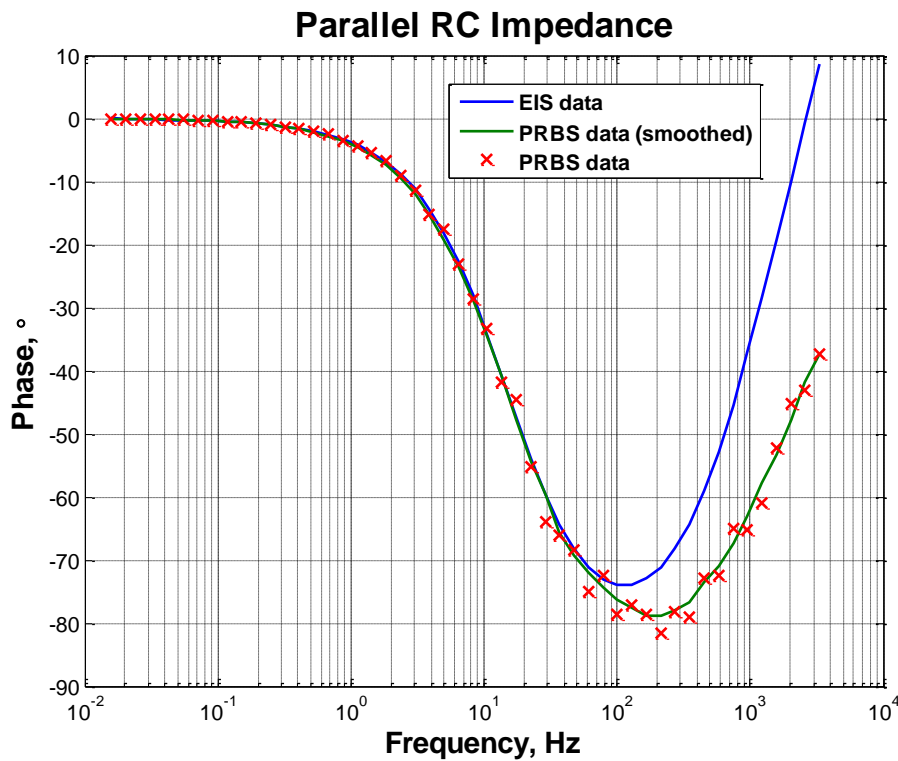
b)

Figure 3.17 – Validation Test: Parallel RC Impedance plots, R = 1 Ω, C = 10 mF

Figure 3.17 shows that for frequencies below 100 Hz, there is good correlation between the standard data and the validation test data. The corner frequency of the circuit is at approximately 15 Hz, and we can observe that this corresponds with a single peak in the amplitude deviation shown in Figure 3.18. During testing, the 200 Hz and 500 Hz PRBS tests were unfortunately not set; it is possible that this error will be reduced if the results of these test frequencies were included, as the data from these sequences (covering 3.1 Hz to 88 Hz, and 7.9 Hz to 222 Hz) would provide the best SNR over the corner frequency. Further work should begin with this step.
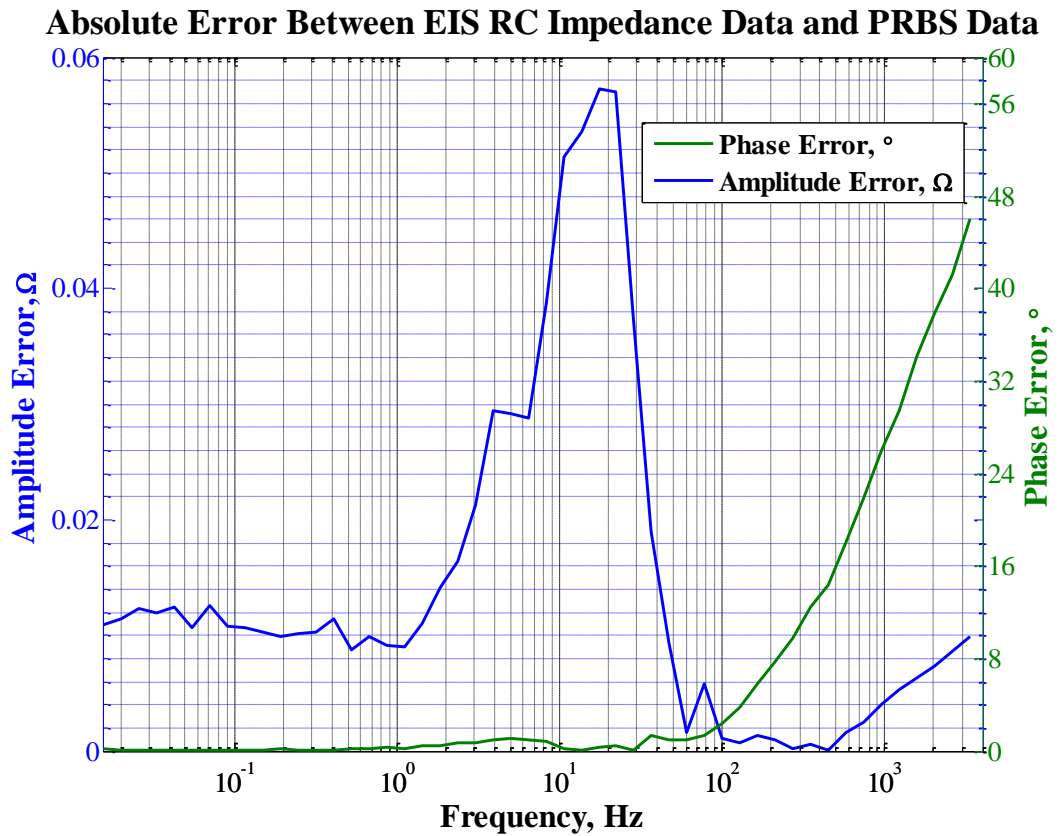
Figure 3.18 – Absolute Error between EIS and PRBS RC Impedance Data

Below 100 Hz the phase error is consistently less than 4 ˚. Above this frequency the error increases dramatically, but also appears to be increasing fairly linearly, at a rate of 24 ˚ per decade between 100 Hz and 1 kHz. This points to a systematic error, and is likely to be due to the inter-channel measurement delay. There was no time to investigate this further, but a quick calculation (delay=phase/frequency) shows that a phase error of 24° at 1 kHz

corresponds to a time delay of 66 µs. The acquisition system used has a minimum inter-channel delay of 4 µs, and a preferred 10 µs settling time between reading each channel. With two differential inputs (four channels) to read, this delay time is most likely the cause of the observed phase error; more tests will be required to prove this.

3.6   Example Results

Figure 3.19 and Figure 3.20 are the results of a one-off impedance test of a 50 Ah, 2.3 V nano Lithium-Titanate cell. The characteristic semicircle due to the parallel RC nature of the cell model is clearly identifiable in the Nyquist plot, and represents the RC element of the charge transfer resistance model. The effect of 7.5 % SoC change is prominently visible at frequencies below 10 Hz.
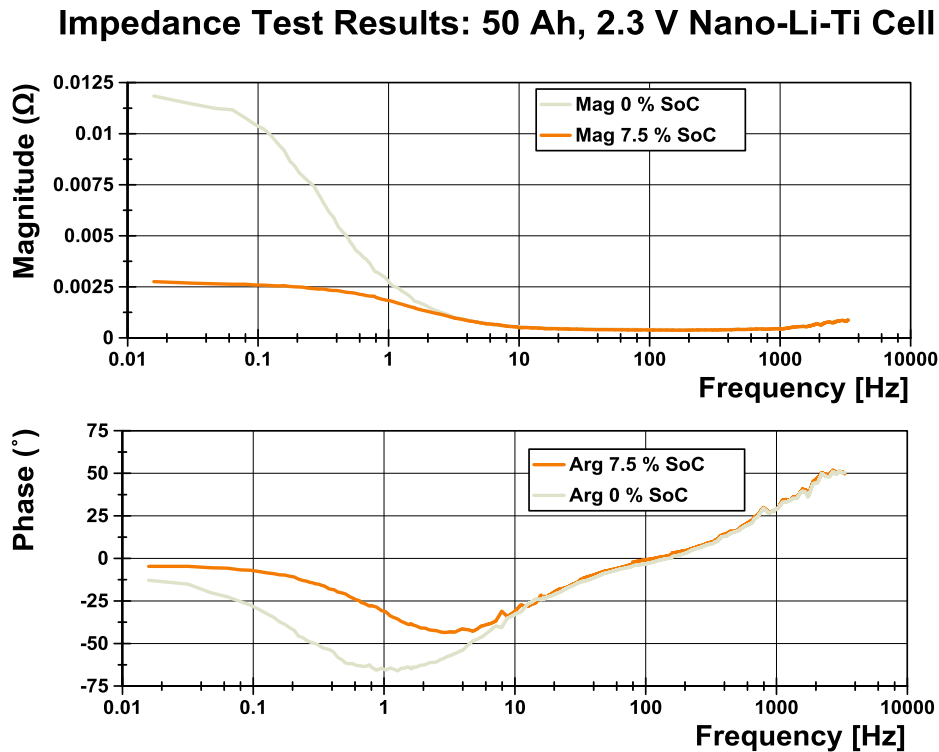
Figure 3.19 – Impedance Data from a Large Capacity Cell

Impedance Test Results: 50 Ah, 2.3 V Nano-Li-Ti Cell
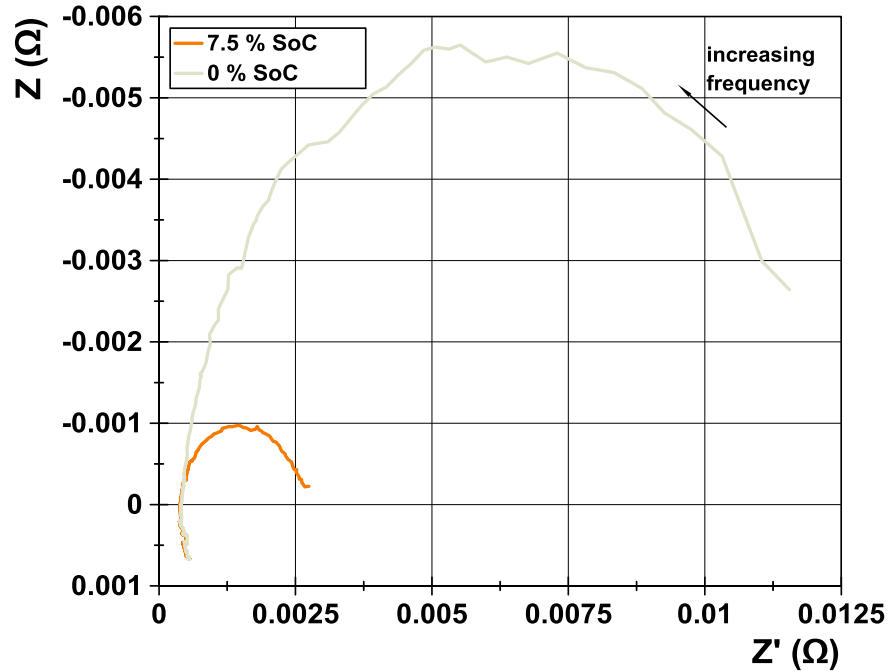
Figure 3.20 – Nyquist Plot of Impedance, 50 Ah SLPB cell

3.7 Conclusion

Early findings have been discussed in section 2.7, *Preliminary Findings and Suggested Changes*. The new impedance test equipment meets the design specification, and performs well at the low frequencies which are of interest in the analysis of battery dynamics. At higher frequencies, while the impedance amplitude data is reliable, the phase data presented here is not. This is believed to be due to the inter-channel measurement delay caused by multiplexing signals to a single ADC. The delay time was significantly reduced in the second design, though it is recommended that simultaneous acquisition is used for further work. Synchronising the measurement sampling and PRBS generation has enabled a more a robust procedure for capturing good quality results, as has the ability to test higher capacity cells at larger stimulus current levels.

Chapter 4: Conclusions and Suggestions for Further Work

4.1 Conclusions

The first chapter was a brief overview of popular EV battery chemistries, with a functional description of Battery Management Systems and battery state estimation techniques. Electrochemical Impedance Spectroscopy was introduced as a system identification tool and we showed how Pseudo-Random Binary Sequences can be used as a system stimulus approximating white noise, giving the benefits of wide-bandwidth system identification with the convenience of a short test duration.

Chapter 2 described the development of equipment to cycle charge and measure the impedance of a range of Li-ion cells. The results of tests on two types of cell, LFP 26650E 3 Ah cells and LTO polymer 100 Ah pouch cells, are presented along with an analysis of the weaknesses found in the early system which prompted a redesign and new methods. This can be found in section 2.7, but the main findings from the first system are summarised here:

1) Charge Cycling
   a) When cycling higher voltage battery packs high frequency oscillations could not be prevented. For this reason we were not able to map the maximum power characteristics of the cell, although low voltage (3.7 V) single cells were successfully cycled at rates of 20 A (C/5) using a single output channel.
   b) The above stability problems meant that cells sometimes had to be charged using a bench power supply directly, and some charging data was lost as a result. The ability to compare charging capacity against discharging capacity would be useful to provide an analysis of cell dynamic characteristics and forming bi-directional models.
   c) An oversight in the initial setup was not to continuously log the cell terminal voltage as it settled during the voltage relaxation step of a pulsed discharge. Without this data we cannot attempt to compensate for any insufficiency in settling time by means of extrapolation.
2) PRBS Impedance Testing
   a) The PRBS generation clock and data acquisition clock must be synchronised; the inter-channel delay of the acquisition system was discovered to be up to 12 % of the

PRBS clock period and 60 % of the acquisition period. This margin of error is unacceptable for a PRBS analysis, where exact-length sequences are required for a clean FFT.

b) Software timing is not a reliable method for generating a precise PRBS stream and should be avoided.

c) Choosing the amplitude of a PRBS stimulus current requires making a trade-off between obtaining a voltage response with good signal-to-noise ratio while maintaining the cell in a steady state. Having bipolar stimulus capabilities allows the stimulus current level to be increased while maintaining a steady state in the cell SoC compared to a unipolar PRBS test.

d) Sensitive measurement instruments are not commonly available in very high cell-count battery packs, where 5 mV resolution is considered to be good [52]. This must be taken into consideration when designing an embedded impedance tester for very low impedance cells such as high capacity LTO cells, for example.

These shortcomings are addressed in the second design iteration presented in Chapter 3. The remaining problem with the system in Chapter 3 is believed to be again caused by the inter-channel measurement delay which causes the phase error to become significant at higher frequencies. This delay time (caused by multiplexing analogue inputs to a single ADC) was reduced from 160 µs in the first design to perhaps 66 µs in the second, and is suspected to account for the frequency dependent phase error seen in the second system (Figure 3.18 – Absolute Error between EIS and PRBS RC Impedance Data).

4.2 **Suggestions for Further Work**

Further work should begin with an investigation of the effect that the inter-channel measurement delay has on the existing system. Provided that the results are reproducible – i.e. that the delay is constant – then a phase compensation scheme should be easy to implement. If the delay is not constant or predictable, then the options are to design a sample-and-hold acquisition system or else to obtain an acquisition system that contains at least four individual ADCs and hence requires no input multiplexing.

The second suggestion for further work pertains to cell testing methods. We have seen that for an impedance measurement to be useful for system identification then the SoC of the cell

must not change significantly while making the measurement. If we quantify this and say that the SoC must not change by more than say 1 % during a test, then using the PRBS test time (say 100 seconds) we can define a discharge rate at which an injected PRBS ripple would give meaningful impedance results. For example, using the figures above we could say that a constant discharge at a rate of $C \times 0.01 \times \frac{3600}{100} = 0.36C$ could be combined with a bipolar (i.e. does not contribute to a mean change in charge) PRBS ripple to yield approximately one hundred wide-band impedance readings over a full discharge. Clearly these numbers would have to be refined empirically to account for the fact that the cell does not discharge linearly, to keep the maximum SoC change during a PRBS within the set tolerance. The advantages of such an approach include the ability to observe key changes in impedance during a charge cycle at a relatively high resolution between states; furthermore with charging impedances distinct from the impedances obtained during discharging then a truly bi-directional model can be developed. The existing hardware is capable of performing this experiment with only a slight software modification. The idea came from a paper [60] in which the authors recorded the discharge characteristic of a cell discharged with a continuous GSM power pulse, in order to assess the impact of the application on cell capacity.

One reason that PRBS is used as a stimulus signal is that it produces a flat wide-band power spectrum. This is good for identifying unknown systems, but may be a disadvantage on a known system. For example, if the largest changes in impedance occur in limited bands of the spectrum – e.g. from 1 mHz to 5 Hz, and from 2 kHz to 8 kHz – then it may be advantageous to switch to Binary Multi-frequency Signal stimulation. These signals concentrate the power spectrum to specific frequency bands, giving better signal-to-noise ratio in the areas of interest [65]. It would of course be easy to implement a Binary Multi-frequency test with the present hardware.

We have detailed the design process, the shortcomings of the initial design and the steps taken to overcome them. Within the third chapter are adequate details for the reader to reproduce the system described here, and three ideas for further work have been given.

References

[1] J. Larminie and J. Lowry, *Electric vehicle technology explained*. J. Wiley, 2003.

[2] S. Vazquez, S. M. Lukic, E. Galvan, L. G. Franquelo, and J. M. Carrasco, "Energy Storage Systems for Transport and Grid Applications," *Industrial Electronics, IEEE Transactions on*, vol. 57, no. 12, pp. 3881–3895, 2010.

[3] J. McDowall, "Integrating energy storage with wind power in weak electricity grids," *Journal of Power Sources*, vol. 162, no. 2, pp. 959–964, 2006.

[4] S. Bharadwaj, "Clean Energy Storage for Grid Load Leveling -The Metlakatla Battery Energy Storage System - Twelve Years Of Success," in *Irena Conference, Port Vila*, 2012.

[5] M. Farber_De_Anda, J. D. Boyes, and W. Torres, "Lessons Learned from the Puerto Rico Battery Energy Storage System," Sandia National Laboratories, 1999.

[6] "DIRECTIVE 2002/95/EC OF THE EUROPEAN PARLIAMENT AND OF THE COUNCIL of 27 January 2003." 2003.

[7] "Battery Recycling." Battery Council International, 2009.

[8] N. Garimella and N.-K. C. Nair, "Assessment of battery energy storage systems for small-scale renewable energy integration," in *TENCON 2009 - 2009 IEEE Region 10 Conference*, 2009, pp. 1–6.

[9] O. Edberg and C. Naish, "Energy Storage and Management Study," AEA Group for Scottish Government, 2010.

[10] C. Naish, I. McCubbin, O. Edberg, and M. Harfoot, "Outlook of Energy Storage Technologies," European Parliament's committee on Industry, Research and Energy (ITRE), January 2004, 2008.

[11] B. Dunn, H. Kamath, and J.-M. Tarascon, "Electrical Energy Storage for the Grid: A Battery of Choices," *Science*, vol. 334, no. 6058, pp. 928–935, 2011.

[12] M. Duduta, B. Ho, V. C. Wood, P. Limthongkul, V. E. Brunini, W. C. Carter, and Y.-M. Chiang, "Semi-Solid Lithium Rechargeable Flow Battery," *Advanced Energy Materials*, vol. 1, no. 4, pp. 511–516, 2011.

[13] A. Kraytsberg and Y. Ein-Eli, "Review on Li-air batteries: Opportunities, limitations and perspective," *Journal of Power Sources*, vol. 196, no. 3, pp. 886–893, 2011.

[14] B. Scrosati and J. Garche, "Lithium batteries: Status, prospects and future," *Journal of Power Sources*, vol. 195, no. 9, pp. 2419–2430, 2010.

[15] K. C. Divya and J. Ostergaard, "Battery energy storage technology for power systems - An overview," *Electric Power Systems Research*, vol. 79, no. 4, pp. 511–520, 2009.

[16] J. W. Fergus, "Recent developments in cathode materials for lithium ion batteries," *Journal of Power Sources*, vol. 195, no. 4, pp. 939–954, 2010.

[17] M. Armand and J.-M. J.-M. Tarascon, "Building better batteries," *Nature*, vol. 451, no. 7179, pp. 652–657, 2008.

References

[18] A. M. Stephan and K. S. Nahm, "Review on composite polymer electrolytes for lithium batteries," *Polymer*, vol. 47, no. 16, pp. 5952–5964, 2006.

[19] L. Florence, "Safety Issues for Lithium-Ion Batteries," Underwriters Laboratories Inc, 2010.

[20] J. Friedman-Rudovsky, "For Lithium Car Batteries, Bolivia Is in the Driver's Seat," *Time Magazine*, Jan. 2009.

[21] H. Aral and A. Vecchio-Sadus, "Toxicity of lithium to humans and the environment: A literature review," *Ecotoxicology and Environmental Safety*, vol. 70, no. 3, pp. 349–356, 2008.

[22] E. Musk, "Tesla Adds Titanium Underbody Shield and Aluminium Deflector Plates to Model S," Tesla Motors, 2014.

[23] "Interim Factual Report, NTSB Case Number DCA13IA037," National Transportation Safety Board, 2013.

[24] NTSB, "NTSB Press Release: NTSB Issues Recommendations on Certification of Lithium-Ion Batteries and Emerging Technologies." May-2014.

[25] "Q&A Concerning the NAS Battery Fire," NGK Insulators Ltd, 2012.

[26] V. Pop, H. J. Bergveld, D. Danilov, P. P. L. Regtien, and P. H. L. Notten, *Battery Management Systems - Accurate State-of-Charge Indication for Battery Powered Applications*, vol. 9. Springer, 2008.

[27] R. Lu, T. Wang, F. Feng, and C. Zhu, "SOC Estimation Based on the Model of Ni-MH Battery Dynamic Hysteresis Characteristic," *World Electric Vehicle Journal*, vol. 4, pp. 259–265, 2010.

[28] M. a. Roscher and D. U. Sauer, "Dynamic electric behavior and open-circuit-voltage modeling of LiFePO4-based lithium ion secondary batteries," *Journal of Power Sources*, vol. 196, no. 1, pp. 331–336, 2011.

[29] C. Blanco, L. Sanchez, M. Gonzalez, J. C. Anton, V. Garcia, and J. C. Viera, "An Equivalent Circuit Model with Variable Effective Capacity for LiFePO4 Batteries," *Vehicular Technology, IEEE Transactions on*, vol. PP, pp. 1–1, 2014.

[30] S. Abu-Sharkh and D. Doerffel, "Rapid test and non-linear model characterisation of solid-state lithium-ion batteries," *Journal of Power Sources*, vol. 130, no. 1–2, pp. 266–274, 2004.

[31] D. Andre, C. Appel, T. Soczka-Guth, and D. U. Sauer, "Advanced mathematical methods of SOC and SOH estimation for lithium-ion batteries," *Journal of Power Sources*, vol. 224, pp. 20–27, 2013.

[32] P. Baudry, M. Neri, M. Gueguen, and G. Lonchampt, "Electro-thermal modelling of polymer lithium batteries for starting period and pulse power," *Journal of Power Sources*, vol. 54, no. 2, pp. 393–396, 1995.

[33] H. Blanke, O. Bohlen, S. Buller, R. W. De Doncker, B. Fricke, A. Hammouche, D. Linzen, M. Thele, and D. U. Sauer, "Impedance measurements on lead–acid batteries

for state-of-charge, state-of-health and cranking capability prognosis in electric and hybrid electric vehicles," *Journal of Power Sources*, vol. 144, no. 2, pp. 418–425, 2005.

[34] S. Buller, M. Thele, and R. W. A. A. D. Doncker, "Impedance-Based Simulation Models of Supercapacitors and Li-Ion Batteries for Power Electronic Applications," vol. 41, no. 3, pp. 742–747, 2005.

[35] L. Chenglin, L. Huiju, and W. Lifang, "A dynamic equivalent circuit model of LiFePO4 cathode material for lithium ion batteries on hybrid electric vehicles," *2009 IEEE Vehicle Power and Propulsion Conference*, pp. 1662–1665, Sep. 2009.

[36] Y.-H. Chiang, W.-Y. Sean, and J.-C. Ke, "Online estimation of internal resistance and open-circuit voltage of lithium-ion batteries in electric vehicles," *Journal of Power Sources*, vol. 196, no. 8, pp. 3921–3932, 2011.

[37] J. Gomez, R. Nelson, E. E. Kalu, M. H. Weatherspoon, and J. P. Zheng, "Equivalent circuit model parameters of a high-power Li-ion battery: Thermal and state of charge effects," *Journal of Power Sources*, vol. 196, no. 10, pp. 4826–4831, 2011.

[38] H. He, R. Xiong, and J. Fan, "Evaluation of Lithium-Ion Battery Equivalent Circuit Models for State of Charge Estimation by an Experimental Approach," *Energies*, vol. 4, no. 4, pp. 582–598, 2011.

[39] X. Hu, S. Li, and H. Peng, "A comparative study of equivalent circuit models for Li-ion batteries," *Journal of Power Sources*, vol. 198, pp. 359–367, 2012.

[40] X. Hu, S. Li, H. Peng, and F. Sun, "Robustness analysis of State-of-Charge estimation methods for two types of Li-ion batteries," *Journal of Power Sources*, vol. 217, pp. 209–219, 2012.

[41] Y. Hu and S. Yurkovich, "Battery cell state-of-charge estimation using linear parameter varying system techniques," *Journal of Power Sources*, vol. 198, pp. 338–350, 2012.

[42] V. H. Johnson, "Battery performance models in ADVISOR," *Journal of Power Sources*, vol. 110, no. 2, pp. 321–329, 2002.

[43] V. Johnson, A. Pesaran, and T. Sack, "Temperature-Dependent Battery Models for High-Power Lithium-Ion Batteries," in *17th Electric Vehicle Symposium*, 2000.

[44] J. Li, J. Klee Barillas, C. Guenther, and M. a. Danzer, "A comparative study of state of charge estimation algorithms for LiFePO4 batteries used in electric vehicles," *Journal of Power Sources*, vol. 230, pp. 244–250, 2013.

[45] R. B. Polder, *Electrodynamics of the AgI/solution Interface*. ISN=211440-03, 1984.

[46] A. Rahmoun and H. Biechl, "Modelling of Li-ion batteries using equivalent circuit diagrams," vol. 2, no. 7, pp. 152–156, 2012.

[47] U.S.D.O.E., *PNGV Battery Test Manual*, no. February. 2001.

[48] N. Watrin, B. Blunier, and A. Miraoui, "Review of adaptive systems for lithium batteries State-of-Charge and State-of-Health estimation," *2012 IEEE Transportation Electrification Conference and Expo (ITEC)*, no. 3, pp. 1–6, 2012.

[49] J. D. Kozlowski, "Electrochemical cell prognostics using online impedance measurements and model-based data fusion techniques," in *Aerospace Conference, 2003. Proceedings. 2003 IEEE*, 2003, vol. 7, pp. 3257–3270.

[50] A. J. Salkind, C. Fennie, P. Singh, T. Atwater, and D. E. Reisner, "Determination of state-of-charge and state-of-health of batteries by fuzzy logic methodology," *Journal of Power Sources*, vol. 80, no. 1–2, pp. 293–300, 1999.

[51] P. Singh and C. F. Jr, "Fuzzy logic-enhanced electrochemical impedance spectroscopy (FLEEIS) to determine battery state-of-charge," *Battery Conference on …*, 2000.

[52] L. Lu, X. Han, J. Li, J. Hua, and M. Ouyang, "A review on the key issues for lithium-ion battery management in electric vehicles," *Journal of Power Sources*, vol. 226, pp. 272–288, 2013.

[53] O. Gerard, J.-N. Patillon, and F. d Alche-Buc, "Neural network adaptive modeling of battery discharge behavior," in *Artificial Neural Networks - ICANN'97*, vol. 1327, W. Gerstner, A. Germond, M. Hasler, and J.-D. Nicoud, Eds. Springer Berlin Heidelberg, 1997, pp. 1095–1100.

[54] B. S. Bhangu, P. Bentley, D. A. Stone, and C. M. Bingham, "Observer techniques for estimating the state-of-charge and state-of-health of VRLABs for hybrid electric vehicles," in *Vehicle Power and Propulsion, 2005 IEEE Conference*, 2005, p. 10 pp.

[55] B. S. Bhangu, P. Bentley, D. A. Stone, and C. M. Bingham, "State-of-charge and state-of-health prediction of lead-acid batteries for hybrid electric vehicles using non-linear observers," in *Power Electronics and Applications, 2005 European Conference on*, 2005, p. 10 pp. –P.10.

[56] B. S. Bhangu, P. Bentley, D. A. Stone, and C. M. Bingham, "Nonlinear observers for predicting state-of-charge and state-of-health of lead-acid batteries for hybrid-electric vehicles," *Vehicular Technology, IEEE Transactions on*, vol. 54, no. 3, pp. 783–794, 2005.

[57] C. Gould, J. Wang, D. Stone, and M. Foster, "EV/HEV Li-ion battery modelling and State-of-Function determination," *International Symposium on Power Electronics Power Electronics, Electrical Drives, Automation and Motion*, pp. 353–358, 2012.

[58] C. R. Gould, C. M. Bingham, D. A. Stone, and P. Bentley, "New Battery Model and State-of-Health Determination Through Subspace Parameter Estimation and State-Observer Techniques," *Vehicular Technology, IEEE Transactions on*, vol. 58, no. 8, pp. 3905–3916, 2009.

[59] J. L. Lee, A. Chemistruck, and G. L. Plett, "One-dimensional physics-based reduced-order model of lithium-ion dynamics," *Journal of Power Sources*, vol. 220, pp. 430–448, 2012.

[60] A. Jossen, "Fundamentals of battery dynamics," *Journal of Power Sources*, vol. 154, no. 2, pp. 530–538, 2006.

[61] B. Sanchez, G. Vandersteen, R. Bragos, and J. Schoukens, "Basics of broadband impedance spectroscopy measurements using periodic excitations," *Measurement Science and Technology*, vol. 23, no. 10, p. 105501, 2012.

[62] E. Barsoukov and J. R. Macdonald, Eds., *Impedance Spectroscopy - Theory, Experiment and Applications*. Wiley, 2005.

[63] W. D. T. Davies, "Using the binary maximum length sequence for the identification of system dynamics," *Electrical Engineers, Proceedings of the Institution of*, vol. 114, no. 10, pp. 1582–1584, 1967.

[64] J. Schoukens, R. M. Pintelon, and Y. J. Rolain, "Broadband versus stepped sine FRF measurements," *IEEE Transactions on Instrumentation and Measurement*, vol. 49, no. 2, pp. 275–278, 2000.

[65] K. Godfrey, "Introduction to binary signals used in system identification," in *Control 1991. Control'91., International Conference on*, 1991, pp. 161–166.

[66] A. J. Fairweather, M. P. Foster, and D. A. Stone, "Battery parameter identification with Pseudo Random Binary Sequence excitation (PRBS)," *Journal of Power Sources*, vol. 196, no. 22, pp. 9398–9406, 2011.

[67] A. J. Fairweather, M. P. Foster, and D. A. Stone, "VRLA battery parameter identification using pseudo random binary sequences (PRBS)," in *Power Electronics, Machines and Drives (PEMD 2010), 5th IET International Conference on*, 2010, pp. 1–6.
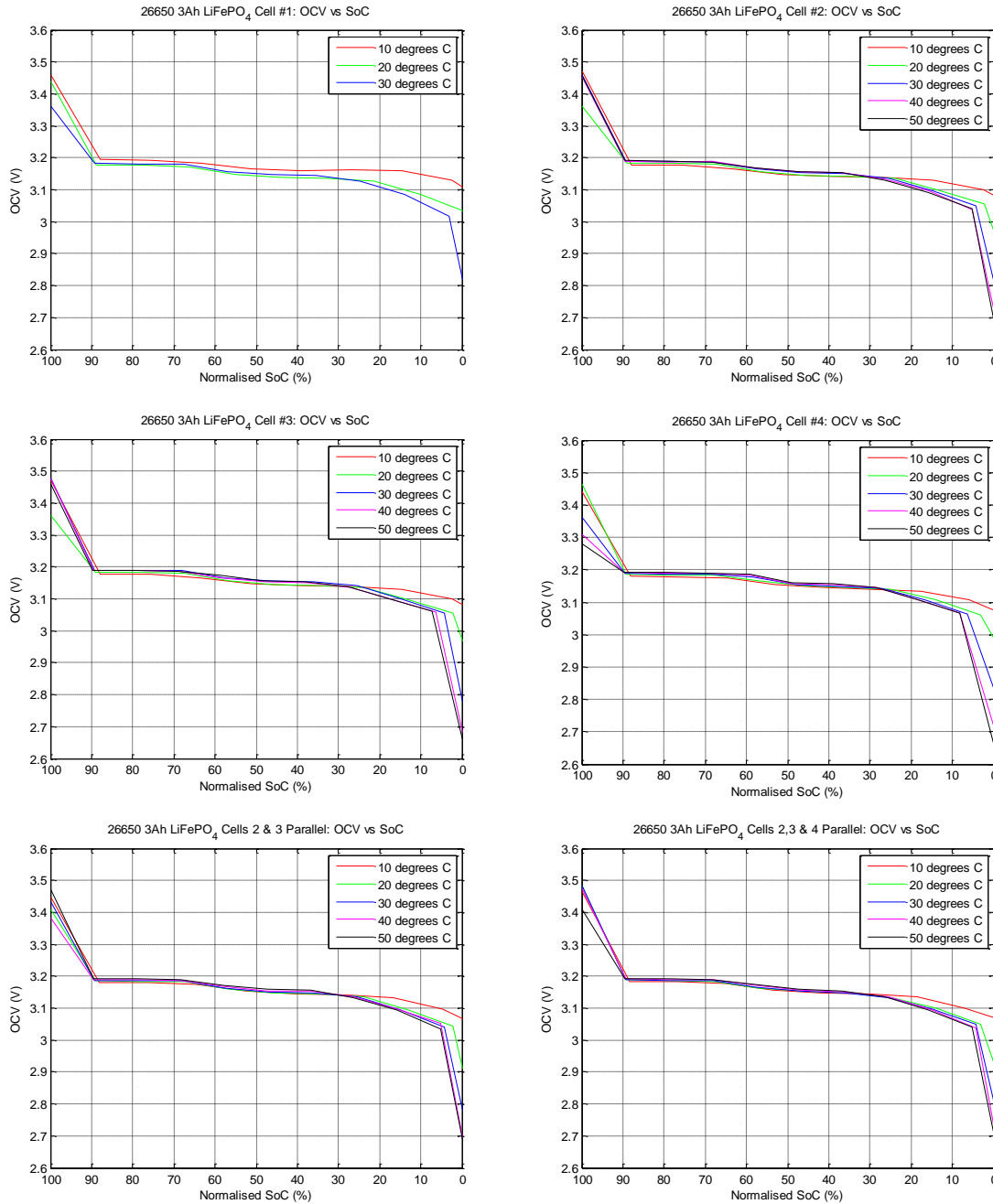
Appendix 1.

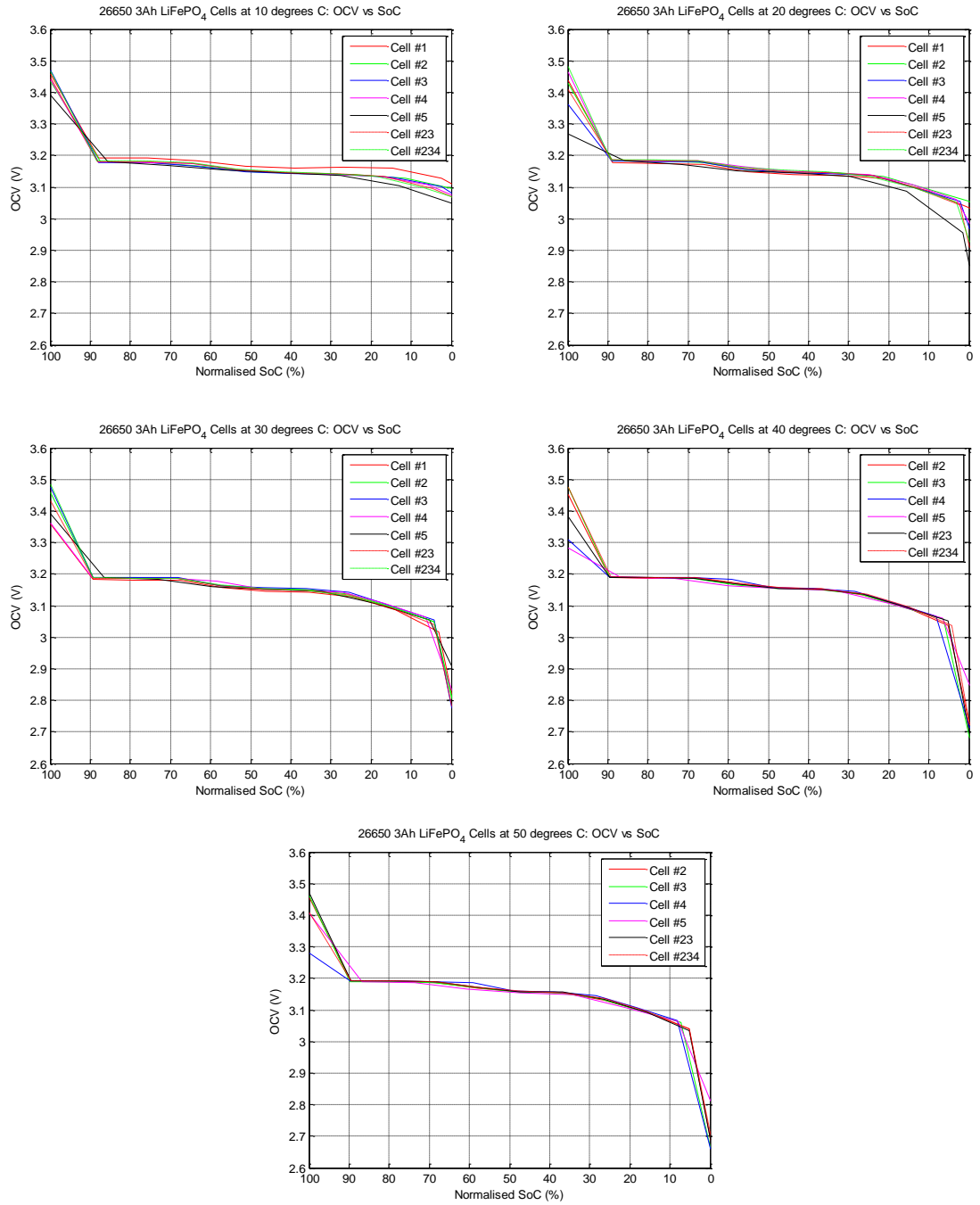**Figure A. 1 – 26650E Cell OCV vs. SoC for each Cell Configuration**

Figure A. 2 – 26650E Cells: OCV vs. SoC at Fixed Temperatures, Comparing Cells
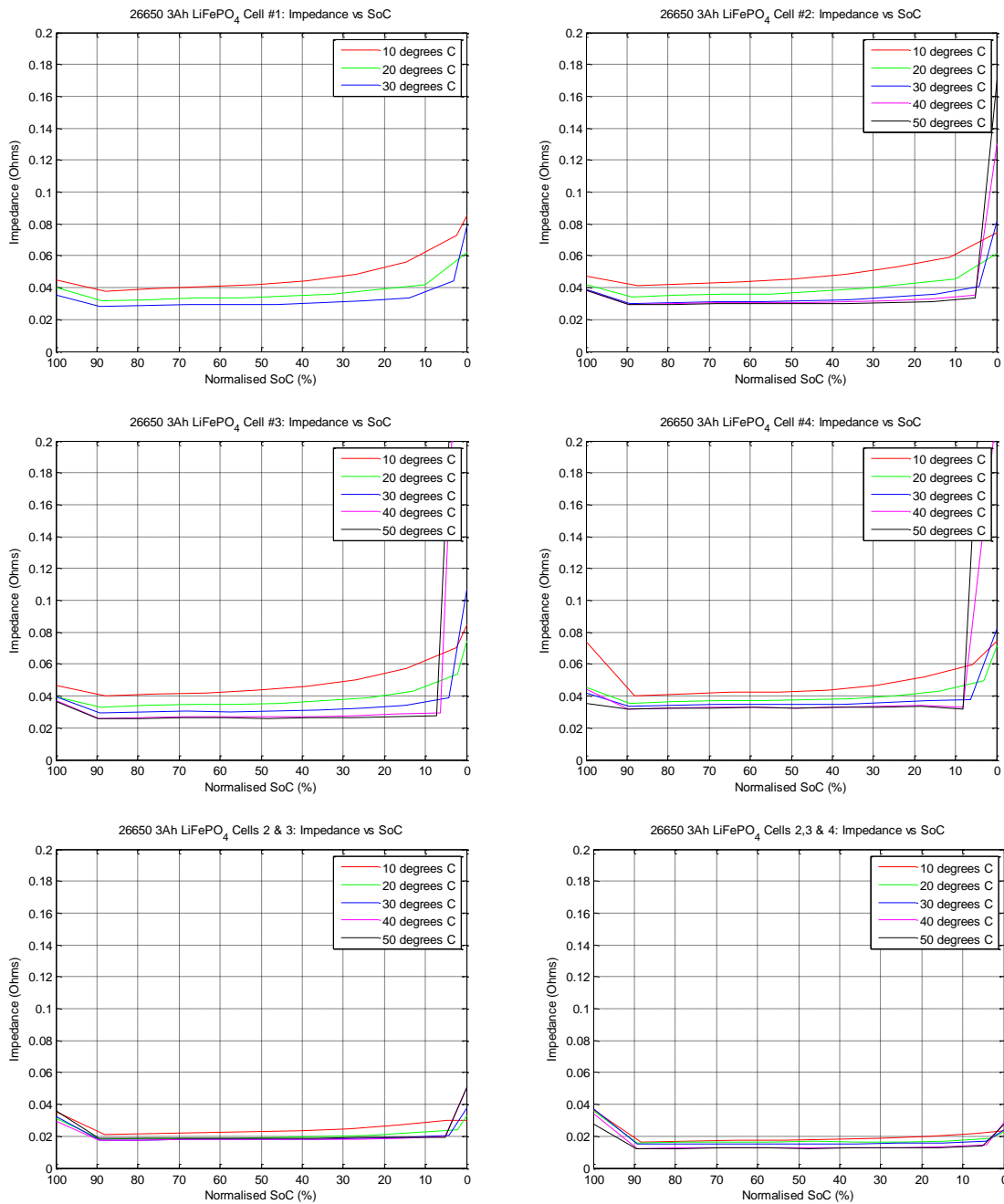
Figure A. 3 – 26650E Cells: Average Impedance at 0-0.5 Hz vs. SoC for each Cell Configuration
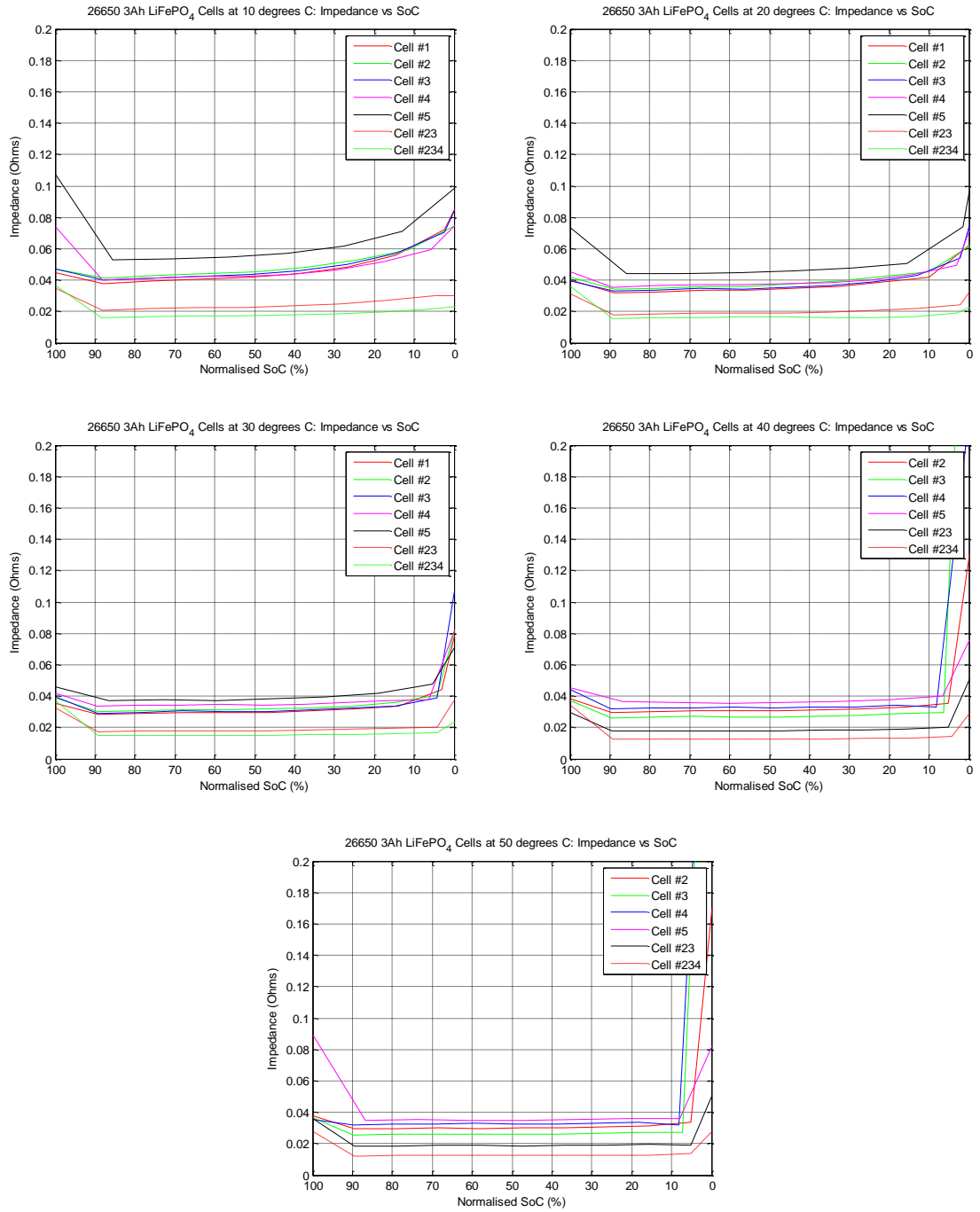
Figure A. 4 - 26650E Cell Comparison at Fixed Temperature: Average Impedance at 0-0.5 Hz vs. SoC